A Narrow-linewidth Laser System for the $^{1}S_{0}$-$^{3}P_{2}$ Intercombination Transition in Strontium

Yilong Yang

München 2021

Ein schmalbandiges Lasersystem für den $^1S_0$-$^3P_2$ Interkombinationsübergang in Strontium

Masterarbeit an der Fakultät für Physik
Ludwig-Maximilians-Universität München

vorgelegt von

Yilong Yang

aus Beijing

München, den 10. Oktober 2021

Abstract

In this thesis, we report on the generation, stabilization, and delivery of narrow-linewidth laser light for the $^1S_0$-$^3P_2$ intercombination transition in strontium. For this purpose, a diode laser is frequency-stabilized to an ultrastable reference cavity and low-noise delivery is ensured by a home-built fiber noise cancellation system. The laser system will serve as a tool for preparing a 2D layer of strontium atoms trapped in an optical lattice for quantum simulation purposes in the future. This work was done in the strontium laboratory in Prof. Dr. Immanuel Bloch's group at MPQ under the supervision of Dr. Sebastian Blatt.

Contents

List of Tables

List of Figures

Chapter 1

Introduction

Ultracold neutral atoms in optical lattices serve as a promising platform for quantum simulation [1] due to their high degrees of controllability and scalability [2]. Via the implementation of the revolutionary technique of quantum gas microscope, these platforms can be further upgraded to allow for single-site resolved imaging and addressing of individual atoms through a microscope objective [3–5]. In our experiment, we aim to construct a strontium quantum gas microscope with state-dependent lattices for quantum simulations [6]. As an alkaline-earth metal atom, strontium has a rich internal energy level structure due to its two valence electrons, and serves as great candidate for studies of quantum many-body physics. The energy level diagram showing the most important states and transitions is shown in Fig. 1.1.

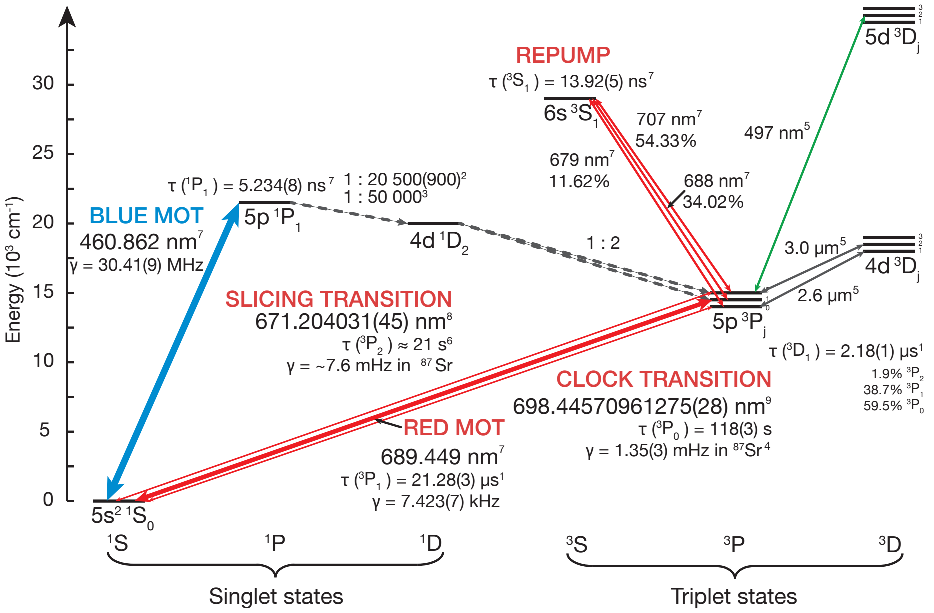

Figure 1.1 An energy level diagram showing the most important states and transitions including lifetimes and important branching ratios in strontium. Data taken from Refs. ^{1}[7] ^{2}[8] ^{3}[9] ^{4}[10] ^{5}[11] ^{6}[12] ^{7}[6] ^{8}[13] ^{9}[14]. Figure adapted from [15].

The general idea behind simulating the dynamics of a quantum state using our system is the following. We start by lowering the lattice depth to allow for atoms to tunnel between different sites, corresponding to the evolving of a prepared quantum state. After a certain time, we increase the lattice depth again to localize the atoms. The distribution of atoms in this case is closely related to the final state that we are interested in. We use a quantum gas microscope to probe the occupation of each lattice site by sending a fluorescence beam and collecting the scattered photons with a high resolution objective. Since in reality the finite depth of field of the microscope could simultaneously cover multiple layers of atoms in a 3D optical lattice, it is essential for us to be able to isolate a single layer of atoms before the imaging process to decrease possible background noise from adjacent layers. To this end, we apply a scheme that was first demonstrated in an ytterbium quantum gas microscope shown in Ref. [16] for the preparation of a single layer of strontium atoms.

In this scheme, we apply a strong magnetic field with a large gradient along the vertical direction of the 3D optical lattice. The magnetic field gradient provides an inhomogeneous frequency shift in the $^1S_0$-$^3P_2$ transition in space due to Zeeman effect so that different atomic layers correspond to different excitation frequencies. At this point, there are two possible strategies to proceed for the preparation of the 2D layer. The first approach is to excite all the layers except the desired one, and let strong inelastic two-body collisions depopulate the $^3\mathrm{P}_2$ atoms in other layers. Such a strategy was used by the ytterbium experiment. However, according to Ref. [17], they have to go through multiple rounds of excitation and collision to have the atoms in the unwanted layers fully depopulate. An alternative method is to only excite the desired layer of atoms to the $^3\mathrm{P}_2$ state, and then immediately apply the blue $^1\mathrm{S}_0$-$^1\mathrm{P}_1$ laser light to scatter the ground state atoms in all the other layers off the trap. Such a method is more time-efficient, but requires that the “blasting-off ” of the ground state atoms must finish before a significant amount of $^3\mathrm{P}_2$ atoms in the desired layer fall out of the trap due to the aforementioned inelastic collisions. For both approaches, we require a high-quality laser beam at the $^1\mathrm{S}_0$-$^3\mathrm{P}_2$ transition frequency with a linewidth narrower than the energy splitting between adjacent layers of atoms, which will be calculated in the following.

In our case, the $^1S_0$-$^3P_2$ transition for the fermionic atoms $^{87}\mathrm{Sr}$ is selected to take place between the $^1\mathrm{S}_0$(F = 9/2) - $^3\mathrm{P}_2$(F = 11/2) hyperfine states. Once the magnetic field is applied, we first spin polarize the atoms in the $^1\mathrm{S}_0$ ground state to the Zeeman level $m_F = 9/2$, and then apply circularly polarized light (σ^+) to excite the atoms into the $^3\mathrm{P}_2$ state with Zeeman level $m_F = 11/2$. For the $^3\mathrm{P}_2$ state the linear Zeeman splitting in $^{87}\mathrm{Sr}$ is $\Delta_{\mathrm{Zeeman}} = 0.5$ MHz/G [13]. Our coils can achieve 0.8 G/(cm A) for the field gradient. With a current supply at 280 A, we are able to provide a gradient of 224 G/cm along the vertical direction, which, together with the 532 nm lattice spacing, leads to a magnetic field difference between adjacent layers of $\Delta B = 0.012$ G. Finally, we can calculate the frequency splitting between adjacent layers as $\Delta_f = \Delta_{\mathrm{Zeeman}} \cdot m_F \cdot \Delta B = 33$ kHz.

Similarly, for the bosonic atoms $^{88}\mathrm{Sr}$ the $^1S_0$-$^3P_2$ transition takes place between the $^1\mathrm{S}_0$(J=0) - $^3\mathrm{P}_2$(J = 2) states. Under the magnetic field, we drive the $^1\mathrm{S}_0$ state ($m_J = 0$) to the $^3\mathrm{P}_2$ state ($m_J = 1$) using σ^+ light. The linear Zeeman splitting in Sr^{88} is $\Delta_{\mathrm{Zeeman}} = 2.1$

MHz/G [13], and following the above argument we calculate the energy splitting between adjacent layers of ^{88}Sr to be 25 kHz.

In order to cleanly address and successfully isolate a single layer of Sr atoms, the transition linewidth has to be about an order of magnitude narrower than the splitting, and thus the linewidth of the laser facilitating the transition also has to be of this order. This leaves us with a narrow laser linewidth on the order of 1 kHz.

There are three parts involved in the realization of such a laser system: the generation of the single-mode laser light with sufficient optical power, which will be discussed in Chapter 3; the frequency stabilization of the light to an ultrastable reference cavity, which is discussed from Chapter 4 to Chapter 6; and the transport of the light with a fiber noise cancellation system, which is discussed in Chapter 7 and Chapter 8. Before we delve into the experimental details, we will first introduce in the next Chapter the working principles of a laser.

Chapter 2

Principles of Lasers

Controlling systems in the quantum regime is not an easy task. As quantum states tend to be extremely sensitive to perturbations, we need to make sure that we are only providing exactly what the quantum system needs when manipulating them. Moreover, due to the intrinsic wave nature of quantum objects, it is necessary to take their phase properties into account: whichever instrument we are using to address them, it must hold a highly consistent phase relation.

For us, the quantum systems we are interested are ultracold Sr atoms trapped in an optical lattice, and the most reliable tool enabling us to coherently address and manipulate these atoms, is called a laser. A laser (an acronym for Light Amplification by Stimulated Emission of Radiation) is a device that can produce highly directional monochromatic light with spatial and temporal coherence. In this Chapter, we will explore the working principles behind a narrow-linewidth laser system. The materials presented follow closely to Ref. [18] and Ref. [19], and interested readers are encouraged to refer to these excellent references for more in-depth discussions.

2.1 Interaction of Light and Matter

A laser exploits three fundamental phenomena that occur when an electromagnetic (EM) wave interacts with a material, namely spontaneous emission, stimulated emission, and the process of absorption. In the following we will give an introduction to these processes.

2.1.1 Spontaneous Emission and Nonradiative Decay

Let us start with a two-level quantum system with a ground state E_g and an excited state E_e representing atoms in the gain medium. An atom initially raised to the excited state has a natural tendency to decay back to its ground state, the more stable state, with a release of the transition energy $(E_e - E_g)$. If the transition energy is released in the form of an EM wave, the process is referred to as spontaneous or radiative emission, as sketched in Fig. 2.1(a). Because of energy conservation, the frequency ν_0 of the emitted radiation is given by $\nu_0 = (E_e - E_g)/h$, where h is Planck's constant. Note that this process occurs even if the atom is completely isolated from the environment. The origin of the spontaneous emission can be traced to the perturbation of the excited atom by the zero-point fluctuation of the electromagnetic vacuum where the averages of EM fields are nonvanishing even without the presence of a classical EM wave [20].

Now let us assume that at time t, the excited state has a population density n_e (number of atoms per unit volume). Atomic decay due to spontaneous emission follows an exponential law [18]:

$$\left(\frac{\mathrm{d}n_e}{\mathrm{d}t}\right)_{\mathrm{sp}} = -\frac{n_e}{\tau_s}, \tag{2.1}$$

with a spontaneous emission lifetime τ_s depending on the particular transition involved. The direction, polarization, and phase of the spontaneously emitted photons are all random and the overall emitted light from the given atom is thus said to be incoherent.

Different from the spontaneous emission, if the transition energy is released into a form other than EM radiation (e.g., into kinetic or internal energy of surrounding atoms via collisions), the process is referred to as nonradiative decay. Similar to the spontaneous emission process, the corresponding rate for nonradiative decay can also be expressed via an exponential law:

$$\left(\frac{\mathrm{d}n_e}{\mathrm{d}t}\right)_{\mathrm{nr}} = -\frac{n_e}{\tau_{\mathrm{nr}}}, \tag{2.2}$$

where τ_{nr} is the nonradiative lifetime. When both radiative and nonradiative decay are taken into account, the rate of decay of n_e becomes:

$$\left(\frac{\mathrm{d}n_e}{\mathrm{d}t}\right)_{\mathrm{decay}} = -\frac{n_e}{\tau_s} - \frac{n_e}{\tau_{\mathrm{nr}}} \equiv \frac{n_e}{\tau}, \tag{2.3}$$

where the time constant τ is referred to as the lifetime of the excited state.

2.1.2 Stimulated Emission and Absorption

If an EM wave with frequency ν close to the atomic transition energy ν_0 is incident onto the atom while in its excited state, the interaction of the wave with the atom can stimulate the atom to decay to its ground state with a simultaneous emission of EM radiation. This process is referred to as stimulated emission. In this case, one photon, with the same frequency ν, propagation direction, polarization state, and phase is emitted, as shown in Fig. 2.1(b). Stimulated emission is the fundamental mechanism behind a working laser which emits coherent light, and quantum mechanical calculations show that the process can be described by

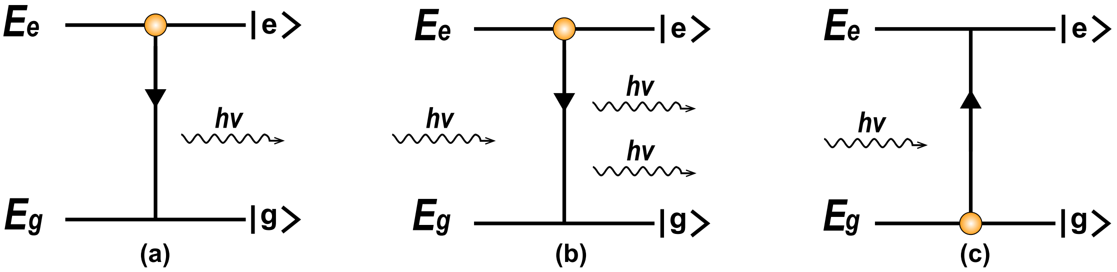

Figure 2.1 Fundamental interaction processes of a quantized atom with an EM wave. (a) Spontaneous emission. (b) Stimulated emission. (c) Absorption. Drawn following closely to Ref. [18].

$$\left(\frac{\mathrm{d}n_e}{\mathrm{d}t}\right)_{\mathrm{st}} = -W_{\mathrm{eg}}n_e, \tag{2.4}$$

where W_{eg} is the stimulated emission rate and is proportional to the photon flux via

$$W_{\mathrm{eg}} = \sigma_{\mathrm{eg}}F, \tag{2.5}$$

where F is the photon flux (number of photons passing unit area per unit time), and σ_{eg} is the stimulated emission cross section. Note that cross section is, in general, a measure of the probability that a specific process will take place when a radiant phenomenon such as a particle beam, sound wave, or light intersects a localized phenomenon (e.g. a particle) [21]. One can find an intuitive picture in Fig. 2.2(b), where each atom has a finite cross sectional area, and a light-atom interaction can only happen if the incoming photon enters through this effective area of interaction.

Now, let us consider the case of an atom initially in its ground state. In the absence of perturbations, the atom will rest stably in this state forever. However, if EM radiation of frequency $\nu \approx \nu_0$ is incident on the atom, there is a finite probability that one photon of the incoming wave will be destroyed and the atom be raised to the excited state. This process, as shown in Fig. 2.1(c), is referred to as absorption. Similar to stimulated emission, the absorption process follows:

$$\left(\frac{\mathrm{d}n_g}{\mathrm{d}t}\right)_{a} = -W_{\mathrm{ge}}n_g, \tag{2.6}$$

where W_{ge} is the rate of absorption. Again, W_{ge} is proportional to the photon flux and absorption cross section by $W_{\mathrm{ge}} = \sigma_{\mathrm{ge}}F$. Note that it can be shown that, for nondegenerate levels, the cross sections σ_{ge} and σ_{eg} are equivalent, leading to $W_{\mathrm{ge}} = W_{\mathrm{eg}}$ [22].

The calculation of the absorption and stimulated emission rates W_{ge} and W_{eg} can be carried out following a semiclassical approach, in which the atom is treated quantum mechanically whereas the EM wave classically [23, 24]. In this case, the incident wave induces an atomic transition via the coupling of the EM field with the electric and magnetic dipole (and multiple) moments of the atom. The dominant interaction is usually between the electric field $\boldsymbol{E}(t) = \boldsymbol{E_0}\cos(2\pi\nu t)$ of the EM wave and the electric dipole moment ($\boldsymbol{\mu}$) of the atom, with the matrix dipole element $\mu_{\mathrm{ge}} = \int \psi_e^*(\boldsymbol{r})e\boldsymbol{r}\psi_g(\boldsymbol{r})\mathrm{d}\boldsymbol{r}$, where $\boldsymbol{r}$ is the position of the electron relative to the nucleus, e is the electron charge, and $\psi_g(\boldsymbol{r})$ and $\psi_e(\boldsymbol{r})$ are the electronic eigenfunctions of the ground and excited states, respectively.

To obtain an explicit formula for the transition rate $W = W_{\mathrm{eg}} = W_{\mathrm{ge}}$, we will apply Fermi's golden rule which describes the transition probability Γ from the initial state $|i\rangle$ to a set of final states $|f\rangle$ as [20]:

$$\Gamma_{i\mapsto f} = \frac{2\pi}{\hbar}|\langle f|H'|i\rangle|^2\rho(E_f), \tag{2.7}$$

where $\langle f|H'|i\rangle$ is the matrix element of a perturbation H' between the final and initial states, and $\rho(E_f)$ is the density of states at energy E_f. For a perfectly-coherent interaction between a linearly polarized monochromatic EM wave and the atom, we can use a Dirac delta function for the density of states of the EM radiation and write the following expression based on Eqn. (2.7):

$$W = \frac{2\pi}{\hbar}|E|^2|\langle e|\hat{\boldsymbol{\epsilon}}\cdot\boldsymbol{\mu}|g\rangle|^2\delta(\nu-\nu_0), \tag{2.8}$$

where $|E| = E_0/2$ represents the average amplitude of the field, and $\hat{\boldsymbol{\epsilon}}$ specifies the wave polarization. If we generalize the linearly polarized EM radiation into an unpolarized isotropic radiation with the same amplitude in all directions: $|\boldsymbol{E}\cdot\hat{x}| = |\boldsymbol{E}\cdot\hat{y}| = |\boldsymbol{E}\cdot\hat{z}| = |E|^2/3$, we can write:

$$|\langle e|\hat{\boldsymbol{\epsilon}}\cdot\boldsymbol{\mu}|g\rangle|^2 = \frac{|\mu_{\mathrm{ge}}|^2}{3}, \tag{2.9}$$

where

$$|\mu_{\mathrm{ge}}|^2 = |\langle e|e\cdot x|g\rangle|^2 + |\langle e|e\cdot y|g\rangle|^2 + |\langle e|e\cdot z|g\rangle|^2. \tag{2.10}$$

And Eqn. (2.8) becomes:

$$W = \frac{4\pi^2}{3\hbar^2}U|\mu_{\mathrm{ge}}|^2\delta(\nu-\nu_0), \tag{2.11}$$

where $U = {E_0}^2/8\pi$ denotes the energy density for a linearly polarized monochromatic field [25].

2.2 Coherent Amplification of Light

Consider a medium made of a collection of two-level atoms with transition frequency ν_0, and consider a monochromatic EM plane wave with frequency $\nu \approx \nu_0$ propagating inside this medium along the z-direction. From the previous Section we see that there exists a one-to-one correspondence between the number of atoms decayed (excited) and the photons created (destroyed) through stimulated emission (absorption). Now if $F(z)$ is the photon flux of the EM wave at plane z, and n_e and n_g are the population densities of the excited and ground states of the atom, respectively, one can obtain the change dF of the photon flux due to the processes of absorption and stimulated emission along the elemental length dz of the material as:

$$\mathrm{d}F = \sigma(n_e - n_g)F(z)\mathrm{d}z, \tag{2.12}$$

where $\sigma \equiv \sigma_{\mathrm{eg}} \equiv \sigma_{\mathrm{ge}}$ is the transition cross section. We can see the photon flux change across an infinitesimal section dz of the amplifier in Fig. 2.2 (a). Note that we did not consider spontaneous and nonradiative decays here since nonradiative decay does not add new photons whereas spontaneous emission creates photons emitted in any direction and has negligible contribution to the incoming photon flux along a specific direction. Most importantly, from Eqn. (2.12) we find that for $n_e > n_g$, we have dF/dz > 0, which means that the medium acts as a coherent optical amplifier through which the EM wave is amplified. Conversely, for $n_e < n_g$, one has dF/dz < 0 and the medium behaves as an absorber.

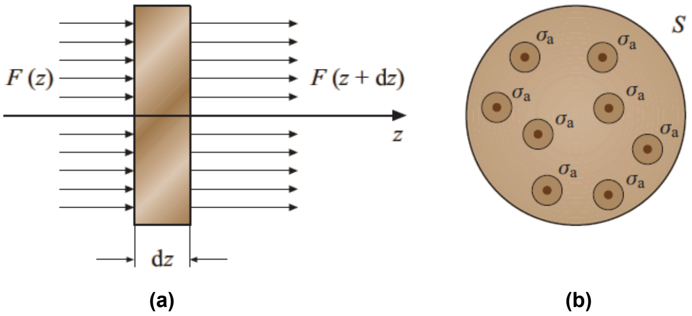

Figure 2.2 Coherent amplification of an EM wave. (a) Photon flux-balance diagram in an infinitesimal section dz of the amplifier, where $F(z)$ is the photon flux at a given plane z. (b) Conceptual illustration of the transition cross section σ_a for atoms in a gain medium with transverse cross section S. Adapted from Ref. [18].

If we let l be the length of the medium, by integrating Eq. (2.12) we find that the photon flux $F(l)$ at the output plane can be given by $F(l) = F(0)\exp(g)$, where $g = (n_e - n_g)\sigma l$ is the gain coefficient. The condition for light amplification ($g > 0$) is therefore $n_e > n_g$, which is often referred to as population inversion. We note that in the previous calculation

n_g and n_e have been assumed independent of the intensity I of the propagating wave. This assumption is valid provided that the light intensity $I = F(h\nu)$ is weak enough that changes of n_e and n_g due to absorption and stimulated emissions can be neglected.

2.2.1 Population Inversion: the Pumping Process

At thermal equilibrium, the distribution of population densities n_e^{eq} and n_g^{eq} is described by Boltzmann statistics:

$$\frac{n_e^{\mathrm{eq}}}{n_g^{\mathrm{eq}}} = \exp\left(-\frac{E_e - E_g}{k_B T}\right), \tag{2.13}$$

where k_B is the Boltzmann constant, and T is the temperature. Note that since $E_e > E_g$, any material will behave as an optical absorber at thermal equilibrium. Therefore, we need to artificially create population inversion in the medium for optical amplification by means of a pumping process [26], driving the population distribution far from thermal equilibrium. However, a system with only two levels cannot achieve population inversion, because when n_g reaches the same value as n_e, absorption and stimulated emission processes will compensate each other: a phenomenon referred to as the saturation of the two-level system.

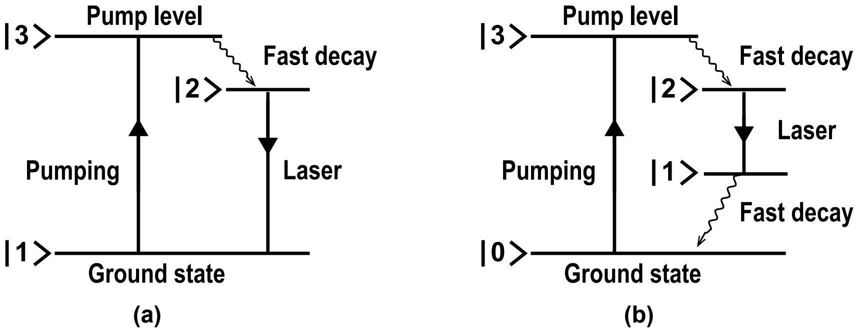

Figure 2.3 Drawings of the energy-level diagram for (a) a three-level laser, and (b) a four-level laser. Drawn following Ref. [18].

Population inversion can be achieved, however, when more than two levels are considered. Typically three or four energy levels are involved. In a three-level laser shown in Fig. 2.3 (a), atoms are raised from the ground level $|1\rangle$ into level $|3\rangle$ through a pumping mechanism. If the material is such that, once an atom excited into level $|3\rangle$ rapidly decays into a lower level $|2\rangle$ (by, e.g., a fast nonradiative decay), then population inversion can be obtained between level $|2\rangle$ and $|1\rangle$. Note that, in a three-level laser scheme, to achieve population inversion it is necessary to raise at least half of the atoms from the ground state $|1\rangle$ to state $|3\rangle$. In a four-level laser shown in Fig. 2.3 (b), atoms are again raised from the ground level $|0\rangle$ to an excited state $|3\rangle$, with a rapid decay to the upper laser level $|2\rangle$; however, this time laser action takes place from level $|2\rangle$ to an excited lower-lying level $|1\rangle$. Once laser oscillation starts, level $|1\rangle$ is populated by stimulated emission; therefore to maintain population inversion in stationary conditions, the lower laser level $|1\rangle$ should also be able to rapidly depopulate, e.g., via a fast nonradiative decay into the ground level $|0\rangle$. Compared to a three-level laser, the four-level laser offers the great advantage that population inversion is ideally achieved when just one atom is raised to the pumping level $|3\rangle$. Four-level lasers are thus more used, whenever possible, than three-level lasers. One can characterize the rate of population change of the upper laser level $|2\rangle$ due to pumping by:

$$\left(\frac{\mathrm{d}n_2}{\mathrm{d}t}\right)_p = W_p n_g, \tag{2.14}$$

where W_p is the pumping rate and n_g is the ground state population density. For a four-level laser, one can assume n_g to be constant and much larger than n_2. In this case we can write from Eqn. (2.14) a constant pump rate: $(\mathrm{d}n_2/\mathrm{d}t)_p = R_p$, where $R_p = W_p n_g$ is the pump rate per unit volume.

The energy required for pumping is generally supplied either optically or electrically. In optical pumping, the pumping source can be a powerful lamp with incoherent light, or a laser with highly coherent light. In electrical pumping, the excitation mechanism usually consists of an electrical current flow through the active medium. Although optical pumping can be used for semiconductor lasers (the type of laser we are interested in), electrical pumping proves to be much more efficient [18] and is thus the pumping mechanism used in our diode lasers.

2.3 Laser Oscillation

A laser is a coherent optical oscillator which generates a coherent signal through resonant oscillation without an input signal [19]. Besides the optical amplification mentioned above, positive optical feedback is required for the laser oscillation. This requirement is fulfilled by placing the gain medium between two mirrors, forming a laser cavity. As we can see from Fig. 2.4, laser photons undergo multiple reflections within the cavity, being amplified at each pass through the laser medium. In this case one mirror (total reflector) with reflectivity R_1 close to 100% reflects almost all the incident light back, while the other mirror (output coupler) with reflectivity R_2 smaller than 100% transmits a fraction $T_2 = 1 - R_2$, which constitutes the output laser beam.

The combination of laser gain medium, pumping source and optical cavity forms a simple laser oscillator: if the amplification is large enough to overcame losses, i.e., when a threshold condition is reached, a single photon can be amplified by several orders of

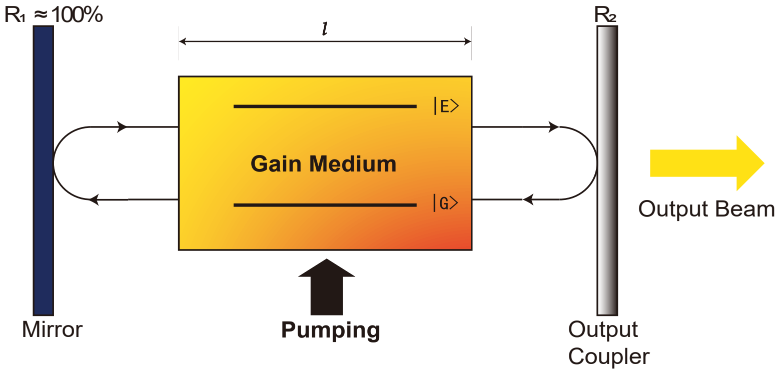

Figure 2.4 Schematic of a laser oscillator. The gain medium is placed in between two mirrors with reflectivity R_1 and R_2, which provide positive optical feedback for laser oscillation. In this way, light propagating along the cavity axis and passing through the pumped laser medium is reflected back through it, stimulating further emission in the same direction. Drawn following Ref. [19]

magnitude to produce a large number of coherently generated photons trapped inside the resonator.

2.3.1 Cavity Photon Lifetime

The modes of an optical resonator are defined as the stationary or weakly damped field distributions that can be sustained inside the cavity and satisfy the boundary conditions imposed by the cavity mirrors [19]. We note that since the mirror reflectivity of the output coupler is always smaller than 100%, a fraction of the photons ϕ stored in the cavity escapes from the resonator at each round-trip. We can, in general, model the electric field for a given mode in a leaky resonator as [18]:

$$\boldsymbol{E}(x,y,z,t) = \boldsymbol{a}(x,y,z)\cos(\omega t)\exp\left[\frac{-t}{2\tau_c}\right]\ (t>0), \tag{2.15}$$

where $\boldsymbol{a}(x,y,z)$ is the spatial distribution of the field, ω is the resonance frequency, and the field amplitude follows an exponential decay law characterized by τ_c, the cavity photon lifetime.

To calculate the rate of energy decay in a given cavity mode, let I_0 be the initial intensity corresponding to the field amplitude at a given point in the cavity, R_1 and R_2 be the reflectivities of the two mirrors, and L_i the fractional internal loss per pass due to scattering and absorption losses of intracavity optical elements. The intensity at the same point after one round-trip time $\tau_R = 2L_e/c$ (L_e is the cavity optical length) is:

$$I(\tau_R) = R_1 R_2 (1 - L_i)^2 I_0 = I_0 \exp(-2\gamma), \tag{2.16}$$

where γ is the logarithmic loss per pass defined is:

$$\gamma = \frac{\gamma_1 + \gamma_2}{2} + \gamma_i, \tag{2.17}$$

with $\gamma_1 = -\ln(R_1)$, $\gamma_2 = -\ln(R_2)$, and $\gamma_i = -\ln(1 - L_i)$. In view of the exponential decay law introduced in Eqn. (2.15), after a round-trip time we have $I(\tau_R) = I_0 \exp(-\tau_R/\tau_c)$. We can thus conclude that the cavity photon life time is:

$$\tau_c = \frac{\tau_R}{2\gamma} = \frac{L_e}{c\gamma}. \tag{2.18}$$

2.3.2 Laser Rate Equations

A simple and powerful approach for understanding the basic dynamical behavior of a laser oscillator is based on a rate equation model, in which simple balance equations for the total number of atoms undergoing a transition and the total number of photons created or annihilated are written [22]. We can derive the laser rate equations for a four-level laser scheme depicted in Fig. 2.3 (b) with the following assumptions: (1) the lifetime τ_1 of the lower laser level $|1\rangle$ is short enough that we may neglect the population in level $|1\rangle$; (2) a single longitudinal and transverse mode is oscillating in the cavity; (3) laser transition is homogeneous for all atoms in the gain medium; (4) we neglect the precise spatial variation of the cavity mode, and (5) pumping of the gain medium is uniform. Under these assumptions, we can write the following rate equations for the population inversion $n = n_2 - n_1 \simeq n_2$ and the total number of photons ϕ of the oscillating mode stored in the cavity:

$$\frac{\mathrm{d}n}{\mathrm{d}t} = R_p - B\phi n - \frac{n}{\tau}, \tag{2.19}$$

$$\frac{\mathrm{d}\phi}{\mathrm{d}t} = -\frac{\phi}{\tau_c} + V_a B \phi n, \tag{2.20}$$

where R_p is the pump rate per unit volume, τ is the lifetime of the upper laser level $|2\rangle$, τ_c is the cavity photon lifetime describing the field decay due to cavity losses, V_a is the volume occupied by the cavity mode inside the gain medium, and B is the stimulated transition rate per photon per mode. Note that $B\phi n = W_{21} n = (\sigma c/V) n$ is the number of atoms per unit volume and unit time that decay creating a photon, with σ being the transition cross section. In Eqn. (2.19), the terms on the right-hand side represent the pumping process, stimulated emission, and spontaneous and nonradiative decay, respectively. In Eqn. (2.20), the first term on the right-hand side represents the number of cavity photons lost per unit time due to losses of the cavity (i.e., internal loss, diffraction loss and output coupling), and the the second term represents the number of photons (per unit time) that are created by stimulated emission. Note that spontaneous emission is not included in Eqn. (2.20) as only a negligible fraction of spontaneously emitted photons belongs to the oscillating mode.

The laser output power P_{out} is related to the photon number ϕ by the relation:

$$P_{\text{out}} = \frac{(h\nu)\phi}{\tau_c} \cdot \frac{\gamma_2}{2\gamma}, \tag{2.21}$$

where $(h\nu)\phi/\tau_c$ is the total EM energy lost in the cavity per unit time, and solely a fraction $\gamma_2/2\gamma$ of this power is available from the transmission through the output coupler.

2.3.3 Threshold Condition

There exits a threshold condition above which the amplification will outweigh losses in the system allowing laser oscillation to take place. The critical population inversion n_c needed to reach the threshold condition can be simply obtained from Eqn. (2.20) by imposing $\mathrm{d}\phi/\mathrm{d}t = 0$. Solving this equation yields the critical inversion as:

$$n_c \equiv \frac{1}{\tau_c B V_a} = \frac{\gamma}{\sigma l}. \tag{2.22}$$

Accordingly, the critical pump rate (per unit volume) corresponding to the threshold condition is $R_{\text{cp}} = n_c/\tau$ (recall that τ is the lifetime of the upper laser level $|2\rangle$), and the related minimum pump power is thus $P_{\text{cp}} = R_{\text{cp}} V h\nu$.

For a pump rate $R_{\text{p}} > R_{\text{cp}}$, the rate equations (Eqn. 2.19, Eqn. 2.20) admit the following solution [18]:

$$n = n_c, \tag{2.23}$$

$$\phi = [1/(B\tau)](x-1), \tag{2.24}$$

corresponding to laser being above threshold as shown in Fig. 2.5, where $x = R_p/R_{\text{cp}} = P_p/P_{\text{cp}} > 1$ is the above-threshold pump behavior parameter. Once the number of photon ϕ is known, we can simply plug it to Eqn. (2.21) to obtain the corresponding output power P_{out}.

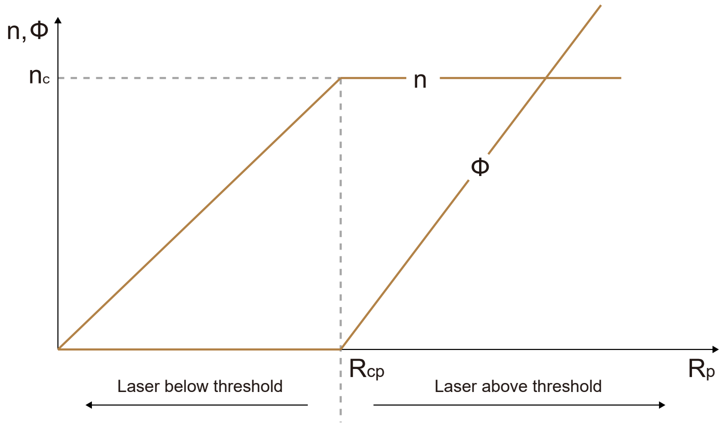

Figure 2.5 Behavior of population inversion n and photon number ϕ in the oscillating mode versus the pump rate R_p for a four-level laser. R_{cp} is the critical pump rate above which laser action takes place. Drawn with close reference to Ref. [18].

2.3.4 Laser Resonators and Modes

As discussed in the previous sections, the gain medium of a laser oscillator is placed inside a laser resonator or laser cavity, which is capable of trapping a stationary or weakly damped EM field at some selected frequencies. Such EM field configurations are called cavity modes. Due to the scope of this thesis, we will only focus on the general picture of cavity modes in this section, but readers are welcome to refer to Refs. [18, 22, 27] for further mathematical details.

The most widely used cavities for lasers are open cavities, composed of at least two plane or spherical mirrors of circular shape. The optical cavity is open to reduce tremendously the number of modes that can oscillate with low loss in the cavity. In fact, if the cavity were closed, the number N of resonant modes whose resonance frequency falls within the gainline of the amplifying medium is approximately given by:

$$N \approx \frac{8\pi\nu^2}{c^3} V \Delta\nu_0, \tag{2.25}$$

where $(8\pi\nu^2/c^3)$ is the density of modes, $\Delta\nu_0$ the linewidth of the gain medium, and V the cavity volume. To estimate N, let us consider a common narrow-linewidth gain medium, such as the λ = 633 nm transition of the HeNe laser ($\Delta\nu_0 = 1.7$ GHz) [18] . Assuming a cylinder cavity with length L =50 cm and a lateral diameter d = 3 mm, we find that the total number of cavity modes that fall under the gainline of the HeNe laser is $N \approx 1.2 \times 10^9$, which is unacceptably large and seriously limits the laser performance for subtle quantum-optical tasks.

Contrary to the closed cavity, an open resonant cavity is able to drastically reduce the number of oscillating modes down to a single or only a few modes by exclusively making the modes traveling nearly parallel to the resonator axis experience low losses to allow for laser oscillation. Therefore, in an open cavity, the oscillating modes are expected to be tightly confined around the optical axis and propagating paraxially along it, making the output laser beam highly directional.

The open cavity modes and the corresponding resonance frequencies can be characterized by three integer numbers n, m and l, which are called mode indices. The latter two indices m and l are transverse field indices determining the field distribution in the plane orthogonal to the paraxial resonator axis, whereas the index n defines the field distribution along the resonator axis and is called the longitudinal mode index. The index n, in particular, gives the number of longitudinal nodes of the standing wave. For spherical mirrors with sufficiently wide apertures, transverse modes are expressed by Gauss-Hermite or Gauss-Laguerre functions, depending on rectangular or circular boundary conditions. In particular, the leading-order mode corresponding to transverse mode indices $m = l = 0$ is a Gaussian beam and represents the most common transverse field distribution of any output laser beam. For this reason, the study of laser modes is closely related to the propagation properties of Gaussian (or Gauss-Hermite) beams.

One can also refer to the above laser beams as $\mathrm{TEM}_{\mathrm{lm}}$ beams, where TEM stands for transverse electric magnetic, as both electric and magnetic fields of the EM wave are approximately transverse to the z-direction. As we can see from Fig. (2.6), for a $\mathrm{TEM}_{\mathrm{lm}}$ beam, the intensity distribution consists of $l + 1$ lobes in the horizontal direction and $m + 1$ lobes in the vertical direction.

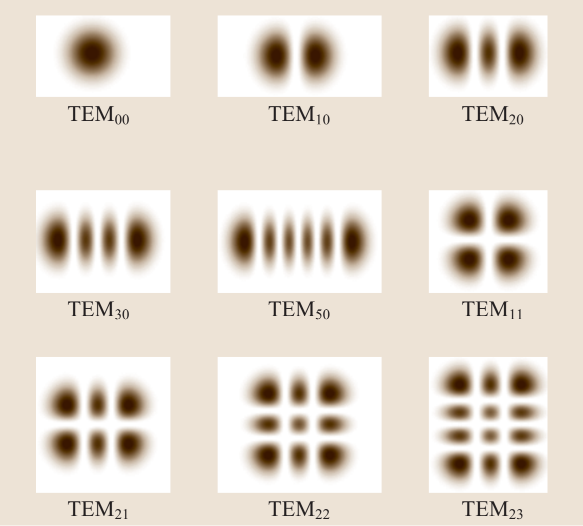

Figure 2.6 Grey scale intensity patterns of a few low-order Hermite–Gaussian modes. Adapted from Ref. [18].

Chapter 3

Setup of the Linear External Cavity Diode Laser

As having previously discussed, if we aim at addressing the $^1S_0$ - $^3P_2$ transition with high fidelity, we need to employ a narrow-linewidth laser at 671 nm. In Chapter 2 we talked about the theoretical aspects behind the lasing process, and now we will focus on the experimental realization and characterization of such a laser system in our lab. Our design is that of an diode laser with a linear external cavity (ECDL). Basically, instead of forming the laser oscillator inside the diode, an ECDL increases the tunability of the laser light by decoupling the wavelength-selection from the optical feedback for laser oscillation. The linear configuration also greatly suppresses the change of laser frequency due to variation of the cavity length, making the system robust against any horizontal compression or expansion of the cavity.

3.1 Setup of the ECDL

3.1.1 Overview of the Laser Housing

The laser housing for our linear ECDL system is made from aluminum with approximately 10 mm thick walls, which help to prevent external noise from reaching the laser cavity. At the mean time, the metal housing acts as a Faraday cage, shielding the laser diode from radio-frequency (RF) signals in the lab environment which can disturb the laser output frequency by influencing the diode forward current. The laser housing consists of a lid and a bottom plate with a Viton ring placed in between. Once closed, the laser house can be made air-tight and evacuable via a KF gasket on the top of the lid for better isolation from external temperature and air pressure fluctuations, as shown in Fig. 3.1 (a). Laser light generated inside the housing is output via a wedged window (WW11050-B) placed into the tilted insert on the lid. The window is tilted to prevent back-reflection into the cavity and is wedged to eliminate etaloning effects in the transmitted and reflected components of the laser light.

The essential components of our ECDL design are captured by Fig. 3.1 (b) and Fig. 3.1 (c). All the optical components in Fig. 3.1 (parts ***a***-***d***) are contained in a monolithic aluminum mount on the bottom plate to ensure maximum stability. The aluminum mount rests on two Peltier elements, which, together with a thermistor attached close to the collimation tube, provide temperature stability for the system. Two electronic connectors are attached on the back end of the bottom plate: the left one is responsible for the Peltier elements for temperature tuning, and the right connector sends the forward current to the diode and controls the piezo voltage.

We use a Schäfter + Kirchhoff 20C-A4.5-07 collimation tube shown in Fig. 3.1 (part $\boldsymbol{d}$) to provide electric isolation and collimation to the diode. The diode is mounted at the back end of the collimation tube and its light is collimated through the lens mounted on the other end of the tube. Note that for a beam with different divergence angles along the horizontal and vertical directions, the collimating lens inside the tube can only fully collimate one direction (usually the direction with larger divergence), while the other direction needs to be collimated by further beam shaping techniques discussed later in this chapter.

The first optical element in the beam path after the collimation tube is an interference filter as can be seen in Fig. 3.1 (part $\boldsymbol{c}$). This filter passes one specified wavelength band while blocking others, enabling frequency adjustment of the laser light. By varying the angle of incidence by a small amount from normal incidence, the wavelength of the transmitted laser light can be effectively tuned over a narrow range. However, large changes in the incident angle may significantly distort the shape of the passband and, more importantly, cause a significant decrease in the transmittance of the passband [28].

As shown in Fig. 3.1 (part $\boldsymbol{b}$), the next element that the beam passes is a lens that focuses light on the output coupler. The output coupler in Fig. 3.1 (part $\boldsymbol{a}$) is a partially transmissive mirror reflecting 30% of the light back into the laser diode to form laser oscillation. The distance between the diode to the output coupler is 10 cm, leading to a free spectral range (FSR) of 1.5 GHz. Directly attached to the output coupler is a piezo ring shown in Fig. 3.1 (part $\boldsymbol{a_1}$). The piezo, driven by an external voltage, serves as another wavelength-selective element for fine tuning of the laser frequency via modulation of the cavity length. The last optical element in the laser body is a second lens shown in Fig. 3.1 (part $\boldsymbol{b}$), which collimates the final output beam.

3.1.2 Custom Laser Diode Protection Board (Version 2.0)

We employ a new version of the laser diode protection board (Laser Adapter V2.0) for the $^1\mathrm{S}_0$-$^3\mathrm{P}_2$ laser system. The electronic schematics and a picture of this board are shown in Fig. 3.2. The main purpose of this customized adapter board used on top of the commercial Toptica (DC 110 19”) current controller is to provide better filtering of the laser diode current, as possible noise on the current can be directly modulated onto the laser light, resulting in an increase of the laser linewidth. In addition to noise filtering elements, the board also allows for direct modulation of the laser diode current with a modulation circuit, which is important for the feedback loop in the PDH locking scheme explained

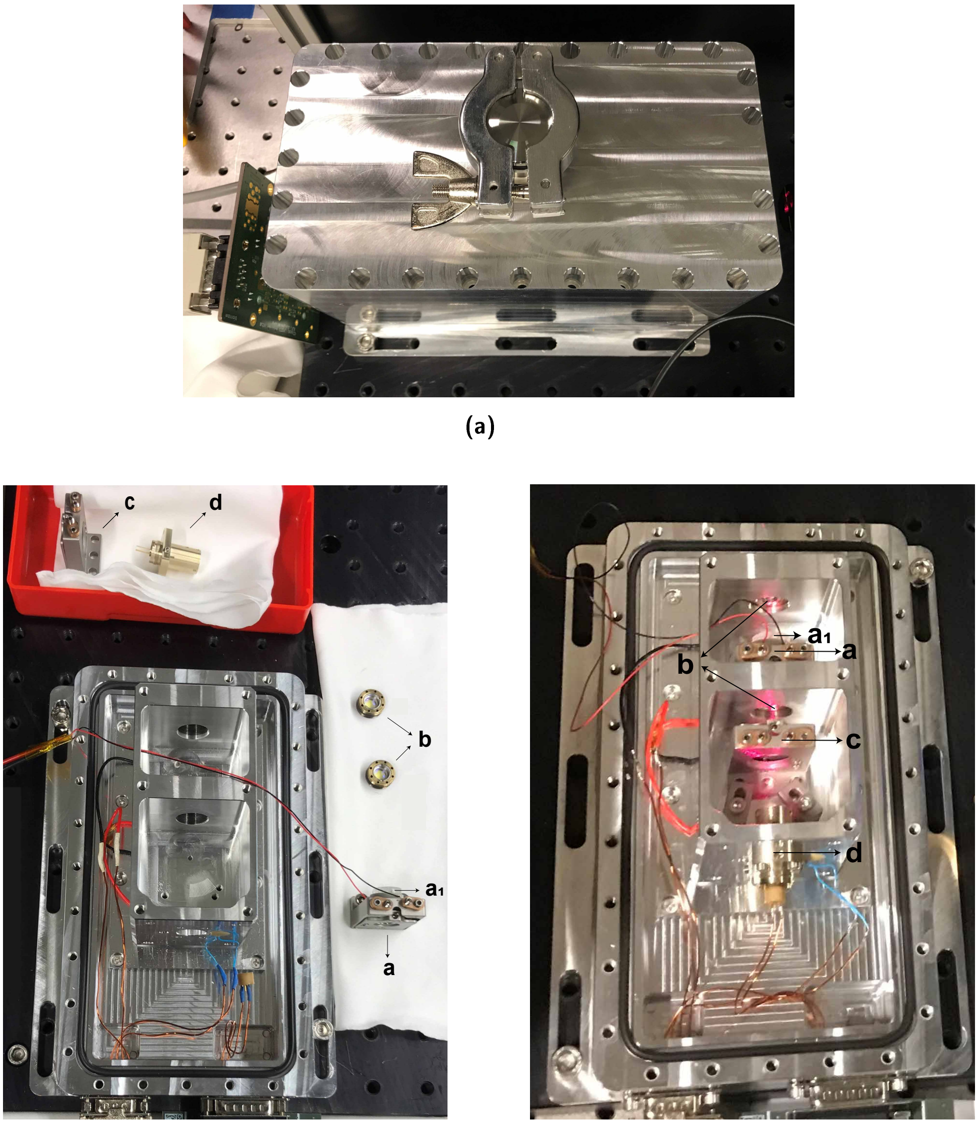

(a)

(b)

(c)

Figure 3.1 External Cavity Diode Laser. (a) A closed laser housing attached with the corresponding laser protection board. The system is evacuable via a KF gasket on the top of the lid. (b) and (c) Bottom plate of the ECDL with unassembled and assembled laser body, respectively. The laser body rests on two Peltier elements for temperature adjustment (beneath the central aluminum mount). A collimation tube (part d) electrically isolates the diode and collimates the output beam. The interference filter (part c) provides a first rough frequency selection. The laser diode together with the output coupler (part a) forms the external cavity, of which the length can be tuned with the piezo ring (part a_1). The first lens (part b) focuses the beam on the output coupler, while the second lens (part b) collimates the final beam.

later in this thesis. The major changes of the board compared to the previous version include: (1) vertical orientation for connection to the laser housing to get a more compact setup; (2) spatial separation of the piezo and laser diode currents to avoid cross-talk; (3) designated room for extra metal case around the board for better shielding from radio-frequency signals; and (4) more flexibility in replacing different circuit components for various modulation properties.

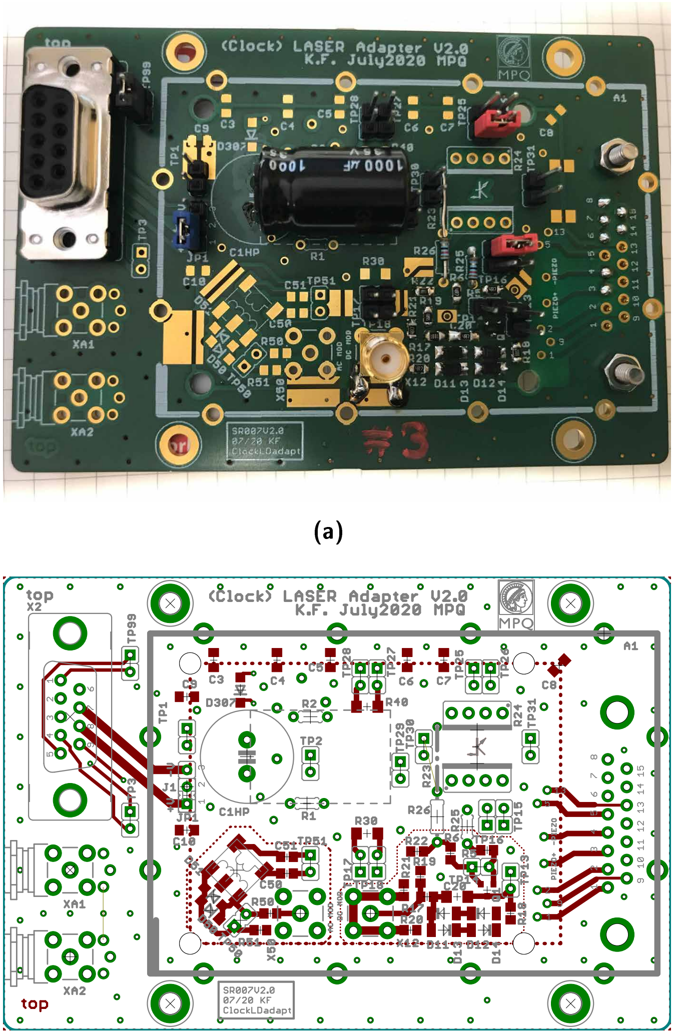

(a)

(b)

Figure 3.2 (a) A real picture of the V2.0 laser diode protection board. (b) Layout for the protection board design.

To test the modulation bandwidth, we send an oscillating voltage signal (with amplitude 50 mVpp) into the board and measure the light intensity fluctuation with a 20 MHz photodiode. The resulted optical power at various modulation frequencies is presented in Fig. (3.3), from which we find a 3 dB bandwidth of 7.8 MHz. As the typical modulation frequency for laser stabilization via PDH locking in the lab is expected to be below 5 MHz (which is approximately the bandwidth of the previous-version (V1.0) adapter board), the V2.0 board fulfills its job for us.

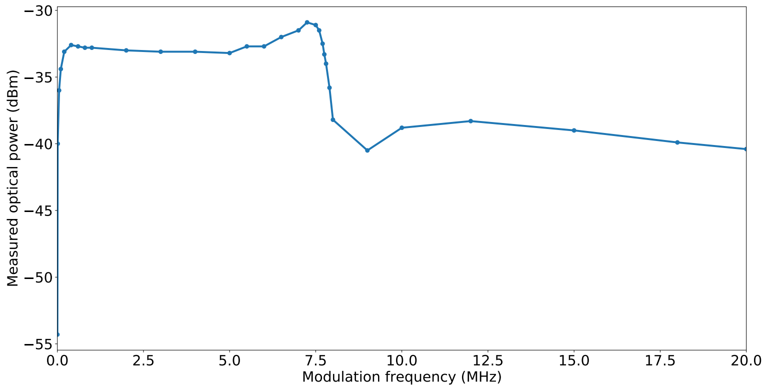

Figure 3.3 Ability to modulate the laser light at various modulation frequencies. Note that the 3 dB bandwidth of the V2.0 protection board is at 7.8 MHz.

3.1.3 Laser Diode Collimation

Do's and Don'ts when Handling a Laser Diode

Working with laser diodes is a task deserving the ultimate precaution, as careful and proper handling of laser diodes are critical to ensuring optimum laser-diode lifetimes. Before delving into the details of diode collimation for our ECDL, let us first go through the basic safeguards for working with a diode.

First and foremost, we need to pay great attention to the electrostatic discharge (ESD). Keep in mind that laser diodes are extremely sensitive to electrostatic discharge, excessive current levels, and current spikes (transients). Symptoms of damage include reduced output power, threshold-current shift, beam-divergence changes, difficulty focusing, and ultimately failure to lase [29]. To avoid damages caused by ESD, we must follow the following measures: (1) wear protective wrist straps designed to drain built-up electric charges safely to ground; (2) all tools that may contact the laser must be continuously grounded; (3) place unprotected laser diodes on static dissipative work surfaces; (4) when not working with the laser diodes, completely enclose them in conductive, shielded material; (5) keep all charge-generating materials away from unshielded diodes, which can become charged inductively; and (6) if possible, wear clothing resistant to charge creation.

Additionally, keep in mind to always double check the pin configuration before plugging current into the diode, especially make sure we do not have a mirrored image in our minds. Moreover, after plugging the diode into the driving socket, make sure the pins are not electrically connected to each other before turning on the power by measuring the resistance between the different pins.

Laser Diode Information

The laser for the $^1S_0$ - $^3P_2$ transition at 671 nm is built with a diode from Eagleyard Photonics (EYP-RWE-0670-00703-1000-SOT02-0000) [1]. The laser diode is anti-reflection coated and designed specifically for ECDL systems. This coating is essential for the linear ECDL to work, as it prevents the formation of an internal cavity between the gain medium and the diode window, which would otherwise compete against each other and reduce the frequency stability of the laser system. The diode is designed to output a single spatial (transversal) mode of TEM_{00} with a center wavelength at 668 nm and a tuning range from 665 nm to 675 nm, covering our desired wavelength at 671 nm. Note that this diode has a small beam divergence of 10 ° along the horizontal direction and a large divergence of 29 ° along the vertical direction.

Mounting the Diode into the Collimation Tube

With the aforementioned diode safety measures in mind, we will now discuss the procedures for obtaining a centered and collimated laser diode beam from the Schäfter + Kirchhoff 20C-series collimation tubes. Before we start to mount the diode, we need to first inspect the inside of the collimation tube, especially the ceramic insulation ring, so that there are no swarfs causing short circuits. Once we are sure that the tube is clean, we can go ahead to slowly insert the diode shown in Fig 3.4 (part a) into the collimation tube with respect to the index of the housing. Try to center the laser diode as much as possible before inserting the orange insulation ring depicted in Fig 3.4 (part b). Make sure the three grub screws on the metal retaining ring in Fig 3.4 (part c) point outside when assembling it. Slightly tighten the retaining ring so that it pushes and stabilizes the diode with a gentle pressure.

For adjustment of the laser diode and the collimating lens, the power supply has to be powered on. Note that particular care must be paid to the connection of the diode with its current socket. We need to ensure a firm and tight connection as shown in Fig. (3.5), because a loose connection can lead to damage when repositioning the laser at later stages. Since the diode pins can be easily bent when we plug them into the socket, we have to proceed very slowly and carefully. Here we only use a small forward current

---

[1] It happens that there exists some technical difficulties in engineering high-power single-mode diodes at 671 nm. The Eagleyard diode, with a specified power of 25 mW, is the most powerful diode with high-quality beam that we can find in the market.

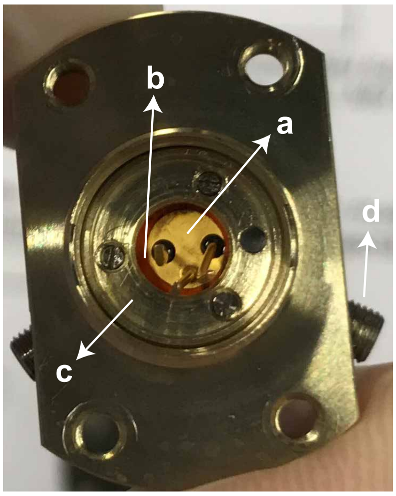

Figure 3.4 A Schäfter + Kirchhoff 20C-A4.5-07 collimation tube mounted with the diode. (a) The slicing laser diode. (b) Insulation ring (orange). (c) Metal retaining ring. (d) Adjustment screws for centering the diode, which need to be replaced once the diode-centering process is completed.

slightly above the specified laser threshold. Additionally, we need to avoid back reflection of the laser light into the laser diode by, e.g., keeping an angle between front face of the collimator and sensor (beam profiler) used to display the collimated laser beam. Before the start of the adjustment process, we need to check that the grub screw in the middle of the collimation tube responsible for tightening the collimating lens is only slightly tightened and that the collimation lens can be moved by the excenter key (60EX-4) without force.

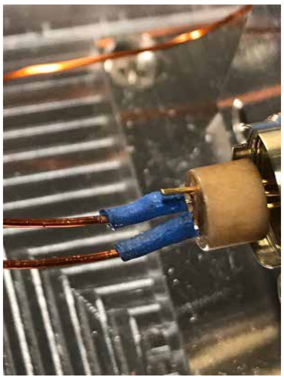

Figure 3.5 Connection of the laser diode with its current socket. It is important to connect them tightly and firmly, as a loose connection can increase the risk of diode damage.

Now, insert the excenter key in the collimator and turn it to adjust the distance between the pre-adjusted diode and the lens. Note that this step (as well as the following step) requires great patience, as the output beam is extremely sensitive to the tuning of the lens, and it is easy to completely overdo it at the first several trials.

Once we have a minimum-radius output light spot in the far field (several meters away), we can proceed to further center the diode via three centering screws. Keep in mind that we must loosen the two opposing screws before fastening the other one. We adjust the centering screws to make sure the beam hits the center of an alignment target placed at multiple positions. Another way to check if the diode is truly centered is by rotating the collimation tube, from which we will find that the collimated laser beam is moving on a circle around the axis of the collimator. Therefore, the diode can be centered by minimizing this radius. Again, because the involved components are too close to the light source, the output beam could be extremely sensitive to any adjustment action done to the collimation tube, thus the centering process has to be done gradually with the collimation of the lens due to the mutual effect: tightening the grub screws for the collimation lens may decenter the collimated laser beam, while the laser diode adjustment and locking of the retaining ring affects the collimation.

Note that there are two sets of centering screws: the shorter ones are for long-term locking of the diode position, and the longer ones are for adjustment and should be replaced with the shorter ones after centering the diode. When using the adjustment screws, the housing of the laser diode collimator is electrically connected to the housing of the laser diode. All adjustment equipment thus must be floating with high impedance to ground during the process.

For the final steps, tighten the screws for the collimation lens. Then tighten the three grub screws on the back retaining ring to lock the position of the laser diode. At last, replace the three longer screws used to adjust and center the diode with the locking screws, which, once screwed in, are detached from the outer case of the tube and allow insulation for the laser diode from the collimator housing.

Solving the Issue of Beam Clipping

Because of the structure of laser diodes, the divergence of the beam is greater along one axis (known as the fast axis), leading to an elliptical beam shape shown in Fig. 3.6 (a). For our case, the divergence along the fast axis is very large (29 °) and tends to cause the beam to be clipped by the edges of the lens inside the collimation tube. The interaction of the light with the lens edge creates a diffraction pattern that manifests as side peaks along the edges, forming a striped pattern in its (near field) beam profile, as can be seen in Fig. 3.6 (b). Note that though this diffraction pattern changes shape as the beam propagates and eventually disappears in the far field [31], the beam can only resemble the fundamental mode again at least several meters away, which is unpractical for optical setups in actual experiments. Efforts have been made to search for the optimal collimation lens of which the focal length is as large as possible to allow for more prominent collimation effects whilst short enough to compensate for the high divergence of the diode.

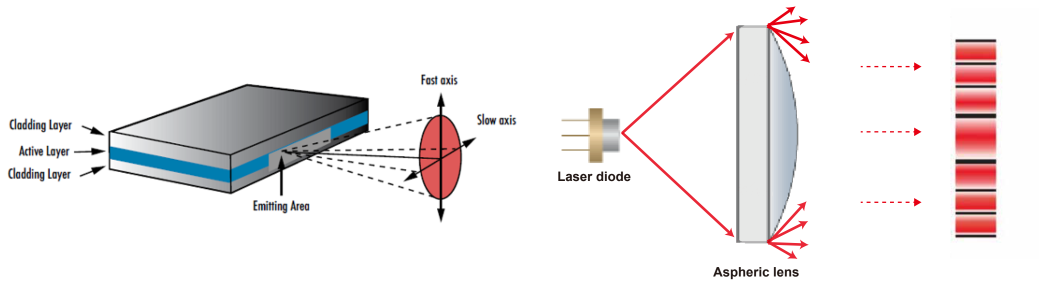

(a) **(b)**

Figure 3.6 Schematic diagrams of the diode elliptical beam shape and the issue of clipping. (a) Laser diodes with no collimating optics will have different divergence angles in the x- and y-axes because of the rectangular shape of the diode's active region, resulting in elliptical beam shapes. Adapted from Ref. [30]. (b) Light (along the fast axis) of the diode hits the edge of the aspheric lens due to the large divergence angle. Clipping at the collimating lens then degrades the original (Gaussian) beam profile by creating diffractive peaks along the propagation path.

We started with the 20CL-A4.5-02 (Schäfter + Kirchhoff) lens with focal length $f' = 4.5$ mm. However, as can be seen from Fig. 3.7 (c), the beam is terribly clipped at the edge of the collimating lens. The next two available lenses are the 20CL-A4-02 lens with $f' = 4$ mm, and the 20CL-A3.1-02 lens with $f' = 3.1$ mm. It turns out that the beam is so divergent that a focal length of 4 mm is still too long to prevent clipping, as can be seen in Fig. 3.7 (b). Fortunately, we find that at $f' = 3.1$ mm, the central part of the beam where the most power is concentrated, can pass freely without being clipped. Since the $f' = 3.1$ mm lens has the largest focal length without leading to clipping, we choose this one as the collimation lens for our laser diode.

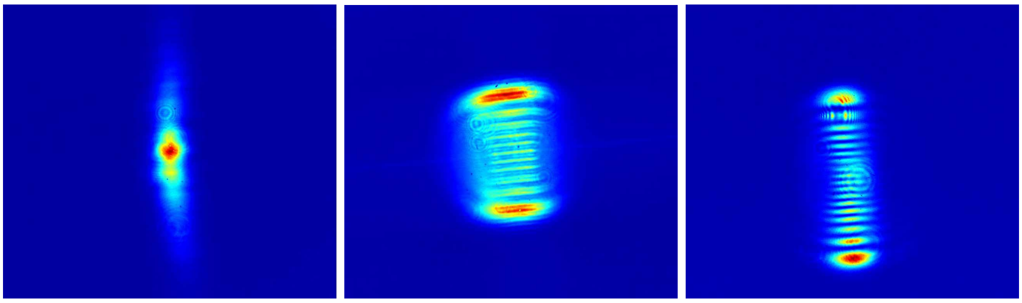

(a) **(b)** **(c)**

Figure 3.7 Diode beam profiles with different Schäfter + Kirchhoff collimator lenses. (a) Beam profile from lens (20CL-A3.1-02) with focal length $f' = 3.1$ mm. The central region where the fundamental mode is concentrated is not clipped by this lens. (b) Beam profile from lens (20CL-A4-02) with $f' = 4.0$ mm. The beam is substantially clipped and we cannot rely on this lens for further experiments. (c) Beam profile from lens (20CL-A4.5-02) with $f' = 4.5$ mm). The beam is being badly clipped as well. (All beam profiles were observed on the CINOGY - CinCam CMOS 1201 Nano beam profiler).

3.2 Characterizing the Laser

3.2.1 Output Power and Threshold Current

As discussed before, the threshold of a laser corresponds to the minimum pumping power required to reach the critical population inversion, at which the gain balances the losses of the resonator. According to Eqn. (2.24), the output light intensity is inversely proportional to the critical pump rate, thus by optimizing the optical properties of the laser resonator, we can lower the threshold current and improve the lasing efficiency to deliver more optical power. Moreover, the improved intracavity power circulation can also ensure a better stability of the lasing mode [32]. It is thus desired to obtain a threshold current as low as possible .

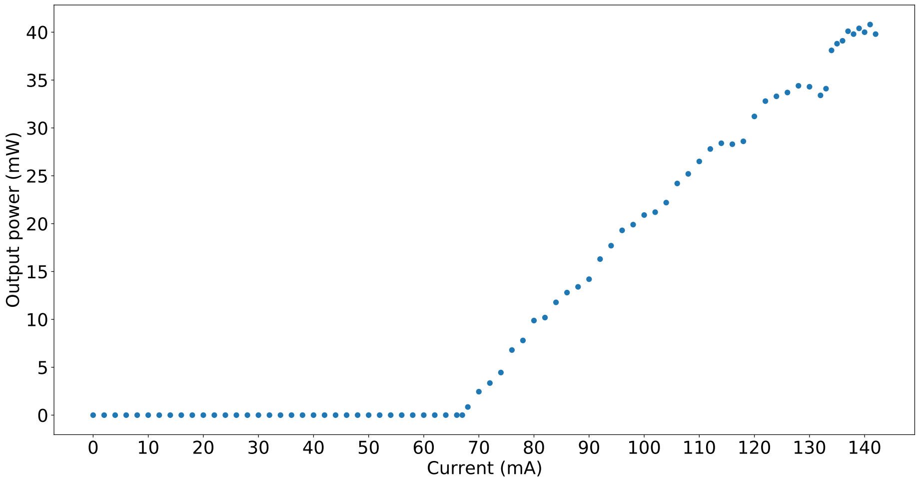

Figure 3.8 The laser has a threshold of 68 mA, with a maximum optical power of 42 mW at the recommended maximum operating current (140 mA).

In our case, the laser diode is pumped with electric current. The optimization procedure involves slightly lowering the current below threshold and tuning the pitch/yaw of the output coupler and the position of the first lens while observing if there is a clear “jump” of the light intensity, which indicates whether the system is lasing or not. One can refer to Ref. [33] (Sec. 5.2.2) for a more detailed explanation of the procedure. Using this procedure, we achieve an optimized threshold current of 68 mA, with a maximum optical power of 42 mW at the recommended maximum operating current of 140 mA.

3.2.2 Beam Shaping

For our experiment, a usable laser light needs to have a uniform beam shape of the fundamental Gaussian mode over its propagation distance. As mentioned before, the optics inside the ECDL laser housing can only fully collimate one direction of the beam: we can see from Fig. 3.9 (a), the laser beam along the vertical direction remains a relatively uniform beam profile over its propagation distance, whereas the beam along the horizontal direction is dispersing and distance-dependent, which needs to be further addressed by external beam shapers. In general, beam shapers are designed to redistribute the irradiance and phase of an optical beam to attain a desired beam profile that is maintained along the desired propagation distance [30].

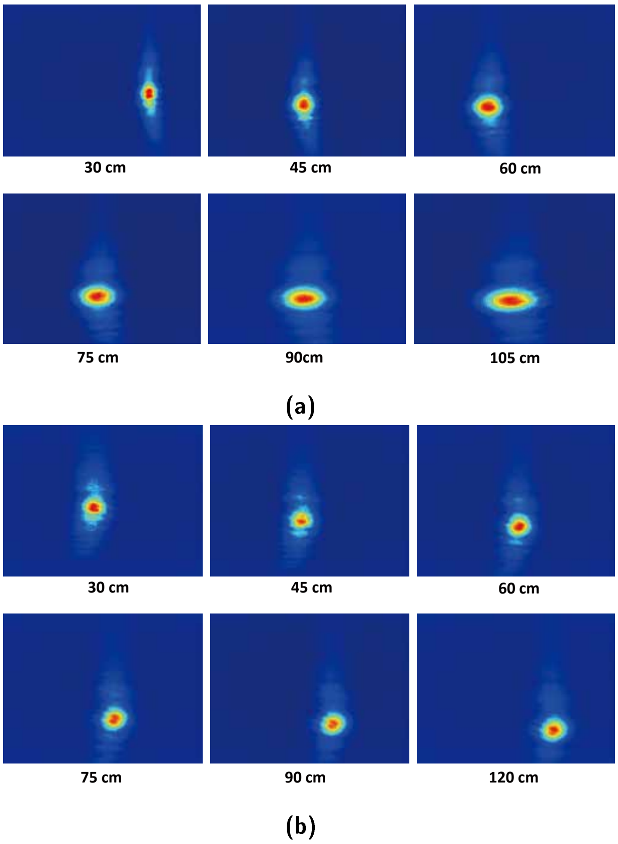

Figure 3.9 Beam profiles with/without cylindrical telescope. (a) Beam profiles at various distances without the use of cylindrical telescope. The beam shapes are asymmetric and diverge along the horizontal direction which is not fully collimated by the optics inside the laser housing. (b) Beam profiles at different distances with the use of cylindrical telescope. The beam shapes after the telescope are uniform and distance-independent, matching that of the symmetric fundamental Gaussian mode. (All presented beam shapes were observed on a beam profiler: CINOGY - CinCam CMOS 1201 Nano)

The exact beam shaper we are employing is a cylindrical telescope. A cylindrical telescope is made of two cylindrical lenses with the flat side facing each other and separated by the sum of their focal lengths. Like standard spherical lenses, cylinder lenses use curved surfaces to converge or diverge light, but what makes them special is that they only have optical power in one dimension. This property of cylinder lenses makes them useful for circularizing elliptical beams. Note that this feature cannot be achieved using standard spherical lenses because light will focus or diverge uniformly in a rotationally symmetric manner. As we can see from Fig. 3.10, a flat elliptical beam from the right is incident on the cylinder telescope. The telescope expands the vertical width of the original elliptical beam while leaving the horizontal direction untouched, resulting in a desired symmetric circular beam at the end.

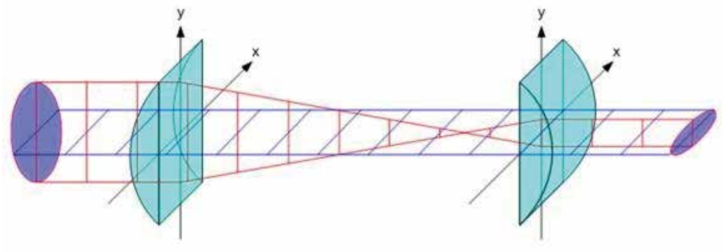

Figure 3.10 Beam correction from a set up cylindrical telescope made from two cylinder lenses. The vertical direction of an asymmetric (flat) beam incident from the right is corrected by a set of cylindrical telescopes, while the horizontal direction is left unchanged. The beam after correction thus has a uniform circular shape. Adapted from Ref. [34]

.

Note that in order to achieve a symmetrical output beam, the ratio of both lenses' focal lengths should match the ratio of the x and y beam divergences of the laser diode. In our case, the beam right after the optical isolator, which is the position we want to put the cylinder telescope, has a x-width of 1.017 mm and y-width of 2.310 mm from second moments fit, leading to a ratio of 1:2.3. The closest cylinder lenses that match this ratio are $f_1' = 20.01$ mm (Thorlabs-LJ1960L2-B) and $f_2' = 50.00$ mm (Thorlabs-LJ1821L1-B) with a focal length ratio 1:2.5. The corrected beam profiles are presented in Fig. 3.9 (b), where we can see a uniform beam shape at all distances up to 1.2 meter, which is enough for setting up the optics in our experiment.

It is worth mentioning that the divergence of laser diodes has a direct effect on the allowable length of the required sizes of the lenses. As the relative positions of the two lenses are fairly fixed due to their focal length, it is possible to calculate the maximum beam width (d) at each lens using the focal length of the specific lens (f) and the diode divergence angle (θ) along the axis of interest [30]. The clear aperture of each lens must be larger than the corresponding maximum beam width.

$$d = 2f \times tan\left(\frac{\theta}{2}\right) \tag{3.1}$$

Using Eqn. (3.1), the largest allowable beam width for the (smaller) lens with $f_1' = 20.01$ mm and a diode divergence angle of 10 ° is 3.5 mm. Given that both widths of the beam at the desired position are within this range, we are safe to use the chosen pair of cylindrical lenses without having to worry about beam aberrations due to oversized beam spots on the lenses.

Finally, the beam profile at the position for fiber coupling (75 cm away from the front of the laser housing) is presented in Fig. 3.11. Since the beam has a outer hallow (shallow blue) that influences the second moment fit, the results from this fitting method is no longer representative. We thus use the super-Gauss fit to gain knowledge of the central beam spot where the most of the energy is concentrated. The fit reveals a major width of 0.93 mm and a minor width of 0.84 mm, with an ellipticity (ratio of major to minor axis) of 0.90.

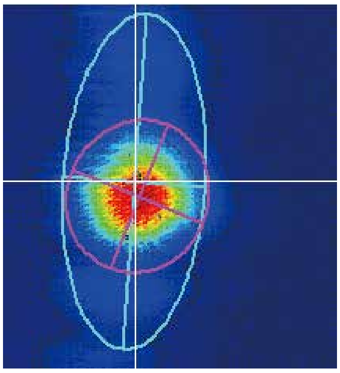

Figure 3.11 Laser beam profile at the point of fiber coupling. The shape of our laser beam is measured by a CINOGY CinCam CMOS 1201 Nano beam profiler at 75 cm away from the front face of the laser housing. The super-Gauss fit shows an ellipticity of 0.90 with major width 0.93 mm and minor width 0.84 mm.

3.2.3 Single Mode Operation

The preparation of a single layer of Sr atoms in an optical lattice requires the laser to be operated with single mode in both the transverse and longitudinal directions. The transverse single mode (TEM_{00}) operation is guaranteed by the limited pump spot size inside the diode implemented by the manufacturer [18]. However, the longitudinal mode, determined by both the diode gain line and the external cavity, needs to be carefully tuned. In reality, both the gain line and the cavity length (responsible for cavity longitudinal modes) are subject to change. Major factors that influence the gain medium are temperature and forward current, and the cavity length is controlled by the piezo ring. With all those factors influencing the longitudinal mode, we cannot naively assume that the laser is operating in single mode. It is thus important to verify the moding behavior of the laser before conducting actual experiments.

The first check for single mode testing is a measurement of the laser output spectrum by an optical spectrum analyzer (OSA). Since the OSA has a limited resolution, it only serves as a sanity check. For a well-behaved single-mode laser of which the linewidth is well below the OSA resolution, we should only see a single peak on the OSA spectrum, as shown in Fig. 3.12.

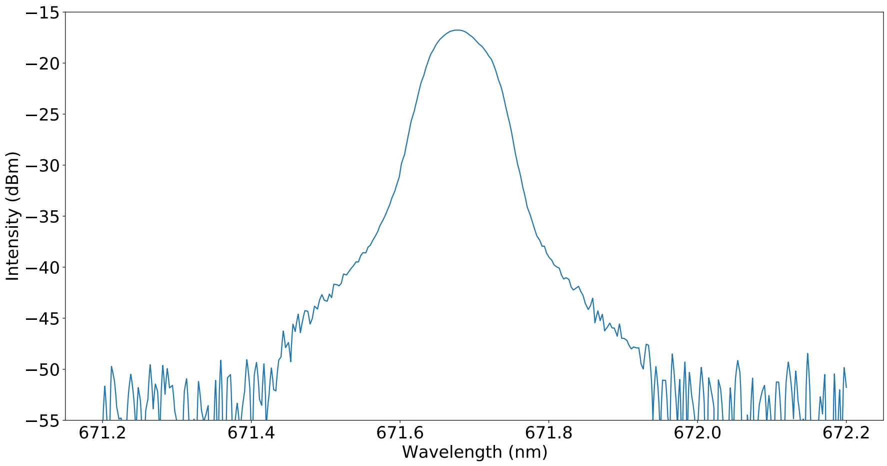

Figure 3.12 Laser output spectrum measured by an optical spectrum analyzer (OSA). Limited by the resolution, the OSA only serves as a sanity check from which we can only gain a rough knowledge of the laser mode behavior. From this measurement, we do not observe signs of serious multi-moding.

Although a well-resolved spectrum of the optical frequency from the laser is unpractical, we can easily resolve the interference of two optical signals that are very close in their frequencies. This premise is well held for the case of the possible longitudinal modes of the laser, which only differ by a few free spectral ranges of the cavity (1.5 GHz). If the laser is indeed multimoding, we can observe a peak in frequency space on the order of GHz. This measurement can be carried out by directing the light into a fast photodiode attached to a spectrum analyzer. An alternative way is to send a small amount of laser light into the high-finesse wavemeter (WS7) which has a built-in interferometry functionality. If we observe a single set of uniformly spaced peaks, we know that the laser is in single mode, whereas if there are more than one set of peaks mixed with each other, it means the laser is multimoding.

Note that it is not “the end of the world” if we observe signs of multi-moding. In fact, when we first tried the aforementioned methods, we observed mixed peaks from the wavemeter, as shown in Fig. 3.13 (a), and multiple peaks from the fast photodiode. These signs only mean that we should take actions to suppress, if not entirely eliminate, the unwanted modes. We note from our daily operations that the moding behavior for the laser is very sensitive to the temperature of the diode, the driving current, the tilt-angle of the output coupler, and the piezo ring. By gradually tweaking these parameters, we mange to find our laser lasing at a single mode as shown in Fig. 3.13 (b), with a forward current of 120 mA and a diode temperature of 20.9 °C.

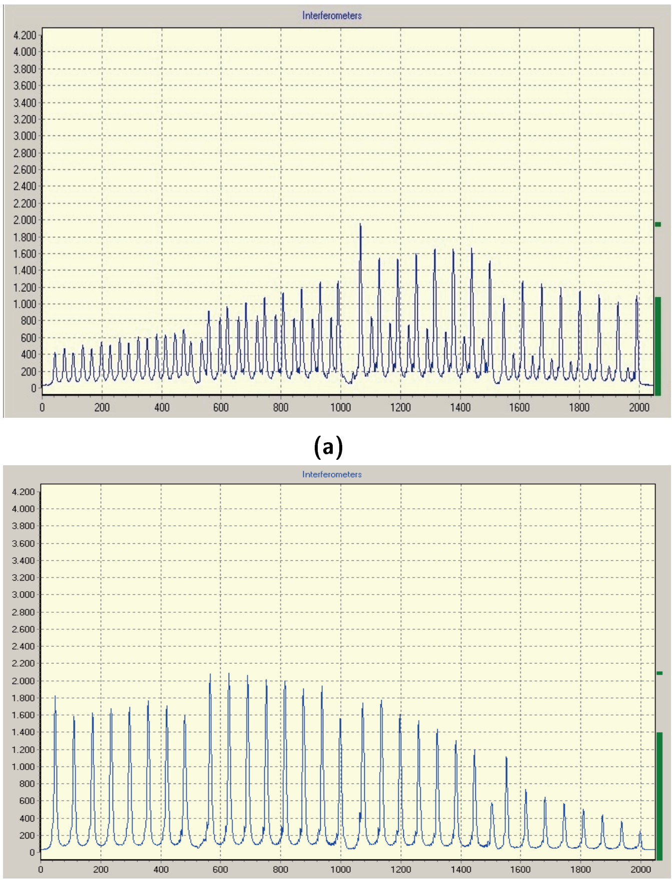

(a)

(b)

Figure 3.13 Wavemeter interferometry for mode testing. (a) The two sets of peaks mixed in the interferometry spectrum indicate multi-moding. (b) After adjusting the diode temperature, forward current, etc., we observe uniformly-spaced peaks, which indicates that the laser is operating in single mode. The operation condition for the single-mode data is at a forward current of 121 mA and a temperature of 20.9 °C.

3.2.4 Fiber Coupling Efficiency

Fiber coupling is a crucial task for efficient transport of the laser light into the experimental site. We are interested in coupling the laser light into a single-mode optical fiber, which involves matching the mode of the incident laser light into the mode of the fiber. The actual fiber coupling process involves beam-walking. One may find a good tutorial video for this daily routine in [35], or obtain the wisdom from a senior PHD student in your group.

It is worth mentioning that we should pay attention to the choice of the focusing lens, which plays an important role in determining the fiber coupling efficiency, calculated as the ratio of the optical power input into the fiber over the output power after the fiber. The coupling efficiency depends upon the overlap integral of the (Gaussian) mode of the input laser beam and the nearly Gaussian fundamental mode of the fiber. To couple light from a collimated laser beam of width (W) into a fiber with numerical aperture (NA), we should choose a lens with a focal length:

$$f = \frac{W}{NA}. \tag{3.2}$$

In our case, the beam width at the point of fiber coupling is approximately 0.9 mm (see Fig. 3.11), and the numerical aperture (NA) of the fiber (PM-630-HP) is 0.12. The optimal focal length is thus $f_{\mathrm{th}} = 7.5$ mm. We test three focusing lenses closest to this theoretical value in the lab with the corresponding coupling efficiencies summarized in Table 3.1. We find that the lens with the highest coupling efficiency (61.8%) is indeed the one with a focal lens $(f = 8$ mm) closest to the calculated optimal value $(f_{th} = 7.5$ mm).

Focal Length (mm)	Input Power (mW)	Output power (mW)	Fiber coupling efficiency
6.24	31.8	19.0	59.7%
8	33.5	20.7	61.8%
11	32.6	17.7	54.3%

Table 3.1 Table of fiber coupling efficiencies with various focusing lenses.

3.3 Optical Power Amplification via Stable Injection-locking

As previously mentioned, due to technical difficulties in engineering high-quality diodes at 671 nm, the power of single-mode diodes at this wavelength is much lower compared to other red diodes. Even though the current single-mode slicing diode is of the highest power in the market, we still find ourselves in a power-constrained situation. A low-power laser light will increase the minimum exposure time when interacting with the atoms, making the system more vulnerable to decoherence. From Table 3.1 we see that the power directly output from the fiber is on the order of 20 mW, which is barely enough for our experiment. Moreover, not all of this power will end up with the atoms: it is expected that the other optical components on the optical path (especially the AOMs) would consume a great portion of the light, leaving a even lower power for the actual experiment. In the following, we will present a method for power amplification of the single-mode 671 nm diode via the technique of stable injection-lock. By locking a powerful slave diode (with lower mode quality) to our high-quality seed diode, we manage to boost the power available for the experiment by a factor of 3, while sustaining the good mode quality of the seed light.

3.3.1 General Setup of the Injection-lock

In general, the broadband gain medium of a free-running laser diode (without coupling to an external cavity) allows the emission of photons across a broader spectrum around its nominal wavelength. If we forcibly inject a seed light with narrow-wavelength into the slave laser diode, it may start emitting light with the same optical properties as the seed light. This effect occurs if the injected light is much stronger than the spontaneously emitted photons of the free-running slave diode. In this situation, the mode of the seed light will be more likely to get exponentially amplified in the gain medium and it will suppress the other spontaneous modes of the slave diode medium by drawing all of the available power. Note that if we want this effect to happen across the whole gain medium, the injected light has to be well mode-matched to the internal cavity of the slave laser diode. The alignment thus becomes very sensitive, especially if we want to use a minimal amount of seed light.

The schematic of the optical setup for injection-locking is presented in Fig. 3.14. The current design is very close to that of a previous version [36] with only minor changes, i.e., the second polarizer of the Faraday isolator is replaced by an external polarizing beam splitter (PBS), and the main output light, instead of being fiber coupled inside the module, is directed directly outside. As we can see from Fig. 3.14, seed light coupled by an optical fiber is sent into the injection-lock and collimated using a lens. We use a half-wave plate to rotate the polarization of the seed light until it is accepted by the PBS in front of the Faraday isolator. The seed light is coupled, through the Faraday isolator, into the slave laser diode using the two mirrors. A half-wave plate directly in front of the slave diode is used to set the correct polarization. The slave laser now emits light that can pass through the Faraday isolator which rejects any counter propagating light (except for the seed light) to protect the diode. A half-wave plate and a PBS after the first PBS are used to split off a fraction of the power for monitoring the operation of the slave laser. The rest of the light is sent outside of the injection-lock module for further uses in the experiment.

3.3.2 Optical Properties of the Slave Diode

Ideally, we have the highest probability for a successful injection-lock to occur when the central wavelength of the salve diode exactly overlaps with that of the seed diode. In practice, however, it is also likely for injection-locking to take place as long as the seed wavelength is buried under the broad emission line of the free-running slave diode. Moreover, even if initially there is no overlapping at all between the emission lines of the two diodes, by tuning the temperature of the slave diode, we can move its central wavelength

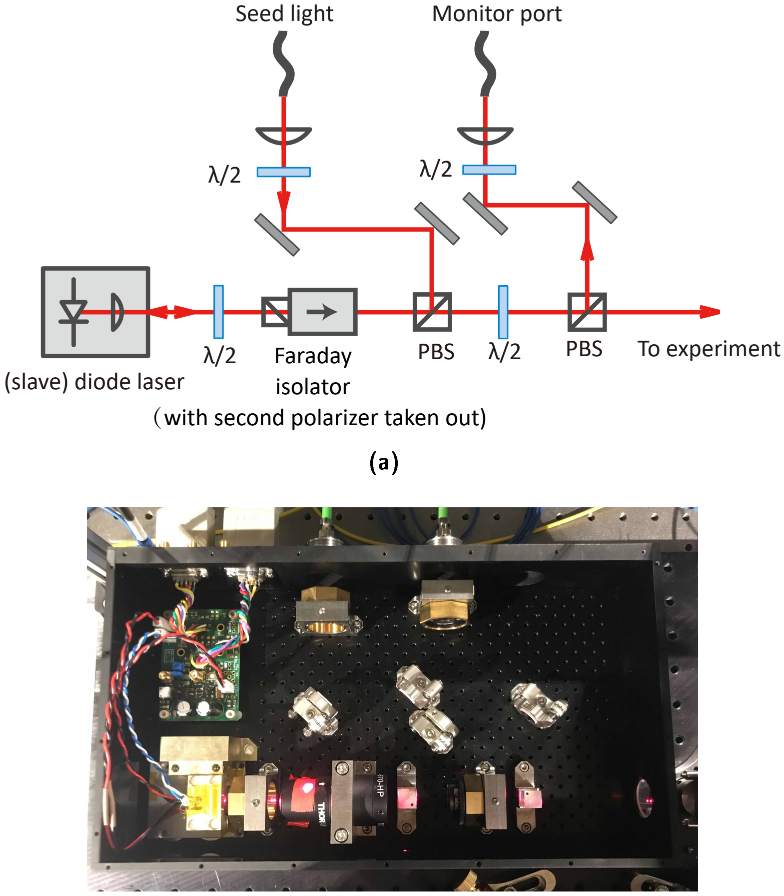

(a)

(b)

Figure 3.14 Setup of the slicing diode injection-lock module. (a) Schematic of the optical setup. (b) A picture of the actual experimental setup. A seed light from the left fiber port is sent into the module. The seed light is directed by two mirrors, reflected by the PBS in front of the Faraday isolator (of which the second polarizer is replaced by the PBS) and sent into the slave diode inside the diode case. The slave diode will then be forced to output a mode matching that of the seed light. A fraction of the slave light is directed into the right fiber port for monitoring purposes, with the rest of the light sent outside the box.

closer to that of the seed light, making the injection-lock more likely to succeed. Therefore, the goal for the selection of a slave diode is to find a powerful diode of which the free-running emission line, after some reasonable heating or cooling within its allowed operational temperature range, covers the wavelength of the seed light.

We first look into high-power diodes from Thorlabs with wavelength closest to 671 nm. The diodes we test include (1) HL6544FM with central wavelength 660 nm and output power 50 mW; (2) L660P120 (660 nm, 120 mW); and (3) HL6750MG (685 nm, 50 mW). However, the difference between the central wavelength of these diodes and that of the seed light is so large that we need to heat up diode 1 and 2 by more than 50 °C or cool diode 3 to below 10 °C to get a slight overlap of their emission lines with that of the seed diode. Although the adjusted temperatures are within the specified maximum/minimum temperature, under the circumstances of extreme operation, the lasing threshold as well as the final optical power seriously degrade to even below that of the seed light, and thus the aforementioned diodes are no longer meaningful as slave diodes.

We finally land at a diode that was by the time a preliminary product of the Ushio company and had not been officially released into the public market. It is an AlGaInP laser diode (HL67xx1DG) with a central lasing wavelength of 675 nm, covering a minimum lasing wavelength of 670 nm and a maximum wavelength of 680 nm. It is a high-power diode with a specified maximum power of 210 mW at the maximum operational current of 265 mA. As shown in Fig. 3.15 (a), the free-running emission line covers very well the intended seed light wavelength at 671.2 nm after cooling down to 18 °C (which is 5 °C below room temperature).

3.3.3 Solving the Problem of Insufficient Cooling Capacity

A major technical difficulty we run into when setting up the injection-lock is related to the temperature cooling range of the system. Note that in order to reach the point where there exits enough overlapping of the salve diode and the seed light emission lines, we need to cool the slave diode down to 18 °C. However, as can be seen from the blue curve in Fig. 3.16, the diode case cannot stay cooled due to a limited cooling capacity. As shown in Fig. 3.17, the diode case is designed to be entirely suspended by a left wall having a limited contact area with the injection-lock breadboard (the heat sink). This design is advantageous for the case of heating in which a built-up of heat is desired. However, when it comes to cooling, the heat generated from the Peltier element embedded beneath the slave diode cannot be transferred into the heat sink in time, which would eventually raise the temperature of the diode.

The solution is to increase the heat transfer rate by inserting an additional aluminum plate underneath the diode case, which greatly shortens the thermal path and increases the contact area with the heat sink. Note that we have to fully cover the aluminum plate with Kapton insulating tape to prevent electric conduction between the diode case and the rest of the injection-lock module. An Ohmmeter is used to confirm that there is no electric conduction between these two elements. Finally, as we can see from the orange curve in Fig. 3.16, the diode can stay cooled to a temperature as low as 13.5 °C stably.

3.3.4 Testing of the Slave Diode

Once we have demonstrated sufficient cooling ability for the diode, we proceed to test injection locking at the required low temperature. After we send a seed light of 1.6 mW

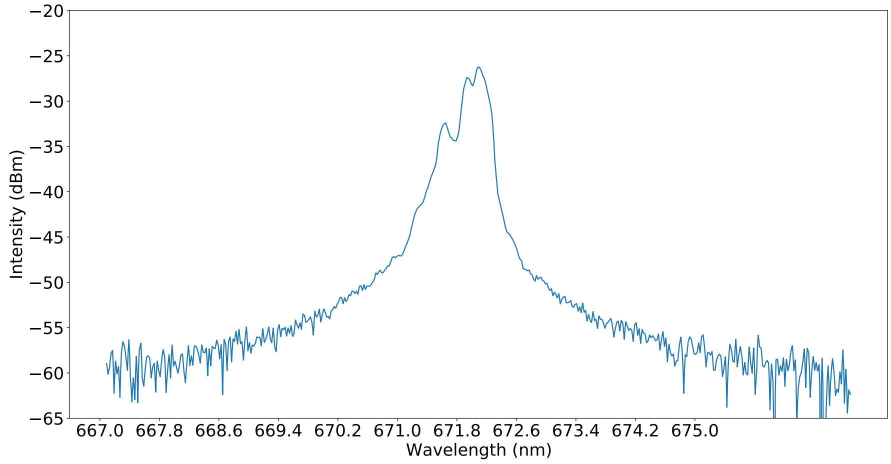

(a)

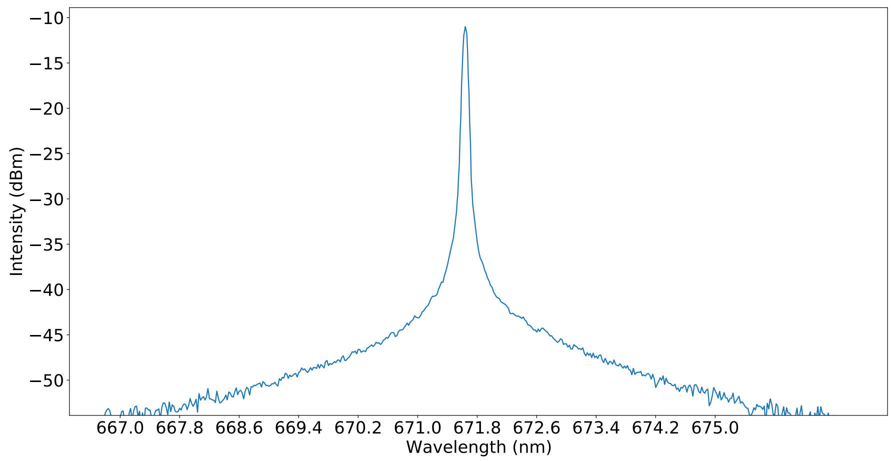

(b)

Figure 3.15 OSA spectrum of the Ushio (slave) diode without/with the seed light at 18 °C. (a) The free-running emission line of the slave diode covers the central wavelength of the seed light, making it promising for injection-locking applications. (b) The spectrum becomes much narrower than the free-running spectrum with a central wavelength shifted to that of the seed light after sending in the seed light.

into the slave diode, we observe from the OSA that the slave diode emission line suddenly narrows down and mimics that of the seed light as shown in Fig. 3.15 (b), which is the sign for a successful injection-locking system.

To continuously monitor the locking status, we couple light from the salve diode into a

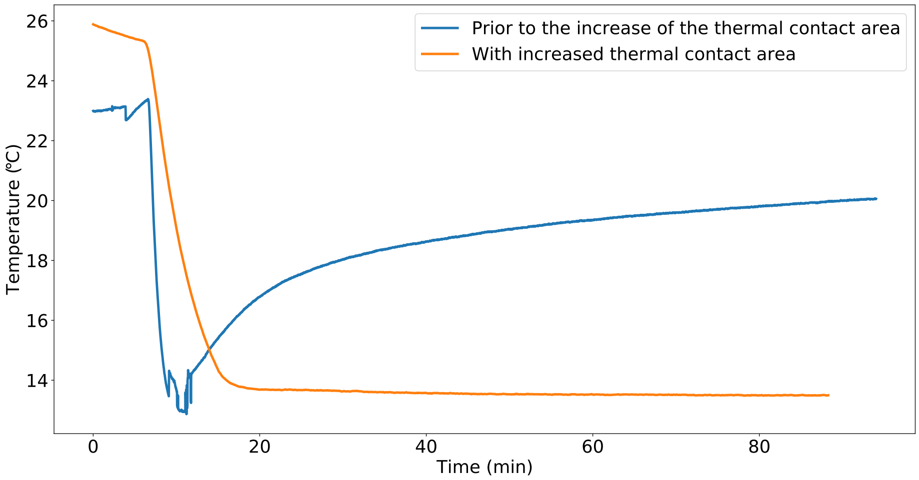

Figure 3.16 Cooling power before and after increasing the thermal contact area.

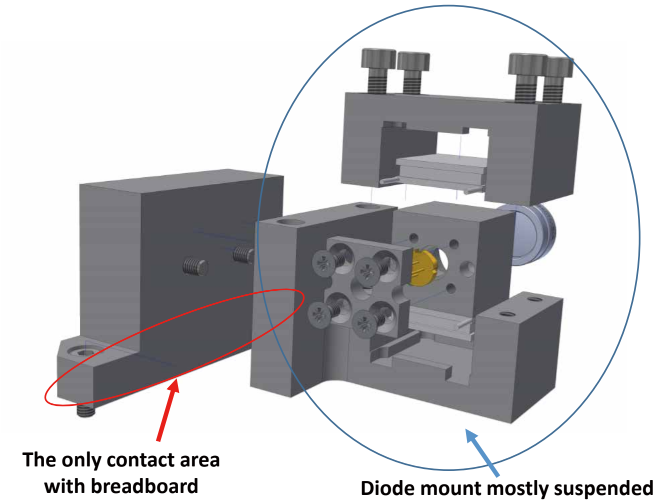

Figure 3.17 Any excess heat of the suspended diode case can only flow through the left wall into the breadboard. The small contact area between the wall and the breadboard seriously limits the cooling power. Schematic adapted from Ref. [36].

scanning Fabry–Pérot cavity of which the optical length can be driven (via its piezo) by an oscillating voltage signal from a signal generator. The scanning cavity is supposed to only transmit light that matches the longitudinal mode at the moment. Therefore, for a slave diode truly injection-locked to the single-mode seed diode, the transmission spectrum (measured by a photodiode) will only show a narrow single peak where most of the power is concentrated for each scanning period. The locking case is shown in

Fig. 3.18 (b). On the other hand, if the slave diode is not locked with the seed light, its broadband emission line will manifest itself as a collection of peaks on the transmission spectrum, which is shown in Fig. 3.18 (a).

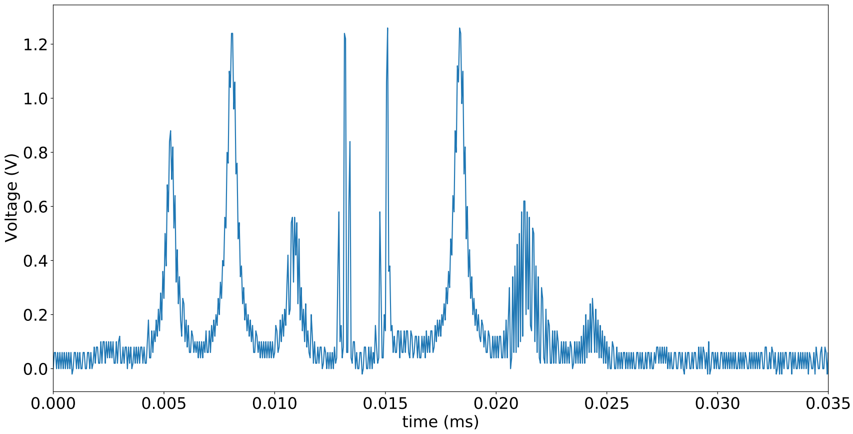

(a)

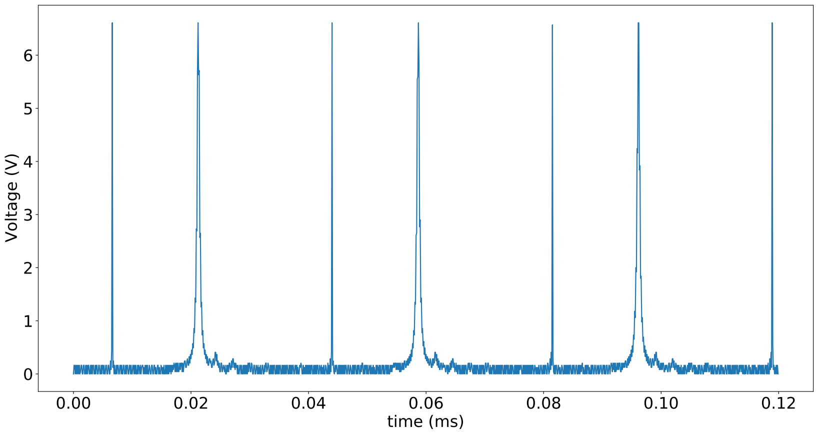

(b)

Figure 3.18 Transmission from a scanning Fabry–Pérot cavity for monitoring of the injection-lock. (a) The unlocked case. (b) The locking case.

Note that the system only locks at specific currents with a certain periodicity, which are specified in Table 3.2. Due to the asymmetry in the thermal properties of the solid state diode, the locking is significantly better when "turning down" the slave diode forward current as opposed to "turning up" the current. Therefore, it is always recommended to go a few mA above the target current and gradually turn it down to form a stable injection-locked state.

Forward current (mA):
105.65
117.74
129.36
140.43
151.02
161.03
170.56
179.94
189.00
197.53

Table 3.2 Currents that lock the slave diode.

3.3.5 Characteristics of the Injection-locked Laser Light

Finally, we will discuss the characteristics of the injection-locked light. The slave diode has a threshold current at 68 mA and its output power (after 85 % Isolator) at 18 °C with a driving current above 90 mA is presented in Fig. 3.19. Note that due to the limit of our current controller, we can only reach a maximum forward current of 200 mA.

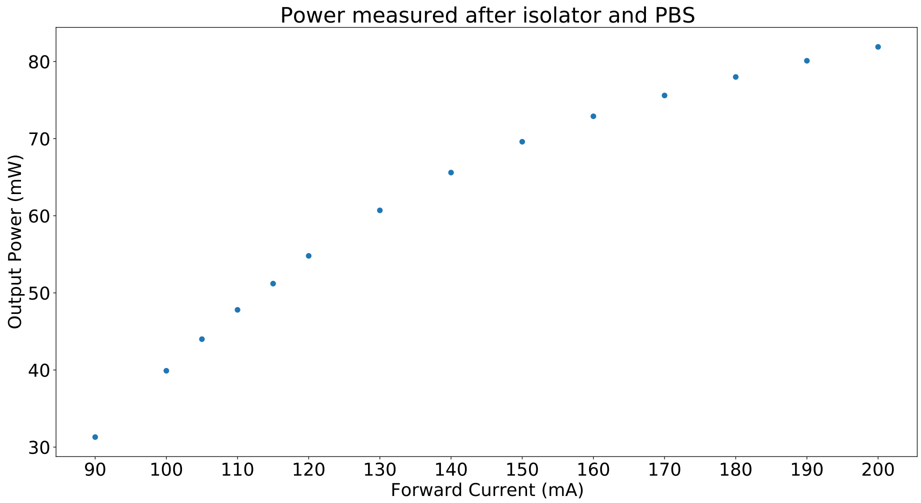

Figure 3.19 Lasing power vs. forward current for the injection-lock.

For beam shaping, we apply a set of plano convex lenses with focal lengths 40 mm (first lens) and 25.3 mm (second lens) for beam shaping. Lastly, we couple the laser light from the injection-lock into a PM-630 optical fiber with a coupling efficiency of 79.2 %, corresponding to a coupled power of 64.1 mW which is three times larger than that of the seed diode. At this point, we are confident in our ability to supply enough optical power to the atoms for the preparation of a single layer of Sr atoms in our optical lattice.

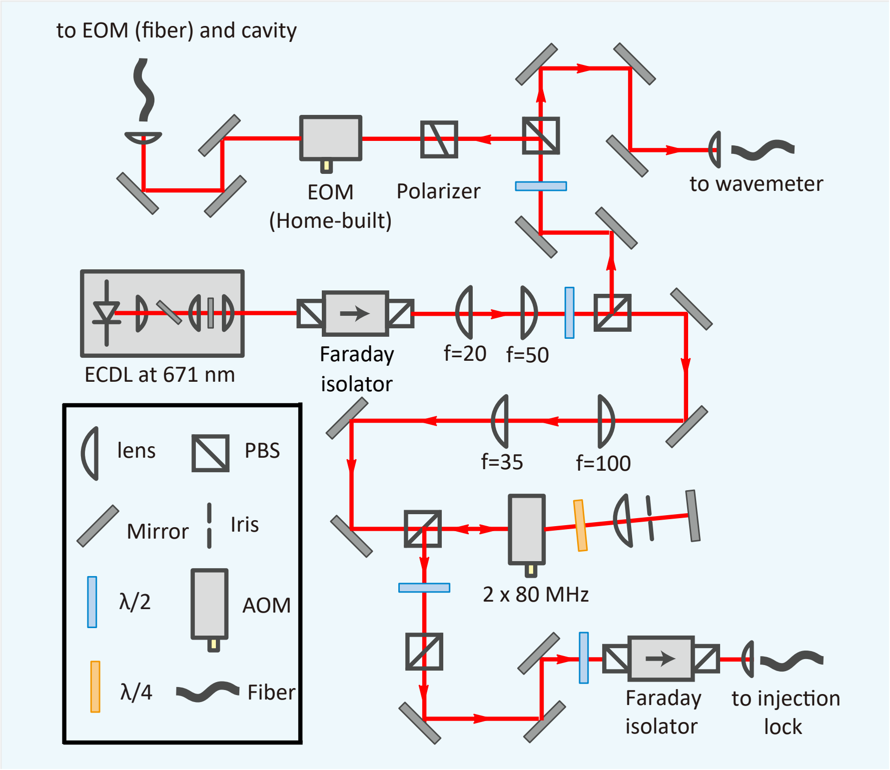

Figure 3.20 Optical setup for the $^3P_2$ laser. Laser light generated from the linear ECDL is split by a series of half waveplates and PBSs into three arms for injection locking, PDH locking, and wavelength monitoring.

A schematic of the optical setup for the $^1S_0$-$^3P_2$ laser is presented in Fig. 3.20. From the schematic we see that laser light generated from the linear ECDL is first sent through a Faraday isolator preventing black reflections, and is then collimated by a set of cylinder telescopes. The light is then split into three arms by a series of PBS and half waveplates. The beam from the first arm (bottom part) is resized by a set of plano-convex lenses to match the optimal beam size for the AOM, and then input into a double-pass AOM for frequency tuning, after which is incident into the injection lock via an optical fiber as seed light. Note that an extra isolator is placed at the end of this arm to prevent back reflections from the injection lock disturbing the master laser. The second arm (top right) is directed into the wavemeter for wavelength monitoring. The third arm (top left) enters a polarizer to match the polarization of the electro-optic modulator (EOM) crystal, and then phase modulated by the EOM before entering the reference cavity for frequency stabilization via PDH locking, which will be fully explained in the next Section.

Chapter 4

Frequency Stabilization of the $^1\mathrm{S}_0$-$^3\mathrm{P}_2$ Laser

THE linear ECDL is, to a large extent, still vulnerable to environmental disturbances and produces a linewidth that exceeds the requirement for the preparation of a single layer of Sr atoms. To this end, a frequency-locking scheme is employed to further stabilize the laser to an ultrastable reference cavity. The general locking scheme will be fully discussed in this Chapter, and the optical reference cavity will be introduced in the next Chapter.

4.1 The Pound-Drever-Hall Locking Scheme

An essential concept for the laser frequency stabilization to a reference cavity is the Pound-Drever-Hall (PDH) locking scheme. The general idea is to first phase-modulate a laser beam before sending it into a cavity to generate sidebands around the carrier frequency. The carrier, if close enough to the cavity resonant frequency, will be transmitted through the cavity while the sidebands are reflected back. We will use the intensity of the reflected beam to obtain an error signal containing information not only on how close the laser is with respect to the cavity frequency, but also on which direction we should move the laser frequency towards for a even closer frequency to resonance. In the following, we will first discuss the fundamental mathematics for a in-depth understanding of this rather complicated concept, and then we will present the experimental realization of such a locking scheme for our laser system.

4.1.1 Derivation of the Error Signal

In the following we will derive the error signal essential for locking the laser to the cavity. This derivation follows closely to Ref. [37]. We start with a laser beam with electric field:

$$E_{\text{in}} = E_0 e^{i\omega t}. \tag{4.1}$$

To generate sidebands, we need to phase-modulate this beam. The tool we employ is an electro-optic modulator (EOM), the details of which will be explained later in this chapter. The phase-modulated light can be expressed as:

$$E_{\text{mod}}(\omega) = E_0 e^{i(\omega t + \beta \sin(\Omega t))}, \tag{4.2}$$

where Ω is the modulation frequency determined by the RF signal sent into the EOM, and β is the modulation depth proportional to the voltage amplitude of the RF signal. Using the Jacobi-Anger expansion:

$$e^{iz\sin(\theta)} = \sum_{n=-\infty}^{\infty} J_n(z) e^{in\theta}, \tag{4.3}$$

where $J_n(z)$ is the n-th Bessel function of the first kind, and applying the relation:

$$J_{-n}(z) = (-1)^n J_n(z), \tag{4.4}$$

we can expand Eqn. 4.2 to the first order:

$$E_{\text{mod}} \approx E_0[J_0(\beta)e^{i\omega t} + J_1(\beta)e^{i(\omega+\Omega)t} - J_1(\beta)e^{i(\omega-\Omega)t}]. \tag{4.5}$$

At this point, the phase-modulation basically splits the original beam into three beams: a carrier with (angular) frequency ω, and two sidebands with frequencies $\omega \pm \Omega$.

To describe the behavior of the reflected beam, we introduce the concept of reflection coefficient $F(\omega)$, which is the ratio of the reflected beam to the incident beam. For a symmetric cavity with no losses, $F(\omega)$ is given by [37]:

$$F(\omega) = \frac{E_{\text{ref}}}{E_{\text{in}}} = \frac{r(e^{i\omega/\nu_{\text{FSR}}} - 1)}{1 - r^2 e^{i\omega/\nu_{\text{FSR}}}}, \tag{4.6}$$

where r is the amplitude reflection coefficient of each mirror, and $\Delta\nu_{\text{FSR}}$ is the cavity free spectral range. We multiply the field of the incident beams with the corresponding reflection coefficients to obtain the field of the reflected beam:

$$E_{\text{ref}} \approx E_0[F(\omega)J_0(\beta)e^{i\omega t} + F(\omega+\Omega)J_1(\beta)e^{i(\omega+\Omega)t} - F(\omega-\Omega)J_1(\beta)e^{i(\omega-\Omega)t}]. \tag{4.7}$$

Since it is the power of the reflected beam (denoted as P_{ref}) that is actually being measured by the photodetector, we will take the square of the field:

$$\begin{aligned} P_{\text{ref}} &= |E_{\text{ref}}|^2 \\ &= P_{DC} + 2|E_0|^2 J_0(\beta) J_1(\beta) \{\text{Re}[F(\omega)F^*(\omega+\Omega) - F^*(\omega)F(\omega-\Omega)]\cos(\omega t) \\ &+ \text{Im}[F(\omega)F^*(\omega+\Omega) - F^*(\omega)F(\omega-\Omega)]\sin(\Omega t)\} + (2\Omega \text{ terms}), \end{aligned} \tag{4.8}$$

where P_{DC} denotes the non-oscillating terms. Note that the Ω terms comes from the interference between the carrier and the sidebands, and the 2Ω terms are due to the sidebands interfering with each other. At high modulation frequency $\Omega >> \Delta\nu_c$, we can perform the approximation [37]:

$$F(\omega)F^*(\omega+\Omega) - F^*(\omega)F(\omega-\Omega) \approx -2i \cdot \text{Im}(F(\omega)), \tag{4.9}$$

which is purely imaginary, leading to the vanishing of the cosine term in Eqn. 4.8. Now, let us neglect the 2Ω terms and define the remaining AC terms in Eqn. 4.8 as the error signal:

$$\begin{aligned} \epsilon(\omega) &= 2|E_0|^2 J_0(\beta) J_1(\beta) \text{Im}[F(\omega)F^*(\omega+\Omega) - F^*(\omega)F(\omega-\Omega)]\sin(\Omega t) \\ &= -4|E_0|^2 J_0(\beta) J_1(\beta) \text{Im}[F(\omega)]\sin(\Omega t). \end{aligned} \tag{4.10}$$

The reflected beam received by the photodetector becomes:

$$P_{\text{ref}} \approx P_{\text{DC}} + \epsilon(\omega)\sin(\Omega t). \tag{4.11}$$

We will then use a mixer to mix this signal with an external AC signal $\sin(\Omega t + \phi)$ which has the same frequency Ω and a relative phase ϕ compared to the modulation signal. The output of a mixer is basically the multiplication of the two input signals. Using the trigonometry identity:

$$\sin(\alpha t)\sin(\alpha' t + \phi) = \frac{1}{2}\left\{\cos[(\alpha - \alpha')t - \phi] - \cos[(\alpha + \alpha')t + \phi]\right\}, \tag{4.12}$$

we obtain the signal after the mixer as:

$$\begin{aligned} P_{\text{mixed}} &= [P_{\text{DC}} + \epsilon(\omega)\sin(\Omega t)] \cdot \sin(\Omega t + \phi) \\ &= \frac{1}{2}\epsilon(\omega)\cos(\phi) + P_{\text{DC}}\sin(\Omega + \phi) - \frac{1}{2}\epsilon(\omega)\cos(2\Omega + \phi). \end{aligned} \tag{4.13}$$

Finally, we pass this signal through a low-pass filter with corner frequency below Ω to isolate the DC term in Eqn. 4.13. By carefully matching the phases of the two input signals of the mixer, we can have the $\cos(\phi)$ term equal to 1, and the remaining DC term thus becomes $\frac{1}{2}\epsilon(\omega)$. As we can see from a simulation in Fig. 4.1, the error signal behaves

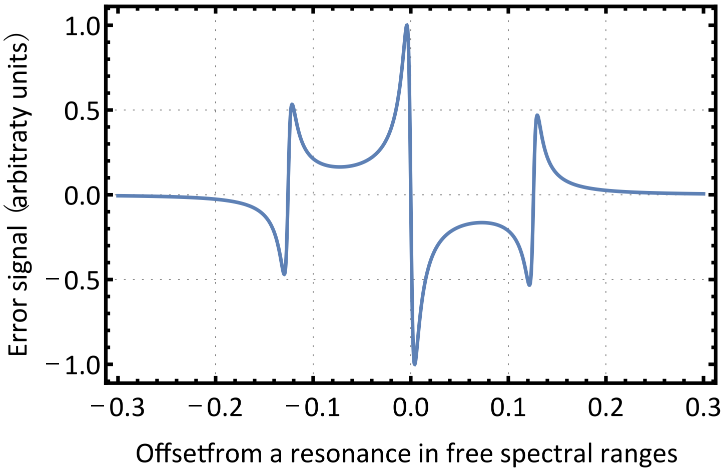

Figure 4.1 The error signal obtained for a high modulation frequency Ω. Here Ω is chosen to be $2\pi \cdot 30$ MHz while the linewidth was 2 MHz. Adapted from Ref. [36].

linearly when the laser frequency is close to the cavity resonance with a zero crossing at the on-resonant frequency. This signal is continuously fed into a servo amplifier (loop-filter) which modulates the laser diode forward current to perform fine adjustments to the laser frequency. Note that if the zero crossing of the error signal is steep enough, and if the feedback loop is fast enough, we can even reduce the linewidth of the laser within the linewidth of the cavity.

4.1.2 Phase Modulation with the Home-built EOM

As discussed in the previous Section, one of the most critical steps in obtaining the error signal for the PDH lock is to phase-modulate the laser beam for the generation of the sidebands. For this purpose, we construct an electro-optic modulator (EOM). An EOM relies on the electro-optic effect referring to the change in the refractive index of a material due to the presence of an electric field, which distorts the orientations and positions of the molecules constituting the material [38]. The change of refractive index affects the phase of the light traveling through the EOM, making the phase modulation for PDH locking possible.

The EOM Crystal

For our home-built EOM, we choose a lithium niobate ($LiNbO_3$) crystal with anti-reflection coating at 630 nm - 920 nm, as shown in Fig. 4.2 (b). Note that the polarization of the input beam needs to be aligned with one of the optical axes of the crystal via a polarizer, so that the polarization state is not changed.

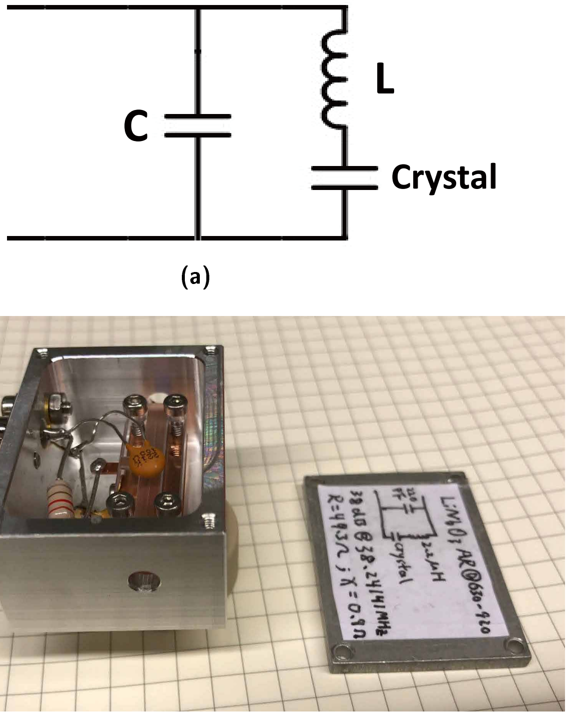

(b)

Figure 4.2 (a) An LC resonant circuit is used for impedance matching with the EOM crystal. (b) A photo of the assembled EOM module. The LC values are optimized at L = 2.2 μH and C = 220 pF with a minimized overall reactance of 0.9 Ω, leading to an optimal return loss at 35.6 dB and a resonant frequency at 38.24 MHz.

To ensure optimal power transfer to the lithium niobate crystal (the load), we integrate the crystal into a LC resonant circuit and perform impedance matching to maximize the field strength and hence generate strong modulations. The LC circuit diagram for the EOM is shown in Fig. 4.2 (a). We would like the reactance of the LC circuit to cancel that of the crystal, so that we can reduce the net reactance for lower power dissipation in the load. For impedance matching, we conduct a single-variable search during which the inductor is chosen to be fixed at L = 2.2 μH, while the capacitor is optimized based on the return loss (incident power / return power) using a graphical impedance analyzer. We test five capacitors with capacitance ranging from 100 pF to 330 pF. For each capacitor there exits a resonant frequency at which the return loss is at the (local) maximum. By going through the capacitor search, we find a global maximum return loss of 35.6 dB at C = 220 pF, with a resonant frequency at 38.24 MHz. The corresponding resistance of the circuit is 49.3 Ω with a low net reactance of 0.9 Ω. Note that we need to close the metal cap of the EOM box for each test, as the cap makes a big difference for the overall impedance of the system and affects the resonant frequency. Additionally, the crystal oscillator inside the impedance analyzer takes time to warm up, which means that we cannot trust the frequency readout before it stabilizes to a stable value.

The EOM Driver

An oscillating electric field of high stability is required to drive the EOM crystal for the phase modulation of the laser beam. For our EOM, the oscillating field is originated from the SiT3808 voltage controlled crystal oscillator (VCXO) mounted on the home-built EOM driver. The VCXO is a programmable oscillator with 6 digit accuracy for any frequency between 1 MHz to 80 MHz. The actual programming procedure involves using the Time Machine II programming module with the associated software.

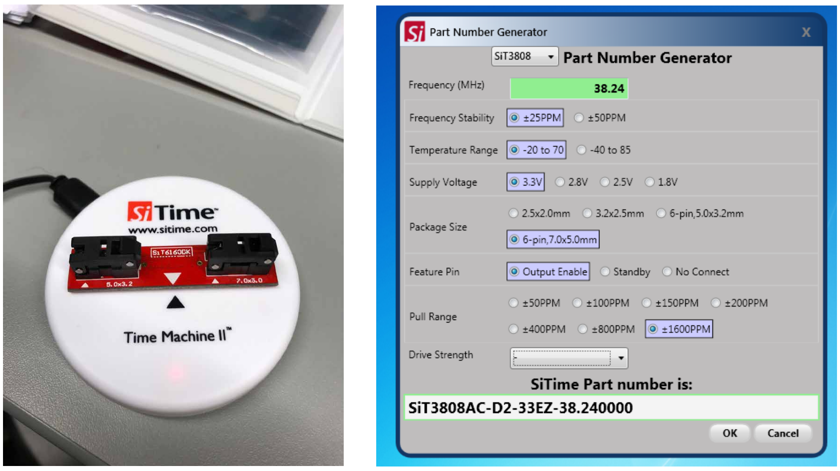

SiT3808 Part Number Generator

Frequency (MHz) 38.24

Frequency Stability ● ±25PPM ○ ±50PPM

Temperature Range ● -20 to 70 ○ -40 to 85

Supply Voltage ● 3.3V ○ 2.8V ○ 2.5V ○ 1.8V

Package Size ○ 2.5x2.0mm ○ 3.2x2.5mm ○ 6-pin,5.0x3.2mm ● 6-pin,7.0x5.0mm

Feature Pin ● Output Enable ○ Standby ○ No Connect

Pull Range ○ ±50PPM ○ ±100PPM ○ ±150PPM ○ ±200PPM ○ ±400PPM ○ ±800PPM ● ±1600PPM

Drive Strength -

SiTime Part number is:

SiT3808AC-D2-33EZ-38.240000

(a) **(b)**

Figure 4.3 Programming the VCXO. (a) The Time Machine II module for connecting the VCXO to the computer. (b) Programming parameters from the software programming page.

A photo of the programming module and the programmed parameters for our VCXO are presented in Fig. 4.3. The frequency is selected to be 38.24 MHz, which is the resonant frequency measured by the impedance analyzer. The configuration of the selected VCXO (5.0 mm x 3.2 mm, 6-pin) requires the Time Machine socket card SiT6160DK (red card in Fig. 4.3 (a)). We can follow exactly the user manual [39] for most of the programming procedures. However, one parameter we need to pay special attention to is the choice of the drive strength, which is directly related to the rise/fall time of the oscillating signal. On the one hand, we would like the rise/fall time T_{rf} (time required for the signal to reach 10% / 90% of the maximum amplitude) to be large and the signal to be smooth, since a very steep edge for the oscillating signal means more Fourier components with increased number of higher order harmonics. On the other hand, a high oscillating frequency requires a steep edge with small rise/fall time of the signal so that we can guarantee a "full swing" of the output voltage. An estimate of the maximum T_{rf} can be carried out assuming that for any legitimate oscillating signal, the 10% rise time or 90% fall time should not surpass the time when the signal amplitude is in between (the "flat" time). For a given frequency, the maximum rise/fall time $T_{\mathrm{rf,max}}$ happens when they equal the "flat" time:

$$T_{\mathrm{rf,max}} = \frac{1}{6 \cdot f}, \tag{4.14}$$

where f is the desired signal frequency. For our desired frequency (38.24 MHz), the maximum T_{rf} is calculated to be 4 ns. According to Table 4.1, the highest T_{rf} below 4 ns corresponds to the F (default) level, which is what we should select during the programming process.

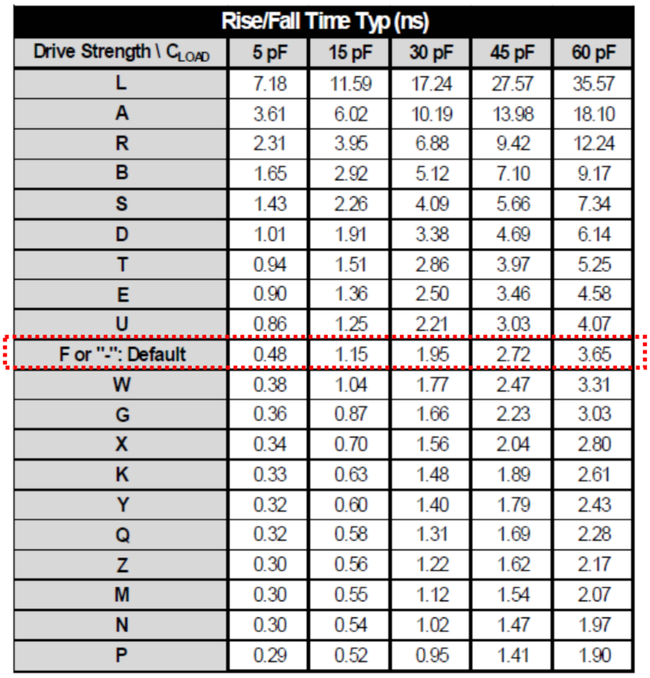

Rise/Fall Time Typ (ns)					
Drive Strength \ C_{LOAD}	5 pF	15 pF	30 pF	45 pF	60 pF
L	7.18	11.59	17.24	27.57	35.57
A	3.61	6.02	10.19	13.98	18.10
R	2.31	3.95	6.88	9.42	12.24
B	1.65	2.92	5.12	7.10	9.17
S	1.43	2.26	4.09	5.66	7.34
D	1.01	1.91	3.38	4.69	6.14
T	0.94	1.51	2.86	3.97	5.25
E	0.90	1.36	2.50	3.46	4.58
U	0.86	1.25	2.21	3.03	4.07
F or "-": Default	0.48	1.15	1.95	2.72	3.65
W	0.38	1.04	1.77	2.47	3.31
G	0.36	0.87	1.66	2.23	3.03
X	0.34	0.70	1.56	2.04	2.80
K	0.33	0.63	1.48	1.89	2.61
Y	0.32	0.60	1.40	1.79	2.43
Q	0.32	0.58	1.31	1.69	2.28
Z	0.30	0.56	1.22	1.62	2.17
M	0.30	0.55	1.12	1.54	2.07
N	0.30	0.54	1.02	1.47	1.97
P	0.29	0.52	0.95	1.41	1.90

Table 4.1 Rise/fall times for specific drive strengths.

After having programmed the VCXO with the right parameters, we can proceed to solder all the electric components onto the EOM driver PCB based on the schematic shown in Fig. 4.4 (c). It is worth noting that the actual value of the LC low-pass filter responsible for reducing the VCXO harmonics (circled region on the bottom left of Fig. 4.4 (c)) undergoes a similar optimization search as described for the LC circuit in the previous Section. The final value of the capacitor is determined to be 42 pF different from the specified 56 pF from the schematic. The performance of the low-pass filter is presented in Fig. 4.5. Note that the signal from the VCXO is split for the two output ports with different amplifications. As shown in Fig. 4.4 (a), the port for the mixer (which requires more power) has an output power of 7 dBm and the port for the EOM crystal has a power of -10 dBm. Pictures

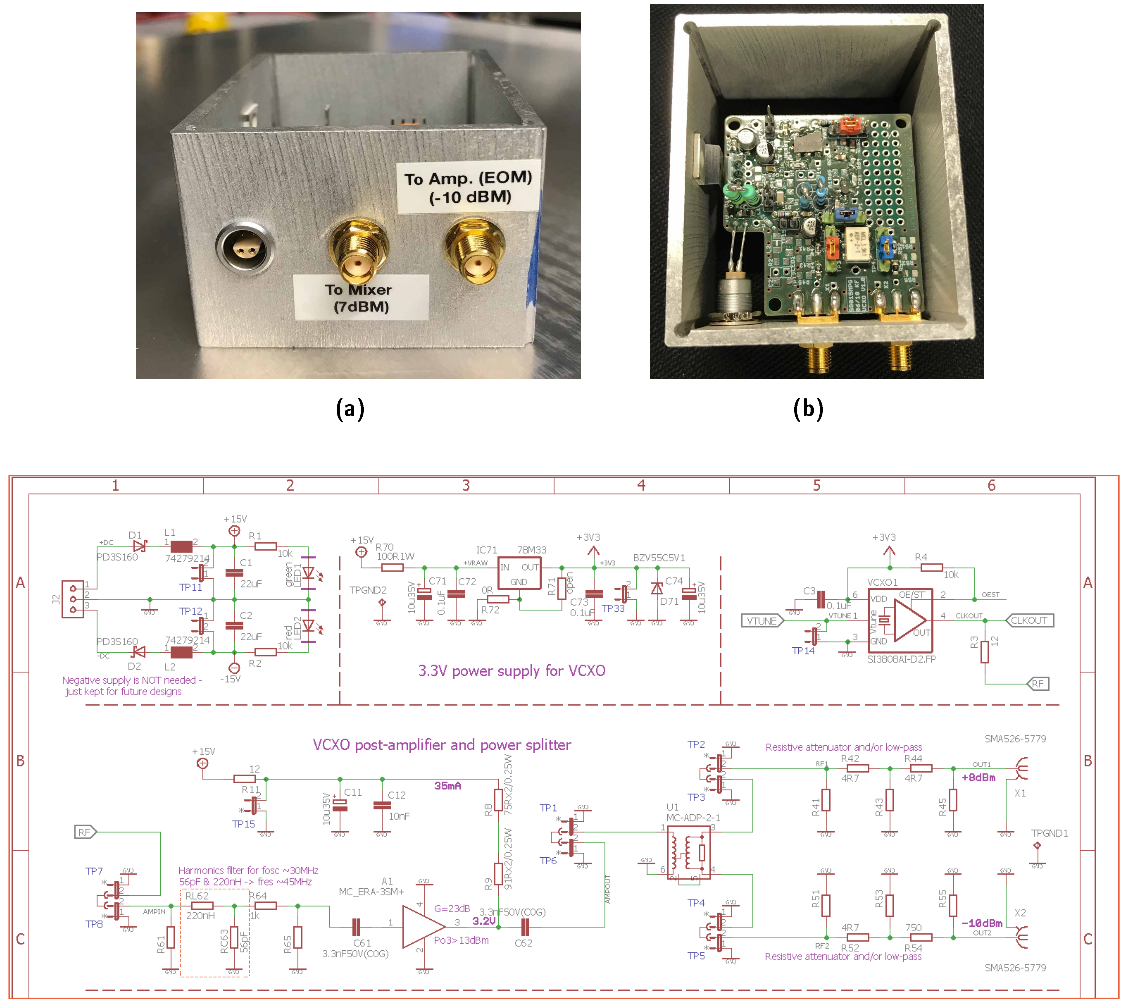

(a) (b)

(c)

Figure 4.4 The EOM driver module. (a) The front side of the EOM driver box. (b) The top side of the EOM driver box. (c) The electric circuit diagram of the EOM driver. Note that a change is made in the circled region at the bottom left, which is an LC low-pass filter designed to filter out the harmonics of the VCXO: different from the specified value, the capacitor RC63 is optimized to be 42 pF for better performance at 38.24 MHz (the resonant frequency).

of the front and top sides of the assembled driver module are presented in Fig. 4.4 (a) and Fig. 4.4 (b), respectively.

As a final check, we measure the linewidth of the EOM driver with a spectrum analyzer (Anritsu MS2721B). Running the spectrum analyzer at the highest resolution (1 Hz), we obtain a measured linewidth of 1.7 Hz for the EOM driver output, which is shown in Fig. 4.6). This result is benchmarked with a high-quality function generator (keysight

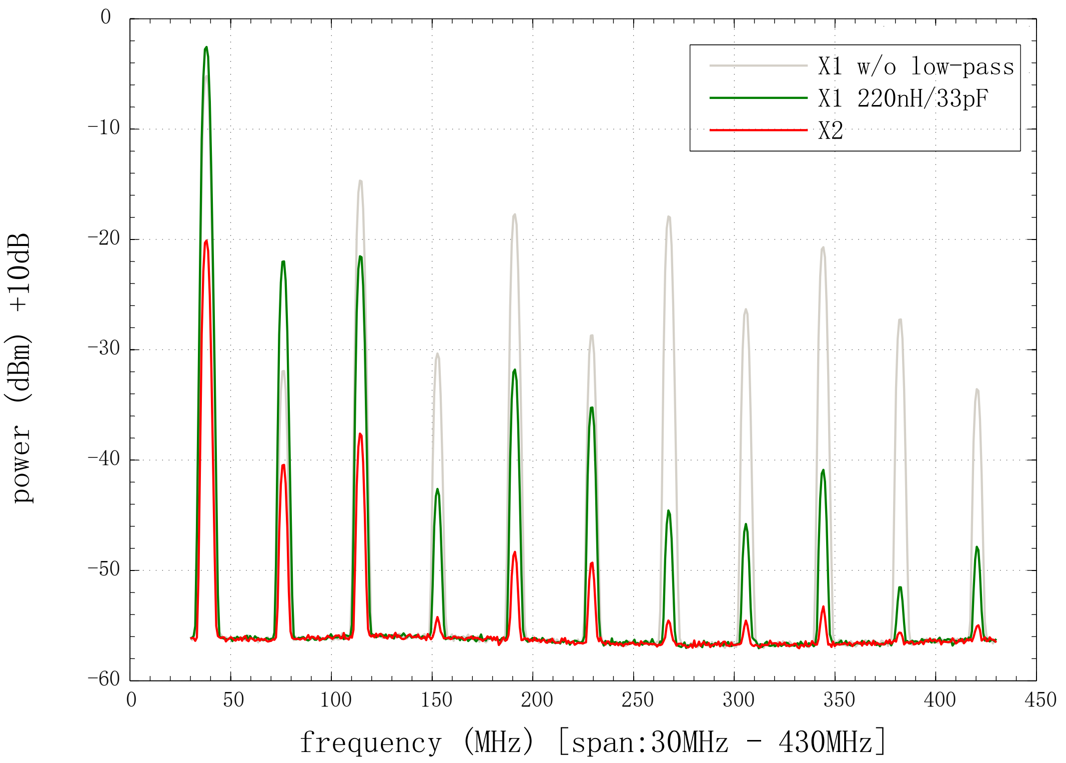

Figure 4.5 Performance of the EOM harmonic filter. Note that VCXO signal is split and directed into output ports $X1$ and $X2$ with different amplifications.

33250A), which has a measured linewidth of 1.2 Hz. It is safe to conclude that the home-built EOM driver module is expected to generate reasonably narrow sidebands useful for locking the laser to the cavity.

Testing the EOM Functionality

We test the sideband generation of the home-built EOM by directing the light passing through the EOM into a tunable Fabry–Pérot cavity, which is shown in Fig. 4.7. The EOM driver output power is enhanced using a mpa-10-40 amplifier with various attenuators to produce different modulation depth of the laser light. By scanning the piezo of the tunable cavity and recording the transmitted signal, we can map the frequency space into the time space. The resulting "time space" spectrum is shown in Fig. 4.7. According to Ref. [37], the optimal modulation depth occurs when the height of the first order sidebands is approximately 40% of the carrier, which indicates that the 26 dBm driving power is the optimal operating condition for the home-built EOM.

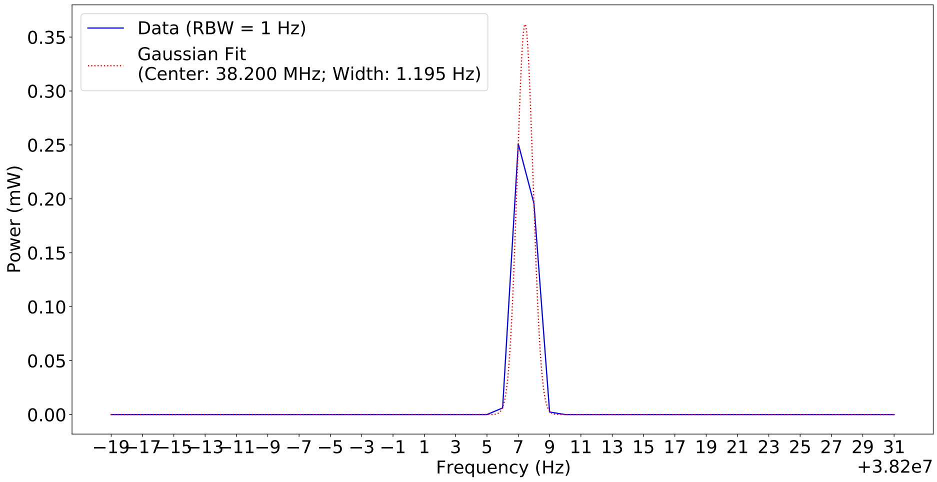

Figure 4.6 Spectrum of the EOM driver module output.

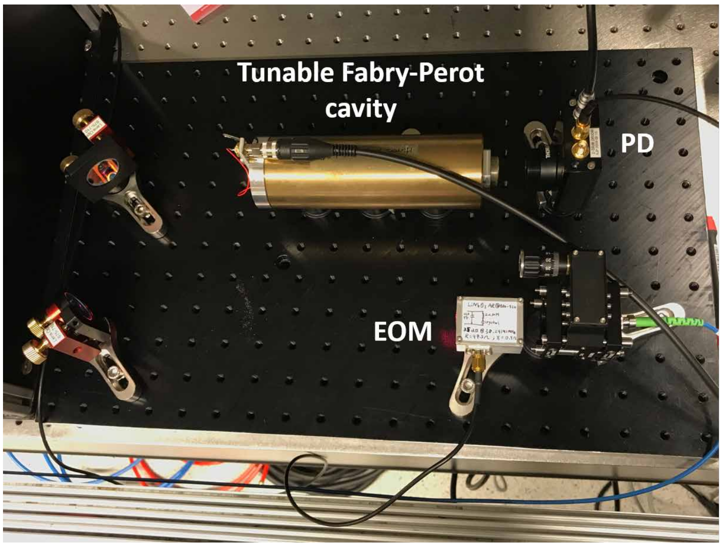

Figure 4.7 Optical setup for testing the sidebands generated by the home-built EOM.

4.1.3 The Dual Sideband Locking Scheme for the ^{1}S$_0$-^{3}P$_2$ Laser System

For the actual setup we employ a locking scheme developed from the standard PDH locking. The technique is called dual sideband locking, which uses a modulation spectrum that is identical to that used for PDH locking with a tunable offset from the carrier. This can be accomplished by modulating the beam at two different frequencies, one of which is adjustable. Consider a light beam with power P_0 and angular frequency ω_c being phase-

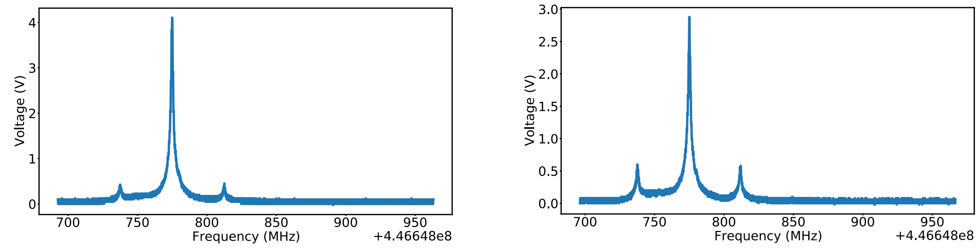

18 dBm **22 dBm**

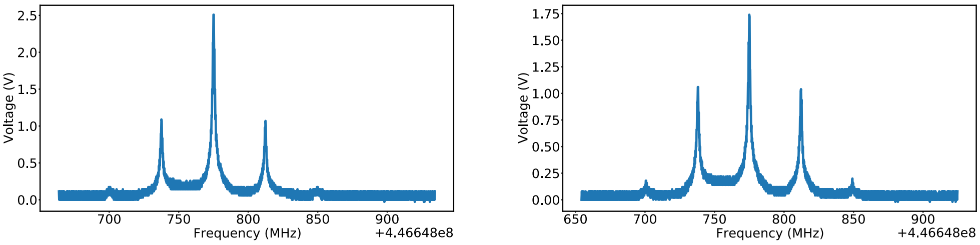

26 dBm **30 dBm**

Figure 4.8 Sidebands generated by the home-built EOM with various driving powers.

modulated with two sinusoidal signals of depth β_1, β_2 and angular frequencies Ω_1, Ω_2. The electric field is given by [40]:

$$E = \sqrt{P_0}\exp\{i[\omega_c t + \beta_1 \sin(\Omega_1 t) + \beta_2 \sin(\Omega_2 t)]\}. \tag{4.15}$$

Expanding to first order in $\beta_{1,2}$, the result of the phase modulation is a carrier with angular frequency ω_c, sidebands with angular frequencies $\omega_c \pm \Omega_1$, sidebands with angular frequencies $\omega_c \pm \Omega_2$, and sub-sidebands at $\omega_c + \Omega_1 \pm \Omega_2$ and $\omega_c - \Omega_1 \pm \Omega_2$.

The modulated spectrum for $\omega \geq \omega_c$ is shown in Fig. 4.9, assuming $\Omega_1 > \Omega_2$ and $\beta_1 > \beta_2$. Note that the spectral structure centered around $\omega_c + \Omega_1$ with sidebands offset by $\pm\Omega_2$ is analogous to the PDH modulation spectrum. In dual sideband locking, this structure (or the analogous one at $\omega_c - \Omega_1$) is used to generate an error signal by placing one of the $\omega \pm \Omega_1$ sidebands on resonance and demodulating the reflected power with Ω_2. Frequency tuning of the carrier for the lock can then be accomplished by adjusting Ω_1.

By allowing a tunable carrier frequency with respect to the cavity resonances, this locking technique in principle equips us with flexibility in adjusting the locked laser frequency without having to heavily rely on double-pass AOMs which are limited by their modulation bandwidth, hard to align, and consume a lot of optical power. One disadvantage of the dual sideband locking technique, however, is that the complex modulation structure makes lock acquisition challenging. Specifically, a PDH error signal can be generated

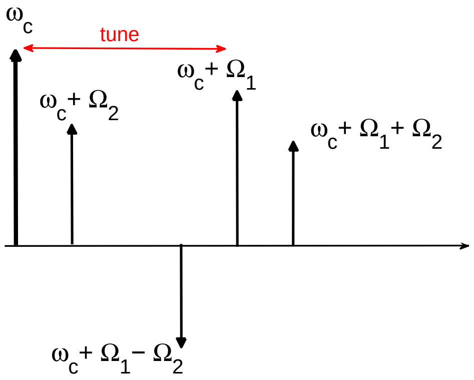

Figure 4.9 The modulated spectrum for $\omega \geq \omega_c$ assuming $\Omega_1 > \Omega_2$ and $\beta_1 > \beta_2$. Drawn following Ref. [40].

when the carrier ω_c is in resonance and the power is demodulated by Ω_2. If the modulation depth of the first modulator (Ω_1) is not large enough to sufficiently suppress the carrier, this error signal may even be larger than the desired dual sideband locking error signal. For us, this disadvantage is avoided to the largest degree by generating the Ω_1 sideband with the power that leads to an $\omega_c \pm \Omega_1$ sideband much more prominent than the $\omega_c \pm \Omega_2$ sideband.

The generation of the Ω_2 sidebands, in our case, is done by the home-built EOM presented in Section 4.1.2. The tunable Ω_1 sidebands are generated by a commercial fiber EOM from Jenoptik (Phasenmodulator PM660). The driving power is optimized at -16 dBm, which yields the largest sideband amplitude. The carrier for the lock is chosen to be the $\omega_c - \Omega_1$ sideband. The sidebands from the phase modulations are monitored by a scanning Fabry–Pérot cavity and the results are presented in Fig. 4.10.

The final locking scheme for the $^1S_0$-$^3P_2$ laser system is presented in Fig. 4.11. Light generated from the linear ECDL with frequency ω_c first passes the home-built EOM driven by the first oscillator with modulating frequency Ω_2, and then passes the fiber EOM driven by the second oscillator with modulating frequency Ω_1. The phase modulated light is then sent through a PBS and a quarter waveplate into the reference cavity. The -1st sideband ($\omega_c - \Omega_1$) of the modulated light is coupled to the cavity and the ($\omega_c - \Omega_1 \pm \Omega_2$) sidebands are reflected back, passing again the quarter waveplate and is directed by the PBS into the photodiode. The error signal for PDH locking is obtained by mixing the photodiode signal with the (phase matched) signal of the first oscillator, which is then low-passed and modulated by a PID loop filter. The signal after the loop filter is sent into the ECDL, forming a closed feedback loop to lock the laser frequency. Note that the transmitted light from the cavity is sent into a CMOS camera, which monitors the transverse mode.

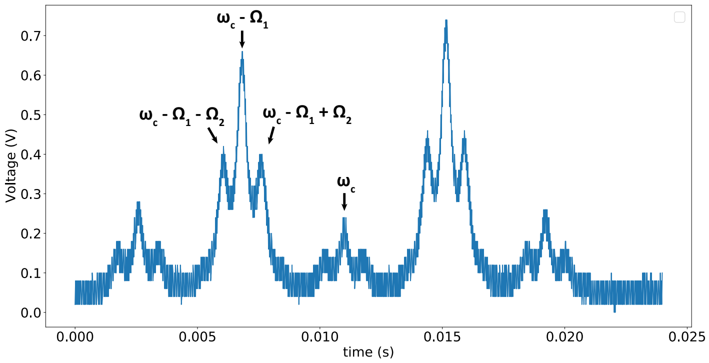

Figure 4.10 Sidebands from the dual sideband locking monitored by a Fabry–Pérot cavity. The driving power for the fiber EOM (Ω_1) is optimized at -16 dBm for a prominent 1$^{\text{st}}$ order sideband at $\omega_c \pm \Omega_1$.

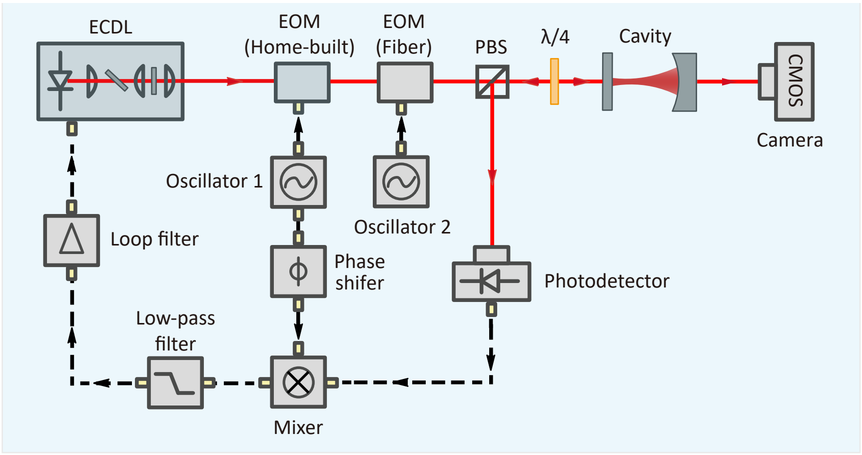

Figure 4.11 The locking scheme for the $^1S_0$-$^3P_2$ Laser System. Light from the ECDL is phase modulated by the home-built and commercial fiber EOMs, and is locked to the reference cavity based on the dual sideband locking scheme developed from the standard PDH lock.

Chapter 5

Optical Reference Cavity

As discussed in the previous Chapter, an essential part of the frequency-locking scheme for the $^1S_0$-$^3P_2$ laser is the optical reference cavity. In this Chapter, we will discuss the construction of an ultrastable cavity that couples the wavelength of the transmitted light with its cavity length. The cavity, when nicely isolated and protected, can be extremely stable against environmental disturbances.

5.1 Factors Characterizing an Optical Cavity

5.1.1 Free Spectral Range

The most common optical cavity consists of two metallic or dielectric mirrors separated by the cavity length (L). At first approximation, the modes of this resonator can be considered as the superposition of two plane EM waves propagating in opposite directions along the cavity axis. In this approximation, we can derive the resonance frequencies by imposing the condition that the phase shift of a plane wave due to one round-trip through the cavity must equal an integral multiple of 2π, which leads to the following expression [41]:

$$\nu_N = N \cdot \left(\frac{c}{2L}\right) = N \cdot \mathrm{FSR}, \tag{5.1}$$

where N is an integer and ν_N is the N^{th} resonant frequency of the cavity, c is the speed of light, and FSR $= c/2L$ is the free spectral range of the cavity.

5.1.2 Quality Factor and Finesse

Having calculated the photon lifetime (τ_c) in an optical cavity in Eqn. 2.18, we can now describe the electric field at any point inside the resonator as a plane-wave with an exponentially decaying amplitude: $E(t) = E_0 \exp(i\omega t) \exp(-t/2\tau_c) + c.c.$, where ω is the angular frequency of the mode, and $c.c.$ stands for complex conjugate. Note that the same temporal behavior also applies to the field of the light leaving the cavity through the output mirror. Taking the Fourier transform of this field (for $t > 0$) we can find that the power spectrum of the emitted light has a Lorentzian line shape with linewidth (FWHM):

$$\Delta\nu_c = \frac{1}{2\pi\tau_c}. \tag{5.2}$$

We now introduce an important quality factor which is strictly related to the cavity photon lifetime. This is the cavity Q-factor which is defined, for any resonant system, as 2π times the ratio between the energy stored in the resonator and the energy lost in one oscillation cycle [18]. Therefore a high cavity Q-factor indicates low losses in the resonant system. Since in our case the energy stored is $\phi h\nu$ (ν is the laser frequency) and the energy lost per cycle is $(-\mathrm{d}\phi/\mathrm{d}t)$, we obtain

$$Q = -\frac{2\pi\nu\phi}{\mathrm{d}\phi/\mathrm{d}t} = \frac{\nu}{\Delta\nu_c}, \tag{5.3}$$

where Eqn. 5.2 and the exponential decay law $\phi(t) = \phi_0 \exp(-t/\tau_c)$ for the stored cavity photon ϕ have been used.

Another important factor characterizing the cavity is the finesse (F), which is a measure for how narrow the resonances are in relation to their frequency distance: a high finesse means sharp resonances. It is defined as the free spectral range divided by the linewidth $\Delta\nu_c$ of the resonances [42]:

$$F = \frac{\mathrm{FSR}}{\Delta\nu_c}. \tag{5.4}$$

Note that this parameter is fully determined by the resonator losses and is independent of the resonator length. Finally, the Q-factor is related to finesse via:

$$Q = \frac{F \cdot \nu}{\mathrm{FSR}}. \tag{5.5}$$

5.2 Frequency Stability of an Optical Cavity

In a more generalized situation where the refractive index of the medium is not assumed to be 1, Eqn. 5.1 becomes:

$$\nu_N = \frac{Nc}{2Ln} \tag{5.6}$$

where n is the refractive index inside the cavity. To see how changes in L and n influence ν, let us take the total derivative of Eqn. 5.6. We can find that any fractional change in cavity length and refractive index will lead to a fractional instability of the resonant wavelength ν in that :

$$\frac{\mathrm{d}\nu}{\nu} = -\frac{\mathrm{d}L}{L} - \frac{\mathrm{d}n}{n} \tag{5.7}$$

Given that the ${}^1\mathrm{S}_0$-${}^3\mathrm{P}_2$ transition is roughly 4.47×10^{14} Hz [13], a stability on the order of 1 Hz of the wavelength requires a fractional stability on the order of 10^{-15} for cavity length and refractive index. Note that we are talking about stability in the sub-atomic regime, as such a length stability is on the order of a nucleon radius. In the following we will cover the most prominent factors in the lab affecting the cavity length and the index of refraction. We will also discuss the measures we can take in our design to meet this challenging task.

5.2.1 Thermal Expansion

The first key factor contributing to the length change of the cavity is through thermal expansion. For a real material, its coefficient of linear thermal expansion (CTE) is given by:

$$\alpha_T = \frac{1}{L}\frac{\partial L}{\partial T}, \tag{5.8}$$

where $\partial L/L$ is the fractional change of its length, caused by a change in temperature ∂T. In this case the fluctuation in temperature can change the distance between the two mirrors inside the cavity via thermal expansion, leading to a broadening effect in the laser linewidth. Note that CTE is dependent on temperature, and for the ultra low expansion (ULE) material that we are using for the cavity there exits a zero crossing temperature where CTE vanishes [43]. It is thus crucial to not only separate the two mirrors with spacers that have extremely low CTEs, but also maintain a cavity temperature as close to the zero crossing temperature as possible. It is certainly also of great importance to reduce the temperature fluctuation of the cavity at the first place.

5.2.2 Vibrations

The next factor reducing the stability of the cavity length is the elastic deformation caused by external forces, i.e., vibration. The total length change of a material due to an external force is given by Young's modulus (E) [44]:

$$E = \frac{Fd}{A\Delta d}, \tag{5.9}$$

where an external force F is applied onto the area A with length d, causing a change of length Δd. There are several measures we can take to make the cavity more stable against vibrations. One is to increase the cross section of the cavity, or choose a material with a relatively larger Young's modulus as the spacer between the two mirrors. Moreover, we can lower the effect of vibration on cavity length by supporting the cavity in a way that length changes induced by vibrations cancel out each other. These supporting points can be found via finite element analysis [45] and can be incorporated in the design of the cavity housing. Additionally, we can employ a vibration isolation platform to decouple the cavity from vibrational effects. It is also possible to absorb vibrations by selecting an elastic material as supporting pads for the cavity. Finally, to account for acoustic vibrations we can construct an acoustic shield enclosing the entire cavity system.

5.2.3 Pressure Fluctuations

We note from Eqn. 5.7 that not only variations in the cavity length can cause changes in the resonant frequency, the change of the optical path length inside the cavity due to fluctuations of the air pressure can also lead to unwanted disturbances to the laser stability. In the following we will obtain a rough estimate of the effect of pressure fluctuations on the change of refractive index. At a pressure of one atmosphere ($p = 1013.25$ mbar) air has a refractive index of $n_{\text{air}} = 1.0003$, and at vacuum ($p = 0$ mbar) we have $n_{\text{vac}} = 1$ by definition. Assuming a linear relation, we can interpolate an expression for $n(p)$:

$$n(p) \approx 1 + \frac{2.96 \times 10^{-7}}{\text{mbar}} p, \tag{5.10}$$

where p is the pressure of air inside the cavity. By differentiating and using Eqn. 5.7, we have:

$$\frac{\partial \nu}{\nu} = -\frac{2.96 \times 10^{-7}}{\text{mbar}} \partial p \tag{5.11}$$

From Eqn. 5.11 we find that to keep the cavity frequency stability within the 10^{-15} range, we need a target pressure stability of at least 10^{-8} mbar. It becomes evident that the cavity needs to be operated in vacuum to achieve such a low pressure stability. For the maximum vacuum pressure, assuming a low fractional pressure instability of one-percent, it is thus necessary to keep a vacuum pressure below 10^{-6} mbar.

5.3 Design of the Ultrastable Reference Cavity

Having discussed the challenges for a stable frequency reference for the $^1S_0$-$^3P_2$ laser, we will now present the actual design of such an ultrastable reference cavity. The cavity for the laser is the second generation reference cavity for our laboratory. In the following section, we will focus on the main design aspects of this cavity, and refer the readers to Ref. [46] for the detailed assembly processes.

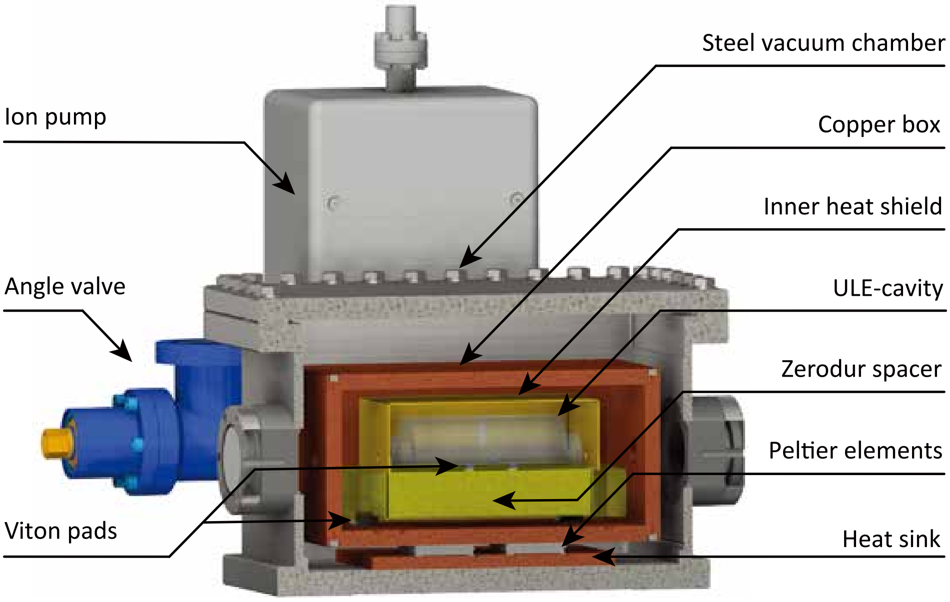

Figure 5.1 Schematic of the cavity housing. The vacuum chamber contains a copper box standing on two Peltier elements, which are mounted on a copper plate acting as a heat sink. Inside the copper box the Zerodur holder of the cavity stands on Viton pads. An inner heat shield is laying on the Zerodur spacer and surrounds the ULE-cavity. Attached to the cavity are the ion pump and the angle valve. Adapted from Ref. [46]

A schematic of the cavity housing is presented in Fig. 5.1. The optical resonator is purchased from Stable Laser Systems for our cavity. A plane mirror and a concave mirror with radius of curvature 500 mm are separated by a spacer made of a ULE glass of type 6020-4 Notched Spacer, with a length of 100 mm. The zero crossing temperature is measured by the company to be 32.75 °C with 1 °C uncertainty. The ULE resonator is surrounded by an inner heat shield (copper alloy EN CW008A) homogenizing the thermal radiation between the optical resonator and the environment and acting as a passive low-pass filter for changes in temperature. The ULE resonator and the heat shield are mounted on a Zerodur support spacer with two Viton pads for vibration isolation attached on the top and the bottom of the Zerodur spacer.

Enclosing the ULE resonator, Zerodur spacer and the inner heat shield is a copper box (EN CW008A) of which the temperature is actively stabilized. For temperature controlling, instead of Kapton heaters used in the previous generation, we implement Peltier elements (TE-2-(127-127)-1.15 from TE Technology) which have lower outgassing rates capable of achieving a pressure on the order of 10^{-9} mbar [47]. In between the Peltier elements and the copper parts we place a 0.1 mm thick indium foil to ensure an optimal thermal contact.

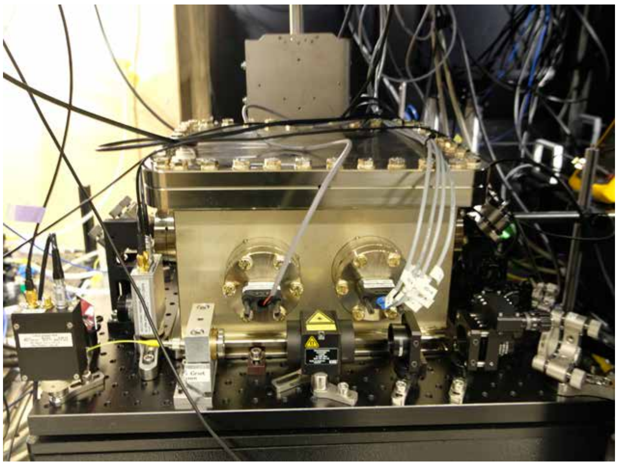

Figure 5.2 Photo of the reference cavity sitting on the vibration isolation platform.

To meet the ultrahigh vacuum operating condition described in the previous section, a stainless steel (AISI 304) chamber vacuum housing is designed, allowing the use of copper gaskets which can reduce the leak rates below 10^{-11} (mbar l s^{-1}) [48]. A total of five CF-40 flanges sealed with copper gaskets are used for the vacuum chamber. Two of them are mounted in the front of the cavity for D-SUB-9 electrical feedthroughs for the wiring of the Peltier elements. Another two CF-flanges are attached with viewports for light transmission and are mounted such that light coupled with the cavity enters directly through the center of the viewport. The viewports are antireflection-coated and angled with 0.5 ° to the surface of the steel chamber to prevent etaloning effects. The fifth flange connects the back of the chamber via a 5-way-cross to the ion pump. Here a Gamma Vacuum 10SW ion pump is employed to pump both noble gases and hydrogen with vibration-free pumping, delivering a pressure way below the specified target pressure of 10^{-8} mbar. A turbo pump can also be connected to the 5-way-cross via the angle valve to provide initial pumping. The lid and the chamber are attached with a custom rectangular copper gasket for high-standard vacuum sealing.

Lastly, to boost the vibration isolation performance, we employ the vibration isolation platform 150 BM-8 from Minus-K Technology, which can well hold the total weight (about 65 kg) of the assembled cavity system in Fig. 5.1 and is large enough for both the cavity and the associated optics. The vibration isolation platform is able to damp by 40 dB and 20 dB for any vertical and horizontal accelerations above 5 Hz, respectively. The actual picture of the assembled cavity sitting on the vibration isolation stage is presented in Fig. 5.2.

5.4 Characterization of the Reference Cavity

After the careful assembly of the aforementioned components following instructions in Ref. [46], we are able to achieve a vacuum pressure of 1.5×10^{-8} mbar at the zero crossing temperature. To obtain the cavity finesse at this condition, we need to know the FSR and the cavity photon lifetime. Since the separation between the two mirrors of the ULE resonator is 100 mm, the FSR of the cavity is $c/2L = 1.5$ GHz.

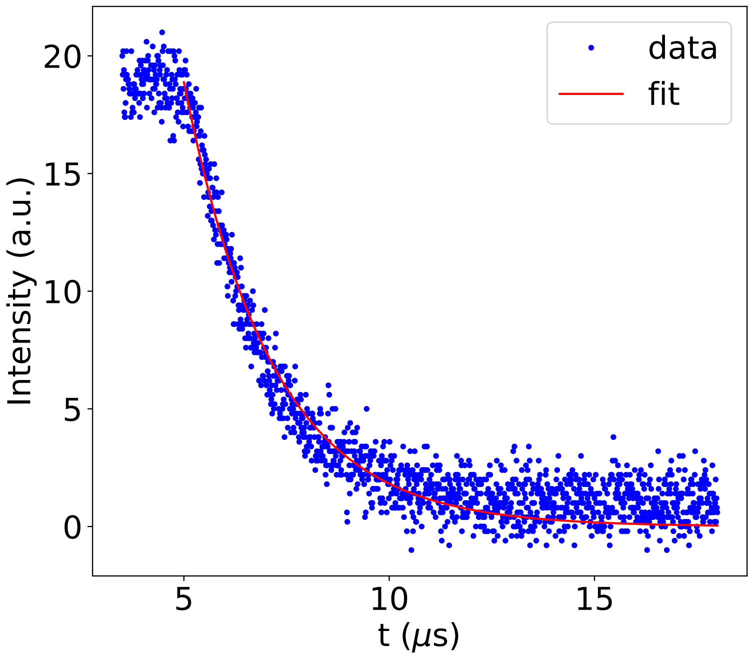

Figure 5.3 A ring-down measurement of the intensity stored inside an optical cavity. A fit of the data (blue) with an exponential intensity decay (red) reveals a ring down time of 2.14 µs. Given the FSR is 1.5 GHz, the ring down time corresponds to a cavity finesse of 20200.

To obtain the photon lifetime, we perform a cavity ring down measurement. For this measurement, we need to lock the laser onto one of the resonances of the corresponding cavity and we must be able to switch off the laser light very rapidly. Since the time scale for the photon lifetime is on the order of μs, simply shutting down the laser or blocking the beam is not fast enough. To perform a rapid shut-off, we let the laser beam pass through an acousto-optic modulator (AOM) and couple one of the diffracted beams from its output into the cavity. Since the AOM is controlled electrically, the diffracted light can be shut off within nanoseconds. The result of the ring down measurement is shown in Fig. 5.3. The transmission light intensity is measured and a fit of the data with an exponential intensity decay reveals a photon lifetime $\tau_c = 2.14$ μs. Together with the

1.5 GHz FSR, we obtain a cavity finesse of 20200. This finesse corresponds to a cavity linewidth of 75 kHz according to Eqn. 5.2.

Note that the ULE resonator assigned by the group for the slicing cavity is taken from an old cavity previously used for the red mot ($^1S_0$-$^3P_1$) and clock ($^1S_0$-$^3P_0$) transitions, of which the mirrors were coated to be optimized for 689 nm and 698 nm. This nonideal coating could explain the limited finesse for the slicing transition at 671 nm. We have also coupled the home-built clock laser at 698 nm into this cavity, and another ring down measurement shows a cavity photon lifetime of 32 μs corresponding to a finesse of 300000 and a cavity linewidth of 5 kHz for the clock laser, which confirms that the limited finesse for the 671 nm is unlikely to be due to any misoperation in the assembling process, but is due to the choice of the mirror coating.

Finally, we should note that the linewidth of the laser is actually much narrower than the cavity linewidth. From a previous beat measurement conducted in Ref. [15], the 5 kHz cavity linewidth of the clock transition leads to a final laser linewidth on the Hz level, which is three orders of magnitude narrower than the cavity linewidth. Comparatively, and from a conservative point of view, we estimate that the $^1S_0$-$^3P_2$ laser linewidth is at least one order of magnitude less than its cavity linewidth, which is on the order of 1 kHz. Recall that the frequency splittings between adjacent layers in our lattice are 33 kHz for ^{87}Sr and 25 kHz for ^{88}Sr. A $^1S_0$-$^3P_2$ laser with a linewidth on the order of 1 kHz is thus sufficient for our purposes.

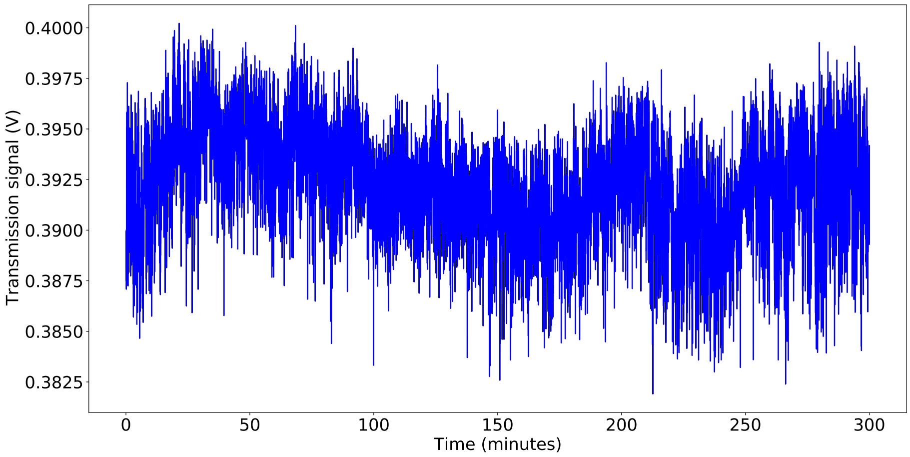

Figure 5.4 Cavity transmission of the $^1S_0$-$^3P_2$ laser light measured over 5 hours.

Since we have not completed the upgrading of the vertical lattice at this point where we could adjust the beam polarization to make the transition frequency independent of lattice power [6], we could not perform more direct measurement of the $^1S_0$-$^3P_2$ laser linewidth through spectroscopy experiments of Sr. However, we could obtain information of the laser linewidth indirectly from the stability measurement of the cavity transmission. As shown in Fig. 5.4, we monitor the transmission signal of the reference cavity over 5 hours for the $^1S_0$-$^3P_2$ laser light. The fluctuation of the transmission signal is within a range of 1-2%. If we assume a Lorentzian lineshape for the cavity resonance, and we relate the cavity transmission instability with the laser instability, we find that a width 1-2% away from the peak corresponds to a laser linewidth of a few kHz, which confirms our previous estimation. Note that this is only a rough inference of the linewidth, and further measurements need to be conducted for a more accurate knowledge.

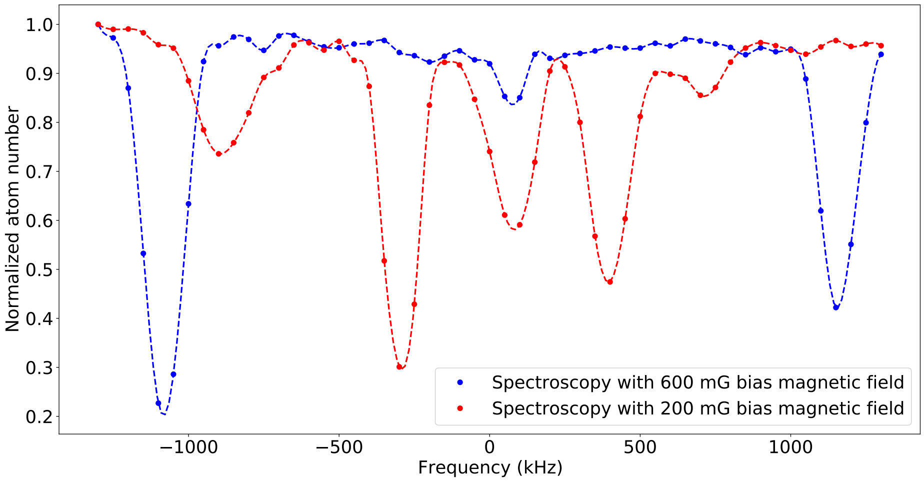

Figure 5.5 Spectroscopy of ^{88}Sr in the transport lattice with bias magnetic fields at 200 mG and 600 mG.

Finally, let us take a look at a preliminary spectroscopy experiment with ^{88}Sr in the transport lattice. During this experiment, we drive the ground state atoms to the excited states with different Zeeman levels using the $^1S_0$-$^3P_2$ laser. As shown in Fig. 5.5, at a bias magnetic field of 200 mG, we are able to observe all the five m_J states with $m_J = 0$, ± 1, and ± 2 by scanning the laser frequency ± 1300 kHz away from the locking frequency. When we increase the bias field to 600 mG, the Zeeman splitting increases as predicted by 2.1 MHz/G. Since the transport lattice is not magic for the $^1S_0$-$^3P_2$ transition, we could not rely on this spectroscopy data to deduct the laser linewidth. However, it is still a promising sign that our $^1S_0$-$^3P_2$ system is working.

Chapter 6

Active Temperature Stabilization via the Cavity Protection Box

As discussed in Sec. 5.2, the environment has a significant influence on the frequency stability of an ultrastable optical cavity. Particularly, looking at the effect of thermal expansion from Eqn. (5.8), we can deduct that to achieve the desired fractional stability of the cavity length, the multiplication of the coefficient of thermal expansion (α) with the change of temperature (ΔT) needs to be within 10^{-15}. The ULE optical resonator at zero crossing temperature has a coefficient of thermal expansion of $\alpha = 1.7 \cdot 10^{-9} K^{-1}$ [49], which means that the required ΔT needs to be within 1 mK.

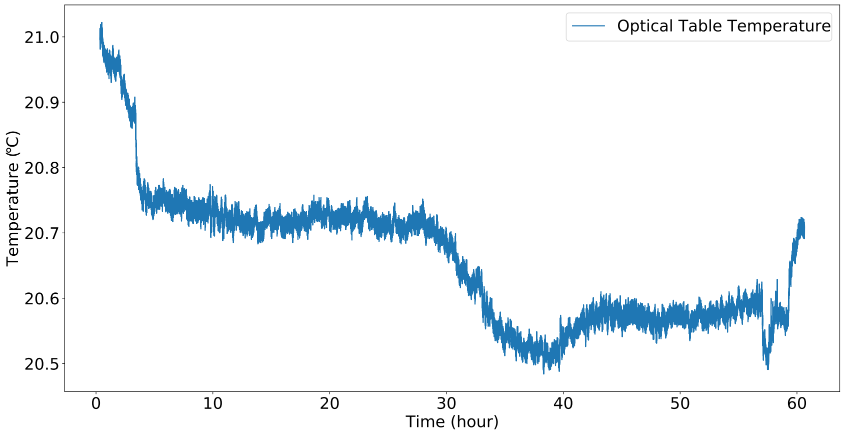

Figure 6.1 Temperature fluctuation of the optical table. This data is measured by a thermal coupler during the weekend with all windows of the optical table closed. Note that the absolute value of the temperature may be off by 1 or 2 degrees, but the relative change of temperature, which is what we are interested in, is expected to be of good accuracy.

The reference cavity presented in Sec. 5.3 is designed to provide the ultimate stability to the inner optical resonator. However, as a "fine-tuning" device the vacuum chamber alone may not be enough to deliver the optimal performance when emerged with more aggressive environmental fluctuations. As we can see from Fig. 6.1, the optical table, though has its own (rough) temperature stabilization system, has a non-negligible daily temperature fluctuation of 0.5 K. Note that this temperature data is taken during the weekend when all the windows of the table are closed and represents the ideal case. During the normal operating hours when the windows are likely to be opened and closed constantly, the temperature fluctuation on the optical table where the cavity sits is going to be even larger. To this end, a protection box surrounding the cavity is constructed to provide extra suppression against environmental noise and active temperature stabilization for the reference cavity.

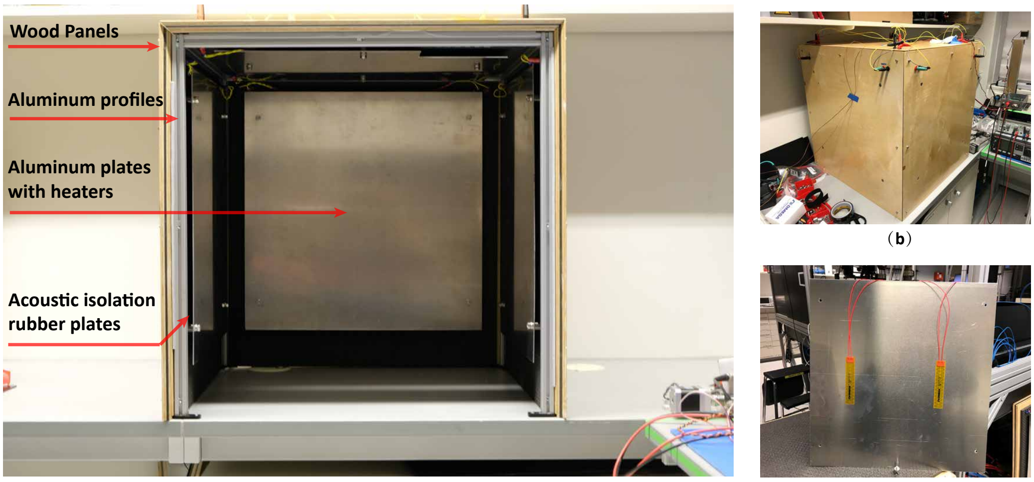

(b)

(a)

(c)

Figure 6.2 Assembled cavity protection box. (a) Inside of the protection box. Side plates are mounted on an aluminum profile. Each side consists of (from outermost to innermost) a wood panel, an acoustic isolation rubber plate, and an aluminum plate attached with Kapton heaters. (b) The outside of the protection box with all sides closed. (c) The attachment of the Kapton heaters on the aluminum plate. Note that heaters face the wood panel when assembled.

The assembled protection box is presented in Fig. 6.2. The wood box consists of five 16-mm-thick BaryVam acoustic isolation wood panels, which are stably mounted on an aluminum profile serving as the frame for the protection box. The outer side of the wood panel is first painted with Clou Wooden Seal, then manually sanded, and painted again for sealing of surface wooden particulates that could spread onto the optical table causing damages to surrounding optical components. For each wood panel, an acoustic shielding rubber foam is glued inside to better resist pressure fluctuations from the air (acoustic noise). An aluminum plate with high thermal conductivity is mounted with steel posts on each wood panel, sandwiching the acoustic isolation foam. Two radiative Kapton heaters (Omega kHLva-105/10-P) are attached on the outer side of the aluminum plate which allows heat to be radiated onto the cavity homogeneously. On the outer side of each wood panel, there are four banana sockets through which we can electrically connect the positive and negative ends of the two heaters with external power supplies.

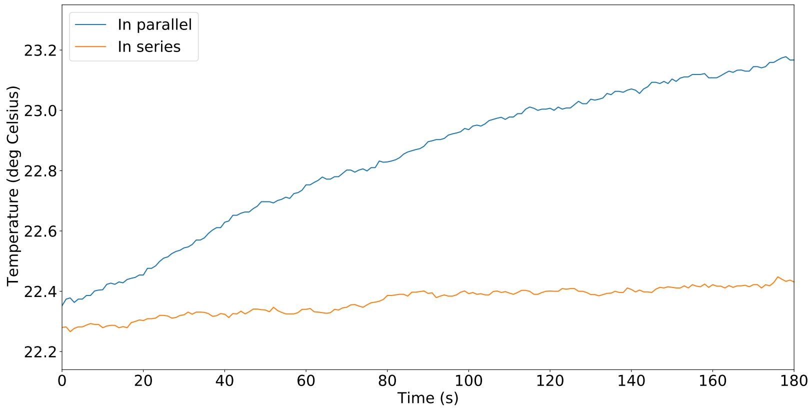

Figure 6.3 Heating performance for the in-parallel and in-series connecting configurations.

6.1 Connection of the Heaters

Note that there is a total of 10 heaters for the entire protection box (2 heaters per side × 5 sides) and the first thing we should figure out is whether we should connect them in series or in parallel. Given that we are using a fixed-voltage laboratory power supply (EA-PS 3032-10 B), we can calculate the overall power for each configuration as:

$$\begin{aligned} P_{parallel} &= 10 \cdot \frac{V^2}{R}; \\ P_{series} &= \frac{1}{10} \cdot \frac{V^2}{R}, \end{aligned} \tag{6.1}$$

which indicates that the in-parallel connection can in principle deliver 10^2 more heating power than the in-series case. This prediction is confirmed with the actual temperature data presented in Fig. 6.3, which shows that the in-parallel connection indeed exhibits a much stronger heating power over the in-series case. The actual setup of the heater connection is shown in Fig. 6.4.

6.2 Analysis of the Protection Box Heat Dissipation

In the following, we will provide an estimation of the heat dissipation of the protection box to gain insights about the required output power level when selecting the right temperature servo. There are three channels for (passive) heat dissipation: radiation, convection, and conduction. In our application, the only contacting area for conduction is limited to the four lower edges of the wood panels (with thickness ≈ 0.5 mm) as can been seen

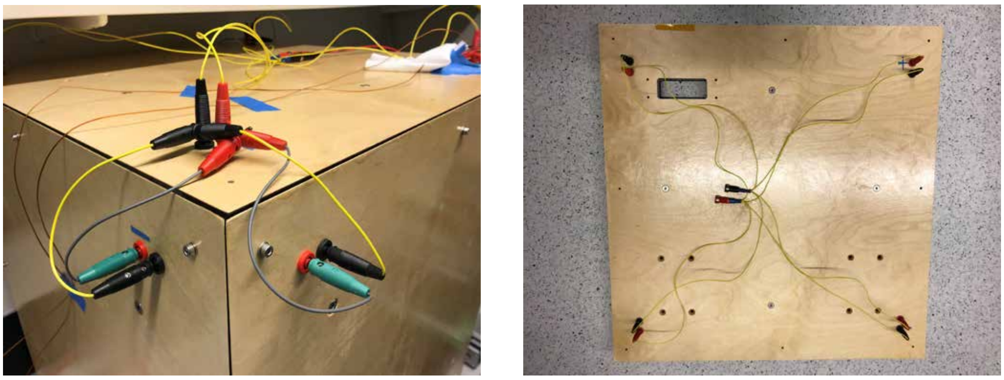

(a) (b)

Figure 6.4 In-parallel wire connection of the Kapton heaters. (a) Each heater is connected independently to the banana socket at the adjacent corner. (b) The four corners are connected to the main sockets on the top plate, which are then driven by a single power source, ensuing an in-parallel configuration for the entire setup. Note that for the double-power-source setup, the configuration is slightly changed as there will be two sets of sockets on the top, each responsible for half of the heaters.

in Fig. 6.2 (a). In this case, conduction heat loss is small and can be ignored. Following the material in Ref. [50], we write the following equation for the heat dissipation of our system:

$$Q_{\text{dissi}} = Q_{\text{rad}} + Q_{\text{conv}} = F\epsilon\sigma A(T_H^4 - T_C^4) + hA(T_H - T_C), \tag{6.2}$$

where T_H and T_C are the inside and outside temperatures, respectively, F is the shape factor, ϵ is the emissivity, σ is the Stefan-Boltzman constant, A is the surface area, and h is the convective heat transfer coefficient. We present in Table 6.1 the assumed values for the aforementioned parameters.

Symbol	Meaning	Parameter Value
F	Shape Factor	Assume a worst-case value of 1
ϵ	Emissivity	Emissivity for wood is 0.924
σ	Stefan-Boltzman constant	$5.667 \cdot 10^{-8} W/m^2K^4$
A	Area of the cooled surface	For a single wood surface: $0.655m \cdot 0.645m = 0.422m^2$
h	Convective heat transfer coefficient	For air at 1 atm., $h = 21.7W/°Cm^2$

Table 6.1 Parameters and their assumed values for the heat dissipation equation in Eqn. 6.2.

Plugging the parameters shown in Table 6.1 into Eqn. 6.2 and assuming an inside temperature of 295 K (about 22 °C), the expected heat dissipation for the entire protection box at a given inside-outside temperature difference is calculated and summarized in Table 6.2. Given that the temperature fluctuation of the optical table is about 0.5 K, the power source for the box must be able to output a power larger than 28.56 W to balance out the heat dissipation. Note that the maximum heating power for each Kapton heater is 50 W, which should be more than enough for our purposes.

$\Delta T(K)$	**Dissipation Power (W)**
0.1	5.71
0.2	11.42
0.25	14.28
0.3	17.13
0.4	22.85
0.5	28.56
0.55	31.42
0.6	34.28
0.8	45.71
1.0	57.15

Table 6.2 Protection box heat dissipation power at various inside-outside temperature differences.

6.3 Introduction to Proportional-Integral-Derivative (PID) Control

The active temperature stabilization system for the protection box is composed of a temperature adjustment element (Kapton heater), a sensor (thermistor), and a servo controller (digital or analog). Generally speaking, the senor provides information about the present system status to the servo, which generates an error value based on the difference between the measured value and the desired (set) value. The error value is then modified by the servo based on a specific set of rules, and is output to drive the temperature adjustment element. The sensor, servo, and temperature adjustment element together form a closed-loop, which can drive and sustain the system to a desired state.

In our case, the rule that the servo controller follows to modify the error signal is called Proportional-Integral-Derivative (PID), and the servo is thus called a PID controller. As an extremely effective and widely used control system, the PID controller is able to capture the history of the system (through integration) and anticipate the future behavior of the system (through differentiation) [51]. In the following, we will discuss the effect of each of the PID parameters on the dynamics of a closed-loop system and will demonstrate how to use a PID controller to improve a system's performance. The materials presented here follow closely to Ref. [51] and Ref. [50]. Interested readers are also encouraged to refer to Ref. [52] and Ref. [53] for more in-depth understanding of PID tuning and control theory.

6.3.1 PID Overview

PID control systems usually come in one of two standard forms, independent or dependent, depending on how the proportional gain is applied. For the independent form the proportional gain k_p is applied only to the error value, while for the dependent form it is applied to the integral and derivative terms as well. In the following we will take the independent form as an illustration. A schematic revealing how the PID controller works in a closed-loop system is shown in Fig. 6.5.

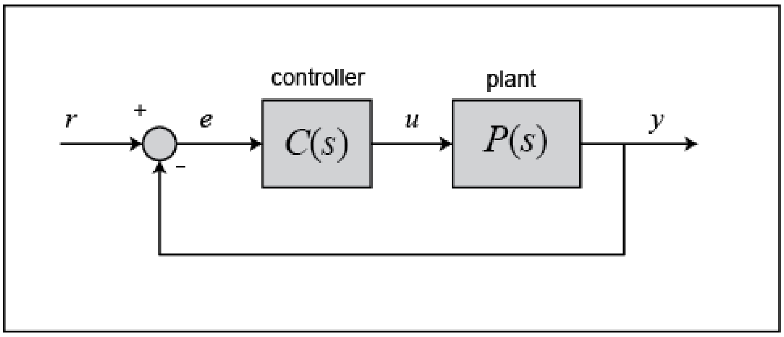

Figure 6.5 Schematic of the PIC control loop. Adapted from Ref. [51].

The variable (e) in Fig. 6.5 represents the tracking error, which is the difference between the desired level (r) and the actual level (y). This error signal (e) is fed into the PID controller, and the controller computes both the derivative and the integral of this error signal with respect to time. The control signal (u), according to Eqn. 6.3, is equal to the summation of the proportional gain (k_p) times the magnitude of the error, the integral gain (k_i) times the integral of the error, and the derivative gain (k_d) times the derivative of the error. The control signal (u) is then fed into the plant and the new output (y) is obtained. In this way, the error signal is constantly updated and the process continues while the controller is in effect.

Mathematically, the output $u(t)$ of a PID controller is calculated in the time domain from the feedback error $e(t)$ as:

$$u(t) = k_p e(t) + k_i \int e(t)\mathrm{d}t + k_d \frac{\mathrm{d}e(t)}{\mathrm{d}t}, \tag{6.3}$$

Note that the integral and derivative gains are usually expressed as time constants. For the independent form, the integral time constant is given by $T_i = 1/k_i$ and the derivative time constant is $T_d = k_d$.

6.3.2 Roles of the P, I, and D Parameters

Simpler control loops utilize only the proportional gain stage. Increasing the proportional gain (k_p) has the effect of proportionally increasing the control signal for the same level of error: with higher k_p the controller will "push" harder for a given level of error helping the closed-loop system to react more quickly. However, with increased proportional the system is also likely to overshoot more. Additionally, the proportional gain alone cannot produce a zero error between the temperature setpoint and sensor feedback, thus leaving a finite steady-state error.

The addition of an integral term to the controller (k_i) tends to help reduce the steady-state error: for a persistent, steady error, the integrator builds and builds, thereby gradually increasing the control signal and eventually driving the error down. However, a drawback of the integral term is that it can make the system more inert and oscillatory, since when the error signal changes sign, it may take a while for the integrator to “unwind.”

The addition of a derivative term to the controller (k_d) adds the ability of the controller to “anticipate” error. With derivative control, the control signal can become large if the error begins sloping upward, even when the magnitude of the error is still relatively small. This anticipation tends to increase stability of the loop by adding damping to the system, thereby decreasing overshoot. The addition of a derivative term, however, has no effect on the steady-state error.

Response	Rise Time	Overshoot	Settling Time	Steady-state Error
k_p	Decrease	Increase	Small change	Decrease
k_i	Decrease	Increase	Increase	Decrease
k_d	Small change	Decrease	Decrease	No change

Table 6.3 Effects of an increase of each controller parameter (k_p, k_d, k_i) on the system dynamics. Note that rise time denotes the time it takes for the plant output to rise beyond 90% of the desired level for the first time. Overshoot measures how much the peak level is higher than the steady state value. Settling time is the time it takes for the system to converge to its steady state. And steady-state error is the difference between the steady-state output and the desired output. Adapted from Ref. [51].

The general effects of an increase of each controller parameter (k_p, k_d, k_i) on a closed-loop system are summarized in Table 6.3, and simulations of the effects of proportional and integral gains on the system dynamics is presented in Fig. 6.6. One can also download a very useful PID simulator based on Excel from Ref. [54]. Note, these guidelines hold in many cases, but not all. If we truly want to know the effect of tuning the individual gains, we will have to do more analysis or perform testing on the actual system. Lastly, keep in mind that we do not need to implement all three controllers (proportional, derivative, and integral) into a single system. For example, if a PI controller meets the given requirements, we do not need to implement a derivative controller on the system. We should always keep the controller as simple as possible.

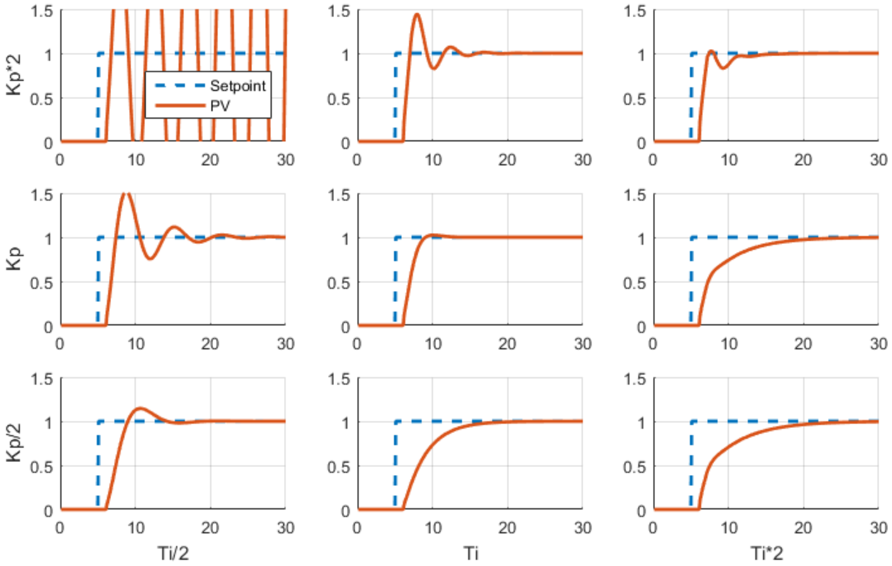

Figure 6.6 Simulation of the effects of proportional and integral gains on the system dynamics. In this simulation, small $(k_p/2)$, medium (k_p), and large $(k_p \cdot 2)$ values of the proportional gain as well as small $(T_i \cdot 2)$, medium (T_i), and large $(T_i/2)$ values of the integral gain (note that T_i is reversely proportional to k_i) are combined to give a total of nine simulations. PV (process value) denotes the system output, and Setpoint denotes the desired system level. The simulations closely resemble the guidelines presented in Table 6.3. Adapted from Ref. [55].

6.3.3 Ziegler-Nichols Method for Finding the Initial PID Parameters

By following the guidelines in table 6.3 and adjusting one control parameter at a time, we can gradually improve the performance of the system. However, to a large extent, the final performance is greatly limited by the choice of the initial parameters. If the initial set of parameters are totally off, we will be very likely to find the system in an awful state even after a tremendous amount of fine-tuning.

Ziegler and Nichols conducted numerous experiments and proposed rules for determining values of k_p, k_i, k_d [53], which give a fairly reliable estimate for the system parameters. The methods is as follows. First, the proportional gain should be set in the middle of the gain range, and then be increased in small steps. After each step, apply a small change to the setpoint and record the system dynamics before reaching an equilibrium. With sufficient proportional gain, the temperature will begin to exhibit damped oscillation as exhibited in Fig. 6.7. If the system begins to oscillate on the first try, simply reduce the gain in steps until the system exhibits the damped response. The proportional gain value that just starts oscillations is referred to as the critical gain k_c. The optimal proportional gain will be about half of this value. If the controller proportional gain cannot, or can only hardly be increased to the level necessary to drive the system into oscillation, then it may not be the appropriate device for the load, as operating any linear controller near its maximum settings can result in non-linear response [50].

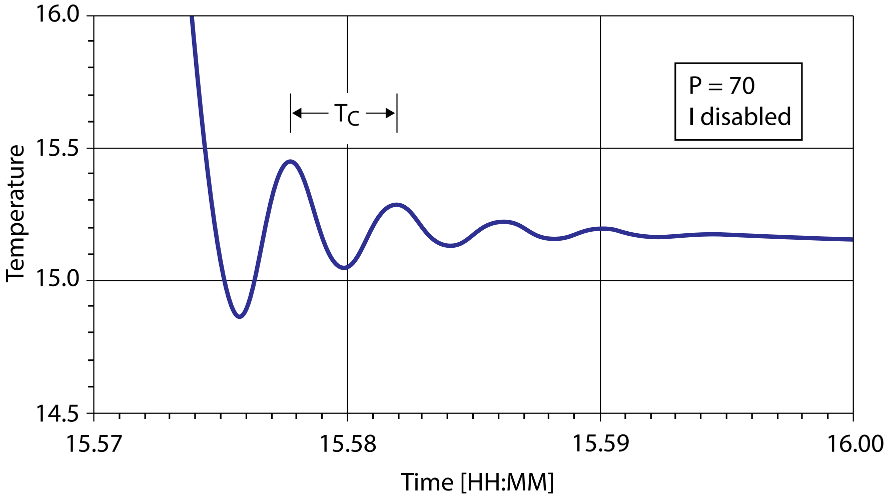

Figure 6.7 Damped oscillation for the Ziegler-Nichols Method. The critical proportional gain (k_c) is the gain necessary to cause the temperature to begin damped oscillations. The oscillation period is T_c. Adapted from Ref. [50].

Next, estimate the period of the oscillation. Further increases in the proportional gain will result in sustained oscillations with a period referred to as the critical period T_c as shown in Fig. 6.7. It is also okay to estimate the critical period made from the damped oscillations, which will usually be within 10% of the critical period and good enough for the initial tuning estimates.

Using the independent control form of the PID controller, the initial estimate of the proportional gain, k_p, will be 0.5 k_c. The initial integral term k_i, will be k_p/T_c. The equivalent integrator time constant will be T_c/k_p. In the example of Fig. 6.7, the critical gain is approximately 70, so the initial proportional gain k_p will be set at 35. The critical period T_c is approximately 25 seconds, so the initial integrator gain would be estimated at about 1.4, or the integrator time constant T_i would be about 0.71 seconds. Using the dependent form, the initial proportional gain will again be k_p, but the integral term will be $1/T_c$.

If the derivative term is used, its initial value can be estimated to be in the range $k_pT_c/8$. Note that if the system exhibits inversion, in which the system responds in the opposite direction to the desired control function, the use of derivative control should be avoided as fast changes in current due to noise response could destabilize the load.

6.4 Selecting the Optimal Servo

To select the most competent control system for the temperature stabilization of the protection box, we have tested the performance of both commercial analog servos and a home-built digital servo. The results are compared using the Allan deviation, which is a unitless measure intended to estimate stability due to noise processes.

6.4.1 Allan Deviation

By definition, the overlapping Allan deviation σ_y (which is a preferred estimation of the standard Allan deviation [56]) is calculated as a function of observation time τ by the following equation [57]:

$$\sigma_y^2(n\tau_0, N) = \frac{1}{2n^2\tau_0^2(N-2n)} \sum_{i=0}^{N-2n-1} (x_{i+2n} - 2x_{i+n} + x_i)^2 \tag{6.4}$$

where τ_0 is the sampling period, n is an integer multiplier of the sampling period that best estimates the desired $\tau \approx n\tau_0$, N is the number of data points, and x_i represents the i^{th} element in the time series. Let $\tau_0 = 1$ s, and let $n\tau_0 = n = \tau$, we have:

$$\sigma_y^2(\tau, N) = \frac{1}{2\tau^2(N-2\tau)} \sum_{i=0}^{N-2\tau-1} (x_{i+2\tau} - 2x_{i+\tau} + x_i)^2 \tag{6.5}$$

Note that Allan Deviation is displayed as a graph rather than a single number. A low Allan deviation is a characteristic of a system with good stability over the measured period. We will use this indicator multiple times in the following sections to compare the stability performances of different setups.

6.4.2 The HTC Analog Temperature Servo

We have chosen the Wavelength Electronics HTC series as the analog servos for our system. These servos employ a PI control-loop with independently adjustable proportional gain (P) and integral time constant (I). Based on the heat dissipation analysis in Section 6.2, we focus our attention on the HTC-3000 and HTC-4000 series, of which the compliance voltage is +11.25 V (with +12 V input), and the maximum output currents are 3 A and 4 A for HTC-3000 and HTC-4000, respectively. These output conditions meet the minimum power requirement of 28.56 W for 0.5 K ambient temperature fluctuation (see Table 6.2). As shown in Fig. 6.8 (b), the assembled servo device is made of a printed circuit board (dark), an evaluation board (green), and a home-built lego box (metal gray). We will skip details about the assembling process, which is well explained in Ref. [58], and will emphasize the configuration for our setup.

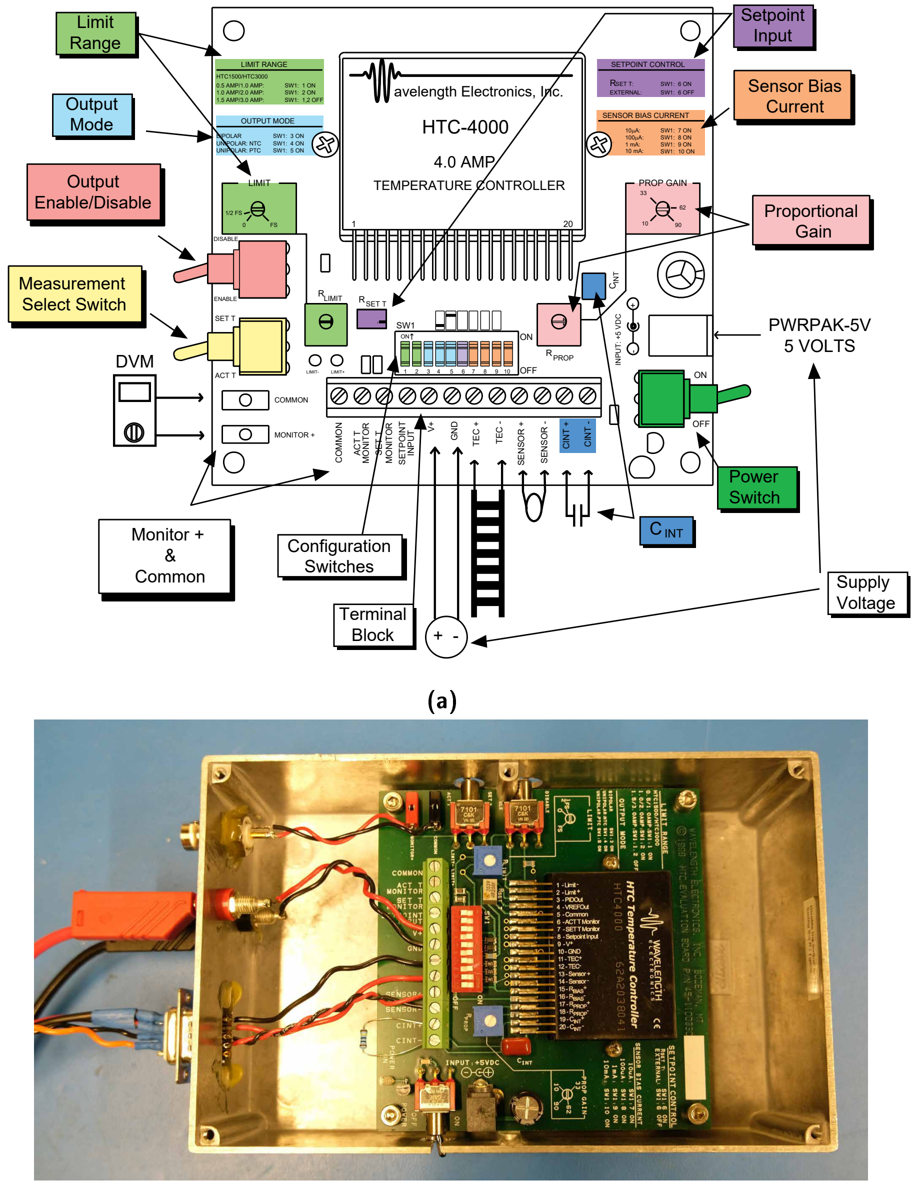

(a)

(b)

Figure 6.8 The Wavelength Electronics HTC analog servo. (a) Top view of the HTC evaluation board. (b) Assembled servo composed of a PCB (dark chip), an evaluation board (green plastic board), and a home-built lego box (gray metal box).

As shown in Fig. 6.8 (a), there is a series of trimpots and switches controlling the operating mode for the servo. Firstly, the Limit Range for the R-limit trimpot (top-left) is turned fully clockwise to allow full-scale current output. We will then configure the ten Configuration Switches (SW 1 to SW 10) on the bottom-middle part of the evaluation board. Switches SW 1 and SW 2 are responsible for setting the output current range and are both turned to the OFF position for the maximum range. The SW 3 to SW 5 switches take care of the output mode, and are set to be OFF (SW 3), ON (SW 4), and OFF (SW 5) for unipolar (heater) operation with our negative temperature coefficient (NTC) thermistor. Switch SW 6 determines how the setpoint is controlled, which for our case is positioned to be ON for use of the onboard $\mathrm{R_{SET-T}}$ setpoint trimpot. Switches SW 7 to SW 10 set the sensor bias current to a given level specified in Table 6.4.

BIAS CURRENT	SW1:7	SW1:8	SW1:9	SW1:10	RECOMMENDED FOR:
10 µA	ON	OFF	OFF	OFF	100 kΩ Thermistors
100 µA	OFF	ON	OFF	OFF	10 kΩ Thermistors
1 mA	OFF	OFF	ON	OFF	1 kΩ RTDs & LM335 IC Sensor
10 mA	OFF	OFF	OFF	ON	100 Ω RTDs
0 mA	OFF	OFF	OFF	OFF	AD590

Table 6.4 Switch configurations for setting the sensor bias current. Adapted from Ref. [58].

We are required to choose a bias current that leads to a sensor voltage between 0.25 V and ($\mathrm{V_{supply}}$ - 1.3 V). Since we are using a 10 kΩ thermistor, the switches are set to be OFF (SW 7), ON (SW 8), OFF (SW 9), and OFF (SW 10) for a 100 μA bias current leading to a sensor voltage of 1 V.

After having configured the servo, we are now ready to tune the PI parameters for an optimized servo performance. The proportional gain can be adjusted by turning the $\mathrm{R_{PROP}}$ trimpot between a gain of 10 and 90. For the integration time constant, a 1 μF capacitor is mounted internally to yield a default one second integrator time constant. By adding capacitance across the CINT+ and CINT- input ports on the Terminal Block, we can increase the integrator time constant to any value below 10 seconds according to the relation:

$$\mathrm{T_{INT}} = \mathrm{C_{INT}} \cdot 1\mathrm{M}\Omega, \tag{6.6}$$

where $\mathrm{T_{INT}}$ is the integration time and $\mathrm{C_{INT}}$ is the added capacitance. To disable the integral gain, we can instead add a 1 MΩ resistor across the two input ports. Note that before turning on the servo, we should make sure that the supply voltage and current follow the Safe Operating Area (SOA) presented in Ref. [58]. The SOA is determined by the amount of power that can be dissipated within the output stage of the controller. If that power limit is exceeded, permanent damage can result.

Following the instructions in Section 6.3.3, we disable the integration and tune the P gain to observe an oscillation at the critical period shown in Fig. 6.9. As a sizeable thermal mass, the protection box exhibits a critical period on the order of 10-minute, which is orders-of-magnitude larger than the 10-second integration limit of the analog servo. Note that for an analog device, the integration time range is constrained to the performance of the internal operational amplifiers (Op-amps) and is in general hard to resolve a T_i on the order of tens of minutes (the corresponding integral gain is too small for the electronics). Additionally, the critical integration time for the protection box can also not be easily reduced by orders-of-magnitude, as it would require a power supply far exceeding the power of the standard laboratory power supplies. In this case, we decide to proceed without the integral control since otherwise it would lead to too much overshoots and a prolonged settling time, which is described in Table 6.3.

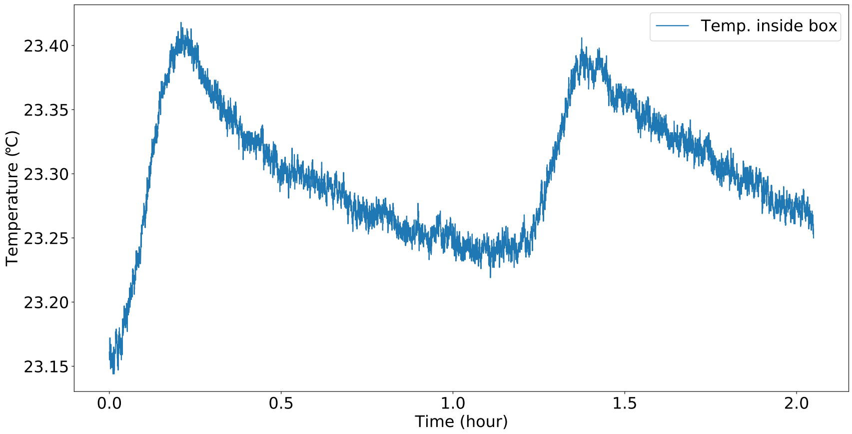

Figure 6.9 Critical oscillation for the Ziegler-Nichols method using the Analog HTC servo.

As mentioned before, with only the proportional control the system cannot fully reach the setpoint. It is, however, not a problem for our case as long as the system is well stabilized to a reasonable steady-state temperature, which is the most important goal for us. Additionally, it is also possible to set the system to a specific temperature by setting the setpoint temperature a bit higher to compensate for the finite steady-state error.

The next decision we need to make is about where to attach the thermistor. Previously, the group has been attaching the thermistor directly onto the cavity steel chamber at the center of the protection box. However, this position may not be the optimal point, as it increases the thermal path between the sensor and the temperature adjustment elements (heaters) on the inner sidewalls. This extended thermal path is expected to lead to a delayed feedback and makes the system more oscillatory and less stable.

To experimentally determine the optimal configuration, three set-ups are tested: double servos (HTC 3000 + HTC 4000) with sensors attached to the cavity and to the sidewalls, and single servo (HTC 4000) with sensor attached to the sidewall. The voltage setpoint is chosen to be 1.055 V, which is about 3 degrees higher than the room temperature. For practical reasons, all the tuning processes presented take place in the preparatory lab

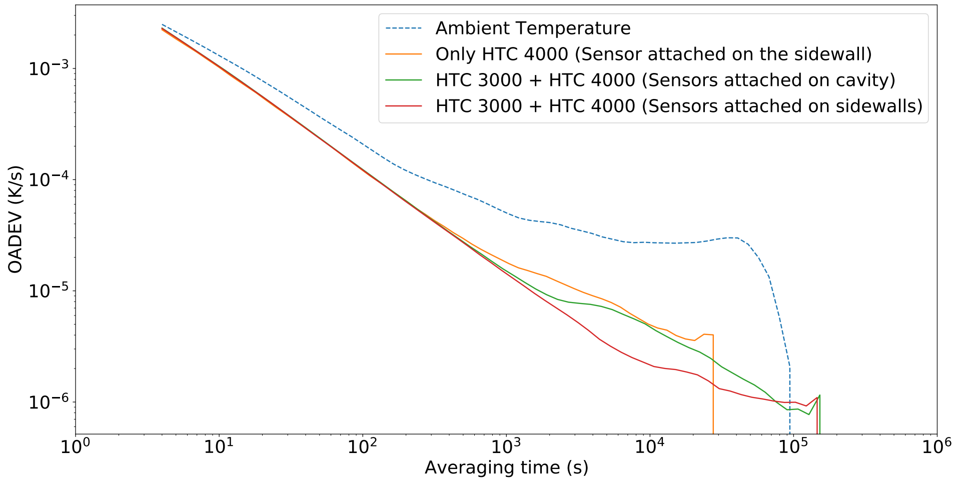

Figure 6.10 OADEV calculations for different temperature stabilization configurations using analog servos.

(prep lab) instead of the main lab optical table, with an old cavity placed in the center of the box resembling the thermal mass of the actual cavity for the experiment. The temperature is monitored using a thermal coupler attached to the top of the cavity inside the box. The calculated overlapping Allan deviations are presented in Fig. 6.10. As we can see, the sensor-on-sidewall case (red) exhibits a lower overlapping Allan deviation than the sensor-on-cavity case (green) as predicted. Additionally, the double-servo cases are more effective than the single-servo case (orange).

Finally we present the actual temperature stabilization data with two HTC analog servos in Fig. 6.11. As we can see, the cavity temperature can be stabilized within 0.1 K under an ambient temperature fluctuation of about 0.5 K to 1 K. Note that the ambient temperature instability in the prep lab is larger than the 0.5 K temperature fluctuation for the main lab optical table. It is thus expected that the actual performance of the temperature stabilization system should be even better during the experiment.

6.4.3 The Home-built Digital Temperature Servo

Due to the internal limitation of the analog servos, the temperature stabilization results presented above are solely from a Proportional control loop. As a possible alternative, a home-built digital servo using the Arduino (Leonardo) module is constructed and tested, through which we are free to implement a full PI control loop. The actual setup of the Arduino module is presented in Fig. 6.12.

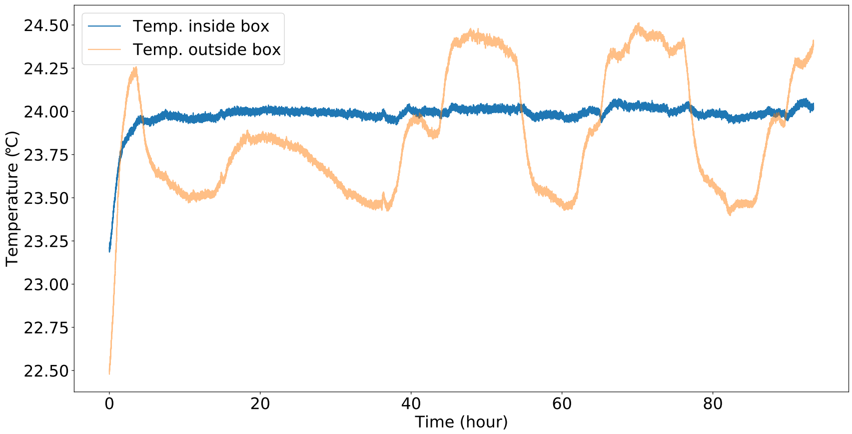

Figure 6.11 Temperature stabilization with the HTC 3000 and HTC 4000 analog servos. The cavity temperature can be stabilized within 0.1 K under an ambient temperature fluctuation of about 0.5 K to 1 K.

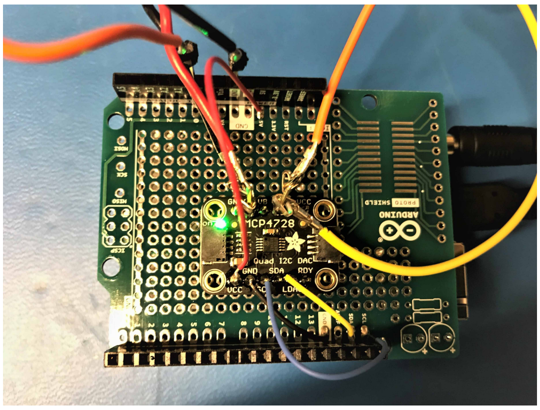

Figure 6.12 The home-built digital temperature servo using the Arduino Leonardo module.

For the digital servo setup, the voltage readout of the thermistor is sent into the Arduino board which compares it with a setpoint value to generate an error value. The error value is processed digitally through a programmed PI loop (independent form). The digital output of the PI loop is then converted to an analog signal via a digital to analog converter (Adafruit MCP4728) and is sent into an externally controllable laboratory power supply (EA-PS 3032-10 B). The power supply is directly connected to the heaters and are able to provide a current from 0 A to 10 A at a fixed voltage below 32 V. The actual code for the Arduino module is attached in Appendix A.

Following the instructions in Section 6.3.3, we obtain a critical proportional gain at 400,000 with a critical period of 5.6 minutes, which is shown in Fig. 6.13. After a se-

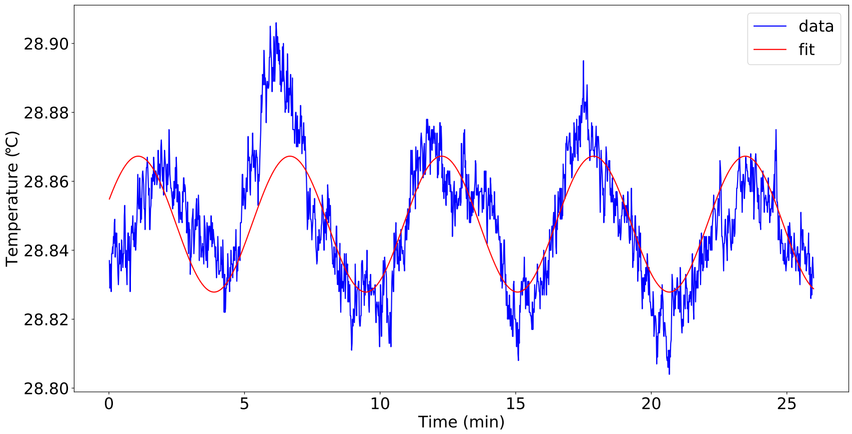

Figure 6.13 Critical oscillation for the Ziegler-Nichols method using the home-built digital servo.

ries of fine-tuning based on Section 6.3.2, we obtain an optimal set of parameters with $k_p = 180000$ and $k_i = 0.6$. The temperature stabilization data is presented in Fig. 6.14 (a). For a 1 K ambient temperature fluctuation, the digital servo is able to maintain a maximum temperature fluctuation within 0.15 K. For better knowledge of the stability, the overlapping Allan deviation is calculated and compared with that of the double-analog-servo configuration. The result is presented in Fig. 6.14 (b). From the Allan deviation analysis, we observe a lower curve for the analog servo case which demonstrates a stronger temperature stabilization ability. One possible explanation is that with the purely Proportional control case, since there always exits a steady-state error, the heaters are always running, and in this case the system is symmetric in its heating (more heating) and “cooling” (less heating) capacities around the steady-state value. However, with the PI loop implemented in the digital servo, heaters stop running once the set temperature is reached, and, since there is no active cooling device, the system is asymmetric in its heating (with heaters) and cooling (passive dissipation of heat) capacities around the set value. This asymmetry could possibly be the cause for more instability in the digital case. Further experiments can be conducted by removing the Integration control from the digital servo and compare with the PI case to test this conjecture.

Fairly speaking, as a first-stage temperature adjustment device, both the commercial analog servo and the home-built digital servo demonstrate sufficient ability in reducing a rough environmental temperature fluctuation by one order of magnitude, which significantly lowers the working load for the second-stage temperature tuning device inside the cavity, serving as an extra warranty for achieving the ultralow 1 mK cavity temperature instability.

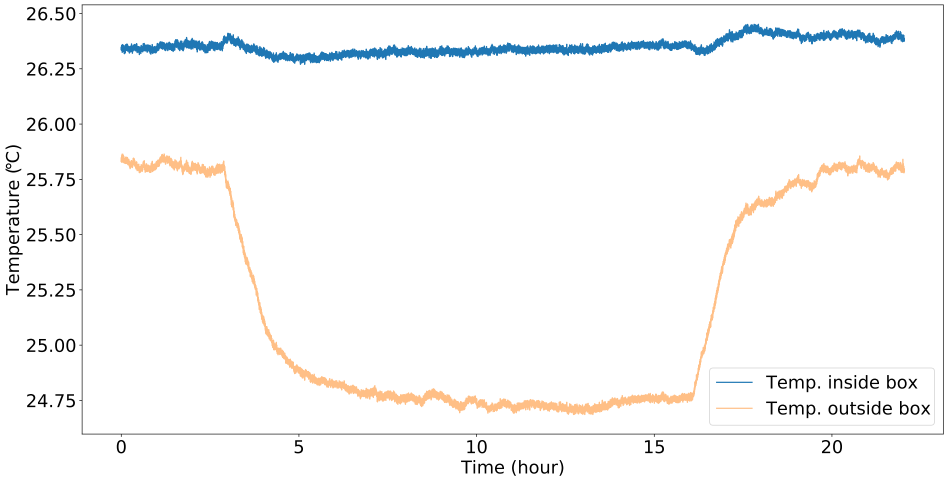

(a)

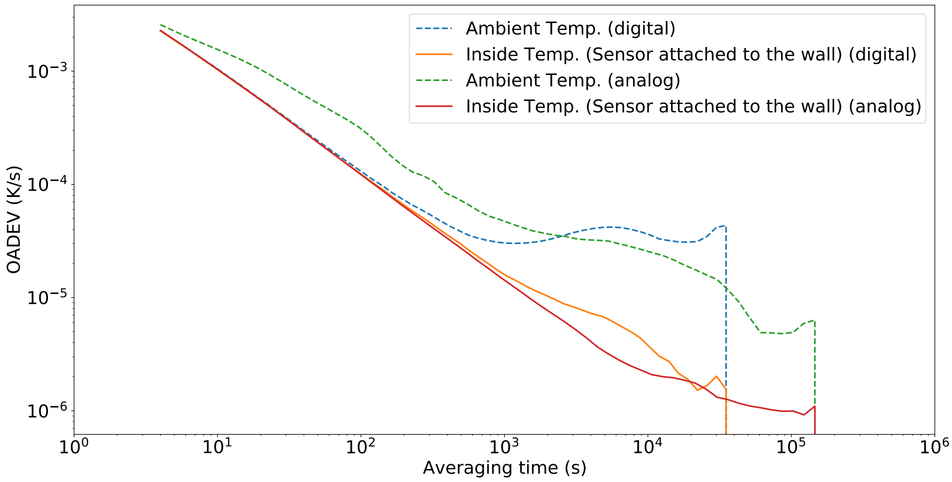

(b)

Figure 6.14 Performance of the digital temperature servo. (a) Temperature stabilization using the digital servo. (b) Comparison of the overlapping Allan deviation between the digital servo and the double-analog-servo configuration.

6.4.4 Outlook

Even though we have achieved a reasonably good temperature stabilization for the protection box, there are still a few things we could do to make the system even more robust. As for now five of the six faces around the cavity are nicely covered and temperature stabilized; the bottom face, however, is left open and behaves as an uncompensated channel for heat transfer. One possible solution to alleviate this situation is to provide better shielding for the bottom and/or put extra heaters on the bottom breadboard. Additionally, since the protection box behaves as a massive thermal load, we are more or less limited by our present level of heating power. Even though it is practically challenging to boost the input power by several orders of magnitudes, it may still be possible to switch to more powerful servos or more powerful power supplies for more robust performances. (Note that we do not have to worry about over-driving the Kapton heaters, which are far from reaching the 50 W maximum power output.)

Chapter 7

Phase Noise in Optical Fibers

ONCE we have obtained a laser light frequency-stabilized to the ultrastable reference cavity, we can proceed to direct it to the atoms via optical fibers. A problem, however, occurs during this transmission process, as the light beam is subject to a fiber-induced phase noise which causes short-term, random fluctuations that significantly brings down the performance of a super-narrow laser system. According to Ref. [59], such a fiber phase noise in a normal laboratory setup can increase the frequency uncertainty to approximately 1 kHz for a laser with frequency uncertainty on the Hz level. In this Chapter, we will focus on the mechanisms inducing the phase noise in optical fibers, and present a simulation of the power spectral density of the phase noise in our experimental setup. The simulation provides us valuable insights in which part of the noise spectrum we should focus on when designing an active noise-cancellation system, which will be discussed in the next Chapter. The theoretical framework used in this Chapter is mainly adapted from Ref. [60].

7.1 Mechanisms behind Fiber Phase Noise

As summarized in Ref. [60], there are three spontaneous processes that can cause the phase of light traveling through a fiber to fluctuate. The first process is caused by the random extension and contraction of the fiber length due to local temperature fluctuations and is called spontaneous thermal expansion (STE). The second process is due to random variations in the refractive index induced by fluctuations of the local temperature and is referred to as spontaneous thermo-optic (STO) effects. Because of their common origins, STE and STO can be further categorized as thermoconductive effects. The third process originates from mechanical effects which lead to random stretches of the fiber length.

The overall fiber-induced phase noise imprinted on the transmitted laser light is thus equal to the sum of the contributions from the aforementioned three processes [60]:

$$S_\phi(\omega) = \frac{4\pi^2}{\lambda^2}\left[\left(\frac{\mathrm{d}n}{\mathrm{d}T} + n\alpha_L\right)^2 l^2 S_{\delta\mathrm{T}}(\omega) + n^2 S_l(\omega)\right], \tag{7.1}$$

where ω is the angular frequency, $S_\phi(\omega)$, $S_{\delta \mathrm{T}}(\omega)$, and $S_l(\omega)$ are the power spectral densities of the overall phase noise, the local temperature fluctuation, and the fiber length fluctuation, respectively, λ is the laser wavelength in vacuum, l is the nominal length of the fiber, n is the refractive index, α_L is the linear expansion coefficient, and T is temperature. The two terms inside the parentheses on the right-hand-side correspond to STO and STE, respectively, and the third term is due to mechanical effects.

7.2 Fluctuation-dissipation Theorem

Now, to simulate the overall phase noise, we will just have to calculate the power spectral densities in local temperature and fiber length. Such a calculation involves the use of the fluctuation-dissipation theorem (FDT), which, as a universal framework, relates fluctuations to processes that dissipate energy. According to [61], the general expression for the FDT can be written as:

$$S_\xi(\omega) = \frac{k_B T}{\pi \omega^2} \mathrm{Re}[Y_\xi(\omega)], \tag{7.2}$$

where $S_\xi(\omega)$ is the spectral density of the spontaneous fluctuations of an extensive parameter ξ of the system, $Y_\xi(\omega)$ is the admittance function associated with ξ, and k_B is the Boltzmann constant. The FDT allows one to find $S_\xi(\omega)$ through the real part of $Y_\xi(\omega)$, which is the loss of the system under a harmonic external excitation at the frequency ω. This external excitation, denoted as $\tilde{F}(\omega)$, is a Fourier component of a generalized force $F(t)$. The admittance function is related to $\tilde{F}(\omega)$ through [61]

$$Y_\xi(\omega) = \left(\frac{\tilde{F}(\omega)}{i\omega \tilde{\xi}(\omega)} \right)^{-1}, \tag{7.3}$$

where $\tilde{\xi}(\omega)$ is the Fourier component of ξ at the frequency ω under the excitation of $\tilde{F}(\omega)$. Through the above discussions, the following steps must be taken when applying FDT to analyze the spontaneous fluctuations of a general variable ξ: (a) identify the generalized force F corresponding to ξ, (b) find the admittance function $Y_\xi(\omega)$ and its real part, and (c) find the spectral density of ξ directly through Eqn. 7.2.

7.3 Simulation of the Fiber Phase Noise

7.3.1 Spectral Density for Temperature Fluctuation

To find the admittance function for temperature fluctuations, we employ a scheme outlined in Ref. [62] and Ref. [63] that relates the real part of the admittance function to the energy dissipation under a harmonic perturbation with the general form $F_0 \cos(\omega t) f(\overrightarrow{r})$, where F_0 characterizes the amplitude of the external force and $f(\overrightarrow{r})$ is a form factor for the spatial distribution of the perturbation. The admittance function is related to the energy dissipation W_{diss} of the system under the external driving by [60]

$$|\text{Re}[Y_\xi(\omega)]| = \frac{2W_{\text{diss}}}{F_0^2}. \tag{7.4}$$

Plugging Eqn. 7.4 into Eqn. 7.2 we obtain

$$S_\xi(\omega) = \frac{2k_B T}{\pi\omega^2} \frac{W_{\text{diss}}}{F_0^2}. \tag{7.5}$$

Now, as illustrated in Fig. 7.2, we consider a section of single-mode fiber with a laser beam propagating through it. At the end of the fiber, there is a phase detector to probe the phase of the light. Given that the laser beam samples local fluctuations of the fiber throughout its path and the detected phase noise is weighted by the Gaussian power profile of the fiber mode, it is reasonable to employ a form factor $f(\overrightarrow{r})$ matching the laser beam profile.

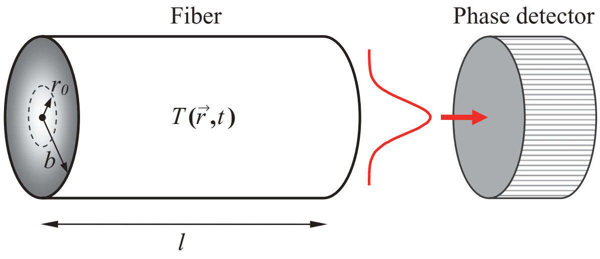

Figure 7.1 A conceptual model for laser beam traveling through a section of an optical fiber subject to temperature fluctuations. The phase of the light is monitored by a phase detector at the end of the fiber. Adapted from Ref. [60].

The fiber can be treated as a straight cylindrical rod extending along z axis of a cylindrical coordinate, since as long as it is not sharply bent, the laser mode is symmetrical around the optical axis and uniform along the fiber. The external generalized force here is in the unit of entropy. The injected entropy creates heat that changes the temperature field inside the fiber through thermal conduction. The volumetric density of the injected entropy at time t and radial location r from the optical axis can be expressed as [60]

$$\delta \mathrm{S}(r,t) = \frac{F_0}{\pi r_0^2} e^{-r^2/r_0^2} e^{-i\omega t}, \tag{7.6}$$

where r_0 is the effective radius of the Gaussian power profile and l is the fiber length, as shown in Fig. 7.2. Assuming that the fiber is in thermal equilibrium at temperature T before the perturbation, and following the general theory of thermal conduction [64], the equation for temperature variations can be written as

$$\kappa \nabla^2 \delta \mathrm{T} - C_V \frac{\partial \delta \mathrm{T}}{\partial t} = T \frac{\partial \delta \mathrm{S}}{\partial t}, \tag{7.7}$$

where $\delta \mathrm{T}(\boldsymbol{r}, t)$ is the variation in the temperature field induced by the external perturbation, κ is the thermal conductivity, and C_V is the volumetric heat capacity. Substituting Eqn. 7.6 into Eqn. 7.7, and using the Green's function method [65], we can obtain the solution for $\delta \mathrm{T}(r,t)$ as [60]

$$\delta \mathrm{T}(r,t) = \frac{i\omega F_0 T}{4\pi l \kappa} e^{-i(\omega t + \psi_0)} \int_1^\infty \exp\left(i\psi_0 \zeta - \frac{r^2}{r_0^2 \zeta} \right) \frac{\mathrm{d}\zeta}{\zeta}, \tag{7.8}$$

where $\psi_0 \equiv \omega r_0^2/(4D)$, with diffusivity $D \equiv \kappa / C_V$, and $\zeta = 1 + 4Dt/r_0^2$.

The temperature variations $\delta \mathrm{T}(r,t)$ along the radial direction break the thermal equilibrium, and as the system tries to "relax" back, heat flow is generated. This relaxation process via thermal conduction causes energy dissipation, which, according to the theory of thermal conduction, can be expressed as [66]

$$\mathrm{W}_{\mathrm{diss}} = \int \frac{\kappa}{T} \left\langle (\nabla \delta \mathrm{T})^2 \right\rangle \mathrm{d}V = \frac{\kappa}{2T} \int \nabla \delta \mathrm{T} \cdot \nabla \delta \mathrm{T}^* \mathrm{d}V, \tag{7.9}$$

where $*$ represents the complex conjugate and the volumetric integration is over the entire fiber. By substituting Eqn. 7.8 into Eqn. 7.9, and evaluate the integral, we can finally obtain an expression for the power dissipation [60]:

$$\mathrm{W}_{\mathrm{diss}} = \frac{\omega^2 F_0^2 T}{8\pi l \kappa} \mathrm{Re}\left[e^{2i\psi_0} E_1(2i\psi_0) \right], \tag{7.10}$$

where E_1 is the special function of the exponential integral [67]. Now, simply plugging Eqn. 7.10 into Eqn. 7.5, we find the spectral density of the spontaneous temperature fluctuation in the fiber to be:

$$S_{\delta \mathrm{T}}(\omega) = \frac{k_B T^2}{4\pi^2 l \kappa} \mathrm{Re} \left[\exp\left(\frac{i\omega r_0^2}{2D} \right) E_1 \left(\frac{i\omega r_0^2}{2D} \right) \right]. \tag{7.11}$$

7.3.2 Spectral Density for Fiber Length Fluctuation

The spontaneous reshaping of the fiber due to mechanical damping can, in principle, be analyzed via normal mode expansion [68]. Each normal mode can be treated as a mechanical oscillator and the total spectral density is the sum of the contributions from all the individual modes. Each mechanical oscillator satisfies the generalized Hooke's law, $F_r = -k[1 + i\phi(\omega)]x$, where F_r is the restoring force, x is the displacement, k is the ideal spring constant, and $\phi(\omega)$ is the loss angle given by $\phi = \Delta\omega/(1 + \omega^2\tau^2)$, where Δ is the relaxation strength, and τ is the relaxation time [69]. Simply substituting the Fourier component of this force into Eqn. 7.3, we derive the admittance function for a single oscillator [60]:

$$Y_x(\omega) = \frac{\omega k \phi(\omega) + i(\omega k - m\omega^3)}{(k - m\omega^2)^2 + k^2\phi^2(\omega)}, \tag{7.12}$$

where m is mass. Plugging the real part of Eqn. 7.12 into Eqn. 7.2, we obtain the fluctuation spectral density for a single harmonic oscillator as [60]

$$S_x(\omega) = \frac{k_B T \omega_0^2 \phi(\omega)}{\pi \omega m[(\omega^2 - \omega_0^2)^2 + \omega_0^4 \phi^2(\omega)]}, \tag{7.13}$$

where $\omega_0^2 \equiv k/m$ is the angular resonant frequency of the oscillator. Summing all the individual modes, we can write the total spectral density for length fluctuation as

$$S_l(\omega) = \frac{k_B T}{\pi \omega} \sum_N \frac{\omega_N^2 \phi_N(\omega)}{m_N[(\omega^2 - \omega_N^2)^2 + \omega_N^4 \phi_N^2(\omega)]}, \tag{7.14}$$

where ω_N, m_N, and $\phi_N(\omega)$ are the angular frequency, effective mass, and loss angle associated to the Nth mode, respectively. For length fluctuations, the fiber can be further simplified to a 1D system so that only the longitudinal vibration modes are involved [70]. Following the same physical picture for the fiber in Fig. 7.2, we can write the longitudinal elastic wave equation as [64]

$$\frac{\partial^2 u_z}{\partial z^2} - \frac{\rho}{E_0}\frac{\partial^2 u_z}{\partial t^2} = 0, \tag{7.15}$$

where u_z is longitudinal displacement, ρ is the fiber density, and E_0 is the Young's modulus without loss. Under the boundary conditions of two free ends at $z = 0$ and $z = l$, the Nth vibration mode is given by [60] $u_{\mathrm{zN}}(z,t) = \Omega_N(z)e^{-i\Omega_N t}$, where $\Omega_N(z) = \cos(N\pi z/l)$ and $\omega_N = (n\pi/l)\sqrt{E_0/\rho}$. The effective mass for the Nth mode is given by [60] $m_N = \rho A l/2$, where A is the cross-sectional area. Substituting ω_N and m_N into Eqn. 7.14, and treating the loss angle as approximately frequency independent over the entire spectral range of interest [71], the spectral density of fiber length fluctuations is simplified to [60]

$$S_l(\omega) = \frac{2k_B T l \phi_0}{\pi^3 A E_0 \omega}\sum_N \frac{1}{N^2[(1-\omega^2/\omega_N^2)^2+\phi_0^2]}. \tag{7.16}$$

The numerical computation of $S_l(\omega)$ requires an upper limit on the summation. We can find a reasonable cutoff order by looking at the contribution of each order to the overall noise power, which can be performed by integrating each order in Eqn. 7.16 over the entire frequency span. Figure 7.2 shows how the total noise power, normalized to the power of the first order, changes against the cutoff order. Evidently, the higher modes beyond $N = 10$ makes only a small difference in the total noise power.

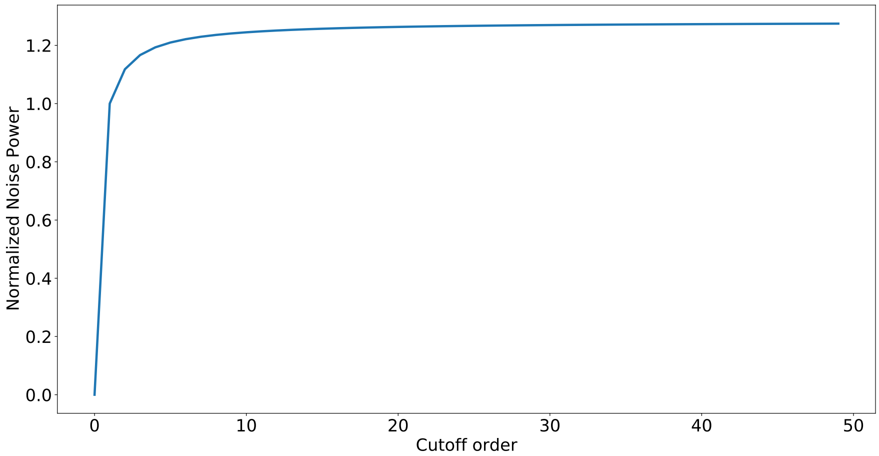

Figure 7.2 Effect of the cutoff order on the total noise power.

7.3.3 Simulation Results

Once we obtain the spectral densities of the temperature and length fluctuations, it is straightforward to calculate the overall phase noise spectral density $S_\phi(\omega)$ by substituting $S_{\delta\mathrm{T}}(\omega)$ from Eqn. 7.11 and $S_l(\omega)$ from Eqn. 7.16 into Eqn. 7.1. We carry out the fiber noise simulation for a 3-m-long Thorlabs PM630-HP single-mode fiber operating at 671 nm under a temperature of 295 K. The mode field diameter for the fiber is 2.75 $\mu\mathrm{m}$ with a fiber outer radius of $b = 122.5$ $\mu\mathrm{m}$ according to the datasheet [72]. The following optical and thermal properties of silica are used [73]: $n = 1.457$, $\mathrm{d}n/\mathrm{d}T = 9.488 \cdot 10^{-6}$ K^{-1}, $\alpha_L = 5.0 \cdot 10^{-7}$ K^{-1}, $\kappa = 1.37$ $\mathrm{Wm}^{-1}\mathrm{K}^{-1}$, and $D = 0.82 \cdot 10^{-6}$ m^2/s. We use an averaged fiber density of $\rho = 1430$ kg/m^3 [74], and a measured Young's modulus of $E_0 \approx 68$ GPa [75]. The mechanical noise is calculated following the assumption in Ref. [60] that the loss angle ϕ_0 equals 0.01 across the entire frequency span.

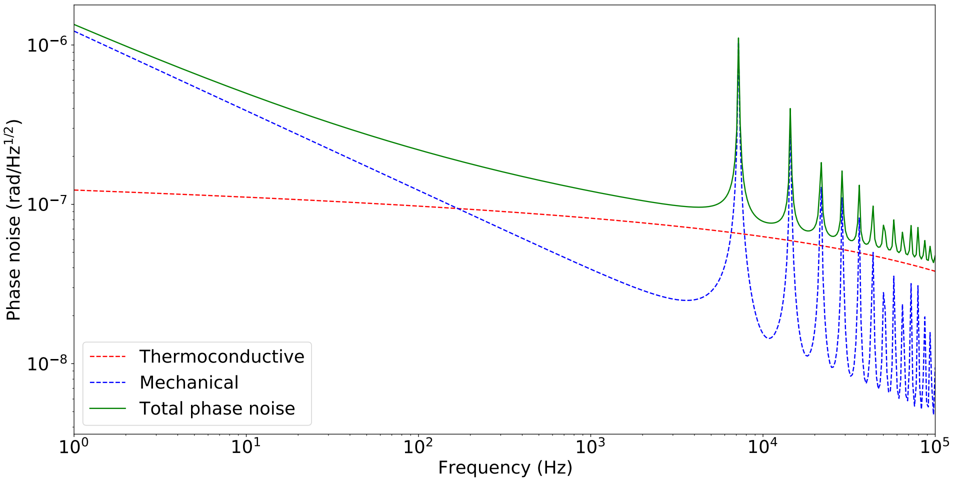

Figure 7.3 The simulated phase noise spectra for a 3-m-long Thorlabs PM-630-HP optical fiber used in our experiment. The red curve represents the thermoconductive noise, the blue curve represents the mechanical noise, and the green curve represents the total phase noise.

Figure 7.3 shows the simulated phase noise spectra of the thermoconductive noise (red), the mechanical noise (blue), and the total phase noise (green). The thermoconductive noise dominates the total noise at high frequencies above 1 kHz, whereas the mechanical noise prevails at low frequencies below 100 Hz. Note that we do not have to worry about the strong mechanical resonance peaks shown in Fig. 7.3. These peaks only exist in the theoretical case of a perfectly uniform, straight fiber, and have never been observed in reality [71], as any bending and material non-uniformity due to manufacturing would eliminate them. The simulation using FDT is able to provide a solid understanding of the noise properties for our fiber. One very important insight from this simulation is that the fiber phase noise mainly concentrates in the low-frequency region below a few hundred Hz. Efforts for fiber noise cancellation should thus be focused on the lower end of the noise spectrum. Additionally, we do not need to worry too much about the high-frequency noise above several kHz, as they are significantly weaker than the low-frequency noises.

Chapter 8

Active Cancellation of the Fiber Phase Noise

After having understood the mechanisms behind the phase noise in optical fibers, we will proceed to discuss the actual cancellation process of the fiber phase noise. Before delving into the details of the complex experimental setup, let us first take a look at the principles behind the major steps involved in the cancellation process.

8.1 Working Principles of the Fiber Noise Cancellation System

We will start by introducing the two most important elements involved in a fiber noise cancellation (FNC) system: phase detection and phase correction. Then we will discuss how to use a phase-locked loop to incorporate these two elements for the actual realization of our FNC system.

8.1.1 Detection of the Phase Noise

Direct measurement of the phase properties of our laser light is unrealistic, as the frequency of the laser is on the order of several hundred THz (red light), far beyond the bandwidth of any existing photodetectors. However, we can probe the phase properties of the light indirectly. A simplified model is illustrated in Fig. 8.1, where we split a laser beam with frequency ω into two arms: Path 1 is frequency-shifted by $+f$, and Path 2 is frequency-shifted by $-f$ and travels through an optical fiber picking up a relative phase $\phi(t)$. At this point, the electric field of Path 1 can be written as $E_1(t) = E_a \cos[(\omega + f)t]$ and the electric field of Path 2 is $E_2(t) = E_b \cos[(\omega - f)t + \phi(t)]$, where E_a and E_b are the field amplitudes for Path 1 and Path 2, respectively. The two arms are superimposed and measured by a photodetector. Ignoring terms oscillating on the order of ω which are too fast to be resolved by the photodetector, the actual signal from the photodetector is the following:

$$|E_1(t) + E_2(t)|^2 \propto \frac{E_a^2}{2} + \frac{E_b^2}{2} + E_a E_b \cos[2ft - \phi(t)]. \tag{8.1}$$

The next step is to mix this signal with a local oscillator at frequency $2f$ through a mixer. Remember that the mixer basically multiplies the two input signals. If we assume that the local oscillator is exactly in phase with the original laser light, we can write the local oscillator's signal as $E_o \cos(2ft)$, where E_0 is the oscillating amplitude, and the signal output from the IF port of the mixer becomes:

$$P_{\mathrm{IF}} = \frac{E_a^2 E_o}{2} \cos(2ft) + \frac{E_b^2 E_o}{2} \cos(2ft) + \frac{E_a E_b E_o}{2} \cos[4ft - \phi(t)] + \frac{E_a E_b E_o}{2} \cos[\phi(t)]. \tag{8.2}$$

Finally, we use a low-pass filter with corner frequency below $2f$ to get rid of the oscillating terms in Eqn. 8.2. Consequently, we obtain information of the fiber phase noise $\phi(t)$ from the DC signal proportional to $\cos[\phi(t)]$. Note that it is crucial to have the local oscillator oscillating exactly at $2f$ and in phase with the original light. These two requirements are fulfilled by implementing a phase-locked loop that will be introduced later in this Chapter.

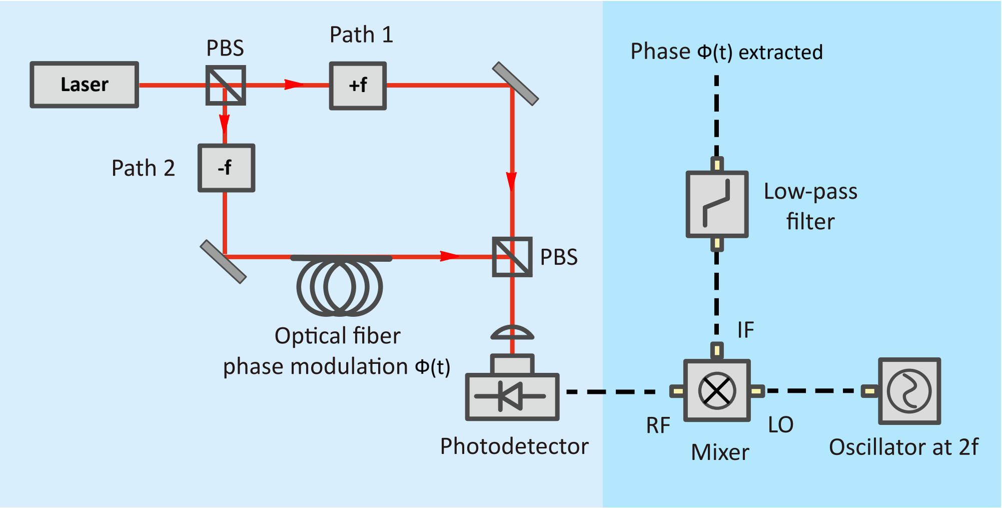

Figure 8.1 Extraction of fiber phase noise. In the optical setup (light blue shaded), laser light is split into two arms. Path 1 is frequency-shifted by $+f$ and Path 2 is frequency-shifted by $-f$ as well as phase-modulated by $\phi(t)$ via an optical fiber. The two arms are combined and measured at the photodetector. In the electronic setup (deep blue shaded), the photodetector signal is mixed with a local oscillator at $2f$. The output from the mixer is low-passed to yield a DC term proportional to the phase noise $\phi(t)$ from the fiber.

8.1.2 Correction of the Phase Noise

Another important step is to correct the phase of the light. For our setup, we employ an AOM for phase correction. We have briefly mentioned these devices when introducing the setup of the double-pass AOM in Chapter 3, and now let us take a closer look. An AOM uses acousto-optic effect to shift the frequency of light using sound waves at radio-frequency. The acoustic wave changes the local refractive index of the material, and the incoming light scatters off the resulting periodic refractive index modulation, leading to different diffraction orders. Such a process is illustrated in Fig. 8.2, which shows that a light at frequency $f_{\rm in}$ is being diffracted by an acoustic wave at $f_{\rm RF}$ into +1st and -1st orders with frequencies $f_{\rm in} + f_{\rm RF}$ and $f_{\rm in} - f_{\rm RF}$, respectively. (There will also be higher diffraction orders with frequency shifts at integer multiples of $f_{\rm RF}$, which are irrelevant to our application.) By changing the frequency of the acoustic wave, we can modulate the diffracted frequencies of the laser light.

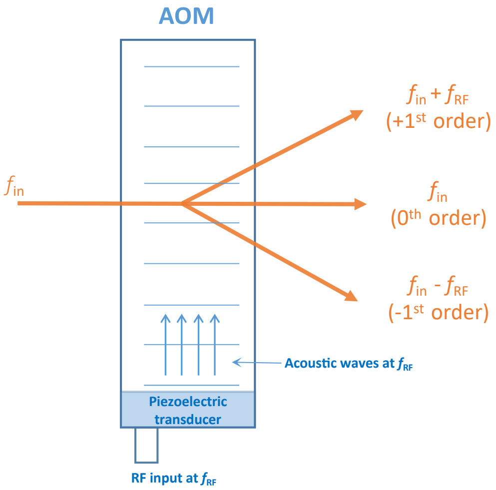

Figure 8.2 Conceptual illustration of an AOM. An electric RF signal is input into the piezoelectric transducer to generate acoustic waves at frequency $f_{\rm RF}$. Consequently, the incoming light with frequency $f_{\rm in}$ is diffracted into several diffraction orders. The positive orders are on the same side as the acoustic wave propagation direction and the negative orders are on the opposite side. The light frequency is shifted by $+f_{RF}$ and $-f_{RF}$ for the +1st and -1st orders, respective. Drawn with reference to Ref. [76].

At this point, one may wonder why we use a frequency modulator to correct for the phase noise. Actually, such a correction is feasible because phase noise is just the short-term instability of frequency and can be compensated via rapid minor changes of the light frequency. Moreover, recall that the phase detection scheme introduced in the previous Section requires frequency shifts of $\pm f$ for the two light paths. The AOM employed for phase correction can thus be used for generating the frequency shifts.

8.1.3 A Phase-locked Loop for Fiber Noise Cancellation

After having discussed the two major steps involved in the FNC process, we will now integrate them into a phase-locked loop to form the complete system. The idea presented in this Section is developed from a FNC scheme in Ref. [59].

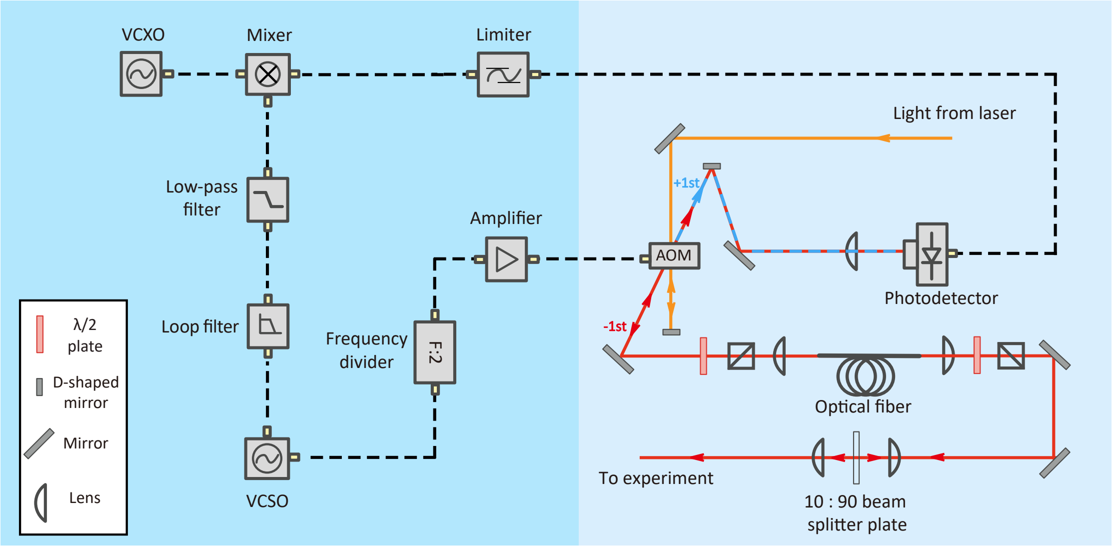

Figure 8.3 Schematic representation of the FNC system. In the optical part (shallow blue shaded) of the FNC system, laser light is diffracted by an AOM. The -1st order diffracted light picks up the fiber phase noise and is superimposed with the +1st order diffracted light on a photodetector. In the electronic part (deep blue shaded) of the FNC system, signal received from the photodetector is first sent through a limiter to reduce amplitude variations, and is then mixed with a VCXO that provides a stable reference frequency. The output of the mixer is low-passed to yield a DC signal proportional to the sum of the AOM phase and the fiber phase. This DC signal then serves as the error value to a loop filter, which drives a VCSO. The output of the VCSO is frequency-divided, amplified, and sent into the AOM to form a closed feedback loop. The FNC system, once activated, will minimize the error value by matching the AOM phase with the opposite of the fiber-induced phase, thus canceling the fiber phase noise.

A schematic representation of the entire FNC system is shown in Fig. 8.3. The system is composed of optical (shallow blue) and electrical (deep blue) parts. For the optical part, a laser light with electric field $E_0 \cos(\omega t)$ passes through an AOM driven by an RF signal with frequency f and phase $\phi_{\mathrm{AOM}}(t)$. The zeroth order of the transmitted light is reflected back and passes the AOM again, and the $+1$st order diffracted light (blue line) from this second passage has the electric field $E_0 \cos[(\omega + f)t - \phi_{\mathrm{AOM}}(t)]$ and is directed into a photodetector, resembling Path 1 in the phase detection scheme from Fig. 8.1. The -1st diffraction order of the light from the first passage of the AOM (red line), resembling Path 2 in Fig. 8.1, travels through the optical fiber picking up a phase noise of $\phi(t)$, and incidents on a beam splitter plate. The majority of the light is directed into the experiment, and a small portion of the light is reflected and travels the same path back, picks up again the fiber phase noise $\phi(t)$, and passes through the AOM. The zeroth order light from this second passage has the electric field $E_0 \cos[(\omega - f)t + \phi_{\mathrm{AOM}}(t) + 2\phi(t)]$ and is directed into the same photodetector. The signal received by the photodetector can be written as $E_0 \cos[2ft + 2\phi_{\mathrm{AOM}}(t) + 2\phi(t)]$, and is sent into the electronic part of the FNC system.

In the electronic part, the signal first passes a limiter, which helps determining the phase more precisely by transferring an incoming oscillating signal into a constant-amplitude signal with the same phase properties. The signal after the limiter is then sent into a mixer to mix with a reference oscillator. The reference oscillator here is a voltage controlled crystal oscillator (VCXO) that can provide a stable frequency fixed at $2f$. The output signal from the mixer has, according to Eqn. 8.2, a DC term proportional to the phase information $\cos[2\phi_{\mathrm{AOM}}(t) + 2\phi(t)]$ with AC terms at frequencies $2f$ and $4f$. Only the DC signal preserves after traveling through a low-pass filter, and is sent into a loop filter as the error term. The loop filter is composed of P, I, and D elements as introduced in Sec. 6.3.1 with different gains for various frequencies. We will discuss more details about the loop filter later in this Chapter. The output of the loop filter modulates a Voltage Controlled SAW Oscillator (VCSO) that has a frequency centered at $2f$ but could be modulated within a certain range by an external driving voltage. The output of the VCSO is frequency-divided by 2, amplified, and sent into the AOM for diffraction of the laser beam.

Now the system has formed a closed feedback loop, which, once activated, will minimize the error term $\cos[2\phi_{\mathrm{AOM}}(t) + 2\phi(t)]$ by making the AOM phase modulation $\phi_{\mathrm{AOM}}(t)$ as close as possible to $-\phi(t)$ which is the fiber phase noise with the opposite sign. In this way, the fiber noise can be actively canceled.

Note that one crucial premise for the system to work is that the light frequency shift by the AOM in the optical part must be consistent with the frequency of the VCXO (the reference oscillator) in the electronic part, as otherwise there would be no DC signal corresponding to the fiber phase noise $\phi(t)$ for the loop filter. Since the AOM is driven by the VCSO (the modulation oscillator), we therefore need to make sure that the frequencies of the two oscillators lock to each other. Such a system is referred to as a phase-locked loop, since a constant phase relation (locked-phase) implies that the two signals share the same frequency.

8.2 The First Generation FNC PCBs

A pioneering attempt has been made in Ref. [46] by a previous master student in the group, who has assembled the first generation FNC PCBs. This prototype system was designed and optimized in a way to maximize the bandwidth for compensating noise frequencies as high as possible. As mentioned in Ref. [46], a bandwidth of approximately 20 kHz was achieved with a 20 dB noise suppression.

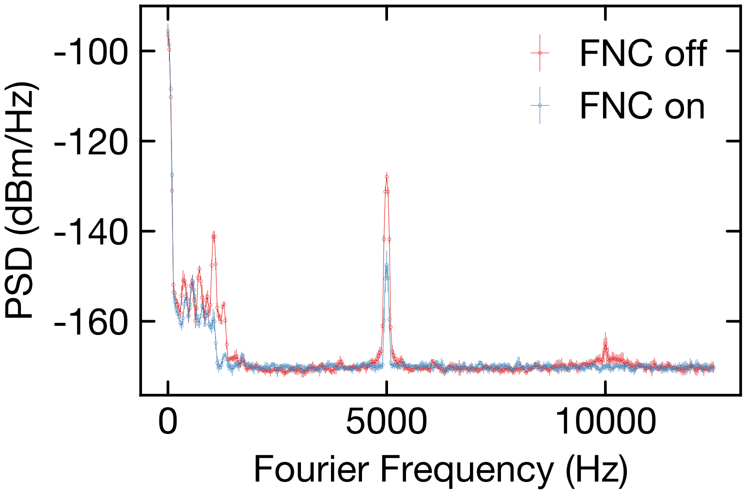

Figure 8.4 Noise cancellation spectrum of the first generation FNC system. An artificial noise is generated at 5 kHz and is suppressed by 20 dB. However, we can see that the noise concentrated below 1 kHz is not well compensated. Such noise is likely due to real environmental noises in the lab and should actually be our target. Adapted from Ref. [46].

However, based on the fiber noise simulation from Cha. 7, the high-frequency noises actually do not really matter for our optical fibers, whereas it is important to instead focus on the low-frequency noises below 1 kHz, which make the predominant contribution to the fiber phase noise. Such law-frequency noises, nonetheless, have not been well compensated. As can be seen in Fig. 8.4, though the first generation system can reduce an artificially generated noise at 5 kHz by 20 dB, it does not really compensate for the low-frequency noises concentrated below 1 kHz, which are very likely due to the actual environment and should exactly be our target.

In order to know what should be changed for the next generation FNC PCBs, we have fully characterized the dynamics of the first generation PCBs, identified the shortcomings, conducted on-site modifications if possible, and gained enough insights for the designing of a more mature FNC system.

8.2.1 The Electronic Setup

Before we analyze the characterization results of the first generation FNC PCBs, let us first look at the details of some of the components that are crucial in understanding the system dynamics. A detailed list of all the major components as well as their testing notes is presented in Appendix **??**.

The VCSO

For our setup, we employ a Vectron VS-705 VCXO with a central frequency at 155.520 MHz. This frequency level is selected to comply with the 80 MHz AOM employed in the optical setup. (Recall that half of the VCXO frequency should match the frequency of the AOM.)

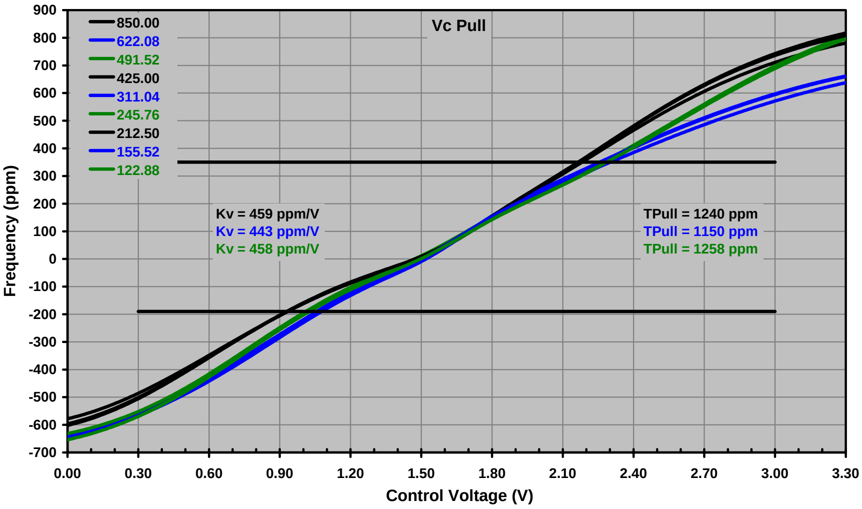

Figure 8.5 VCSO control voltage vs. frequency shift. The oscillator can be frequency-adjusted within a range of -600 to +800 ppm under a control voltage from 0 to 3.3 V. Adapted from Ref. [77].

The relation between the VCSO control voltage and the frequency shift from central frequency is shown in Fig. 8.5. For a working system, the control voltage for VCSO has two components: a DC voltage to shift and match the VCSO frequency to the VCXO frequency, and an AC voltage that compensates for the phase fluctuations due to the fiber.

Ideally, the control voltage starts from a very low level and keeps increasing until the error signal diminishes, which means that the frequencies of the two oscillators match each other. Note that we can only achieve frequency-locking of the two oscillators if we start with a voltage lower than the actual locking voltage. If otherwise we start with a voltage above the locking voltage, the control voltage for VCSO will just keep increasing and overshoot to its maximum. However, such an over-shooting phenomenon can easily happen due to, e.g., something blocking the light path, or the rebooting of the system. Therefore, a convenient reset functionality is required to reset the control voltage to the minimum when overshooting happens. We will discuss this reset function in more detail later in this Chapter.

The Loop Filter

The loop filter of the phase-locked loop transforms the error signal to a modulation voltage for the VCSO, which further actuates the AOM. There are three components designed for the loop filter: proportional (P), integral (I), and derivative (D). As mentioned before, the P element is responsible for an overall amplification of the error signal, the I element handles the low frequency parts, and the D element amplifies the high frequency parts of the error signal. The loop filter is composed of three op-amps: IC201, IC202, and IC203. These op-amps are chosen to be analog devices with low noise specifications and high bandwidths. Their specific part numbers can be found in Tab. B.1 from Appendix **??**. We have calculated the transfer functions for a deeper understanding of the loop filter behavior. The calculation follows the guidelines in Ref. [78] which provides a good introduction to op-amps.

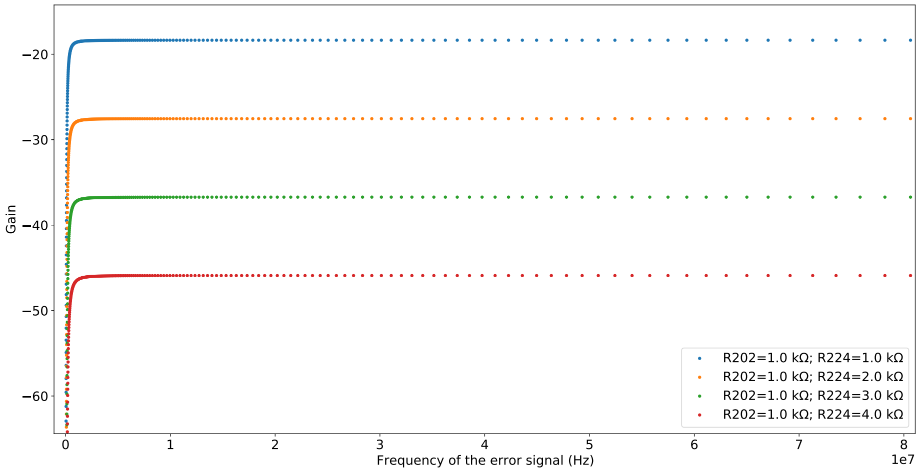

Figure 8.6 Transfer function of the proportional element (IC203) with various R224 values.

The op-amp IC203 is an overall amplifier that serves as a proportional element with the gain level controlled by trimpot R224 with a maximum resistance of 50 kΩ. As can be seen in Fig. 8.6, the proportional gain is frequency-independent and is inversely proportional to the resistance of R224.

Op-amp IC202 is basically a large proportional element that can only be activated by DC signals. Such a feature is ensured by the diodes D204 and D203 associated with IC202 that blocks AC signals. This op-amp is designed particularly for locking the frequency of VCSO to the frequency of VCXO (reference oscillator), as when the two oscillators do not match each other, the error signal will be dominant by a DC term. This DC signal will be amplified by IC202 and drives up the frequency of the VCSO until it matches that of the

VCXO. Once the two oscillators match, the DC error term will diminish and IC202 will become deactivated.

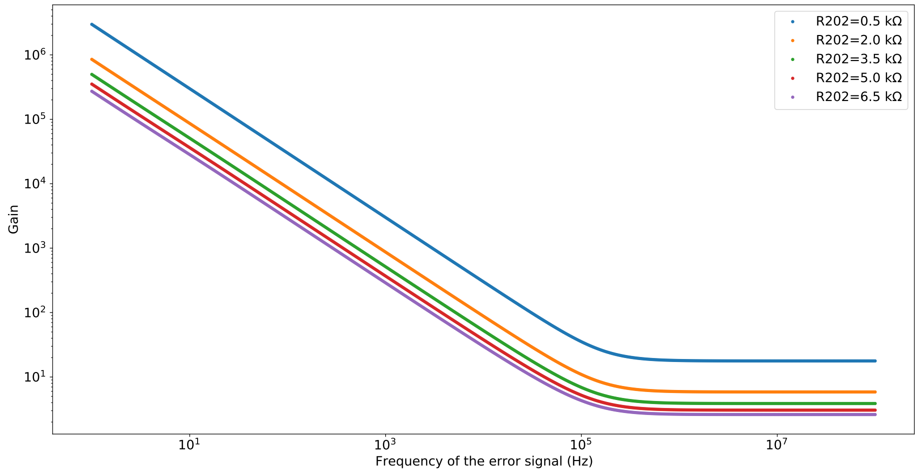

(a)

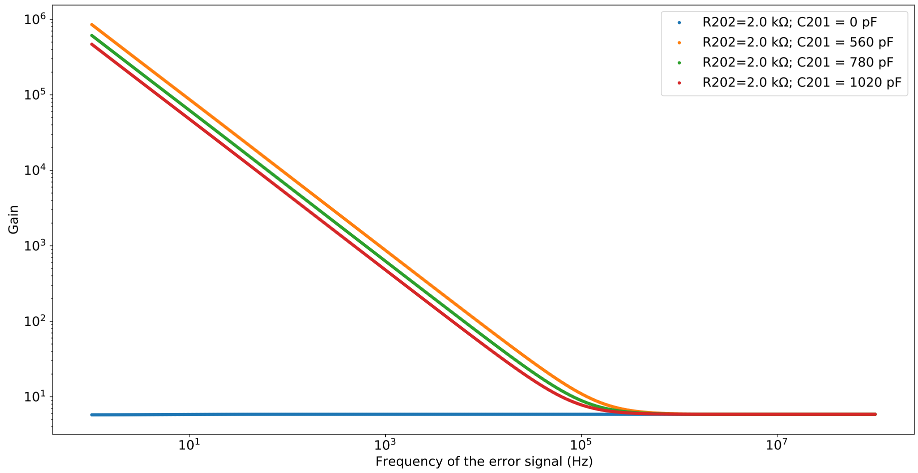

(b)

Figure 8.7 Transfer function of the integral element (IC201). (a) Overall amplification of the integral gain is inversely proportional to the resistance of R202. (b) The corner frequency is inversely proportional to the capacitance of C201. Note that once C201 is shorted, the integral element becomes deactivated (blue curve).

The op-amp IC201 with the capacitor C201 form the integral element. As we can see from Fig. 8.7 (a), the overall gain level of the integral element is inversely proportional to the trimpot R202 which has a maximum resistance of 10 kΩ. The corner frequency, as presented in Fig. 8.7 (b), is determined by the capacitor C201 which is default at 560 pF from the schematics. Note that when the capacitor C201 is shorted, the integral element is deactivated and the gain drops to approximately zero for all frequencies (blue curve in Fig. 8.7 (b)). This feature provides a means to reset the VCSO frequency for solving the overshooting problem mentioned in the previous Section.

Testing of the Electronics

Before testing the overall system performance, we need to first conduct a thorough test of the electronic components and the performances of individual functional modules. A complete list of the components, testing methods, and testing results are presented in Table B.1. Several problems have been identified during this test. The first problem is the cross-talking between the VCXO and the VCSO. As shown in Fig. 8.8 (a), the two oscillators are located on the same PCB and are relatively close to each other. Such a layout could potentially lead to unwanted interference between the signals of the two oscillators. The cross-talking is evidenced in Fig. 8.8 (b), where the output signal of the VCSO is measured in an open-loop configuration in which the frequencies of the two oscillators differ from each other. In the ideal case, we should solely see a single signal at the VCSO frequency with all the other signals buried under the noise background. However, we observe a clear signal corresponding to exactly the VCXO frequency from the VXSO output, which confirms the existence of cross-talking.

Moreover, instead of internal signal interference, the system is also vulnerable to electromagnetic interference (EMI) from the environment due to the lack of a proper shielding. We have observed multiple times that unexpected peaks showing up in the main output port, which, after a lot of searching, are found to correspond to nearby direct digital synthesis (DDS) devices or other lab signals. These unexpected peaks keep showing up with the same amplitudes even when the power supply is isolated from ground via an isolation transformer, which indicates that the spurious signals do not come from grounding but are actually picked up by the PCBs from the air. Additionally, it occurs that sometimes the system could fall out of lock by a change of the nearby parasitic capacitance due to, e.g., the movement of the operator.

Furthermore, the power supply scheme does not coordinate well with some of the electronic components. The board currently has a single external power supply of ±15 V, while the two oscillators as well as some other components require an operating voltage of 3.3 V. This large voltage difference causes a sizeable burden on the voltage regulators responsible for converting 15 V down to 3.3 V. As a result, the voltage regulators are significantly heated up. Such an excess amount of heat causes potential safety issues especially for long-time operation of the boards.

In spite of the aforementioned issues, the first generation PCBs in general fulfill their roles as a prototype system. The solutions to the identified problems will be fully discussed

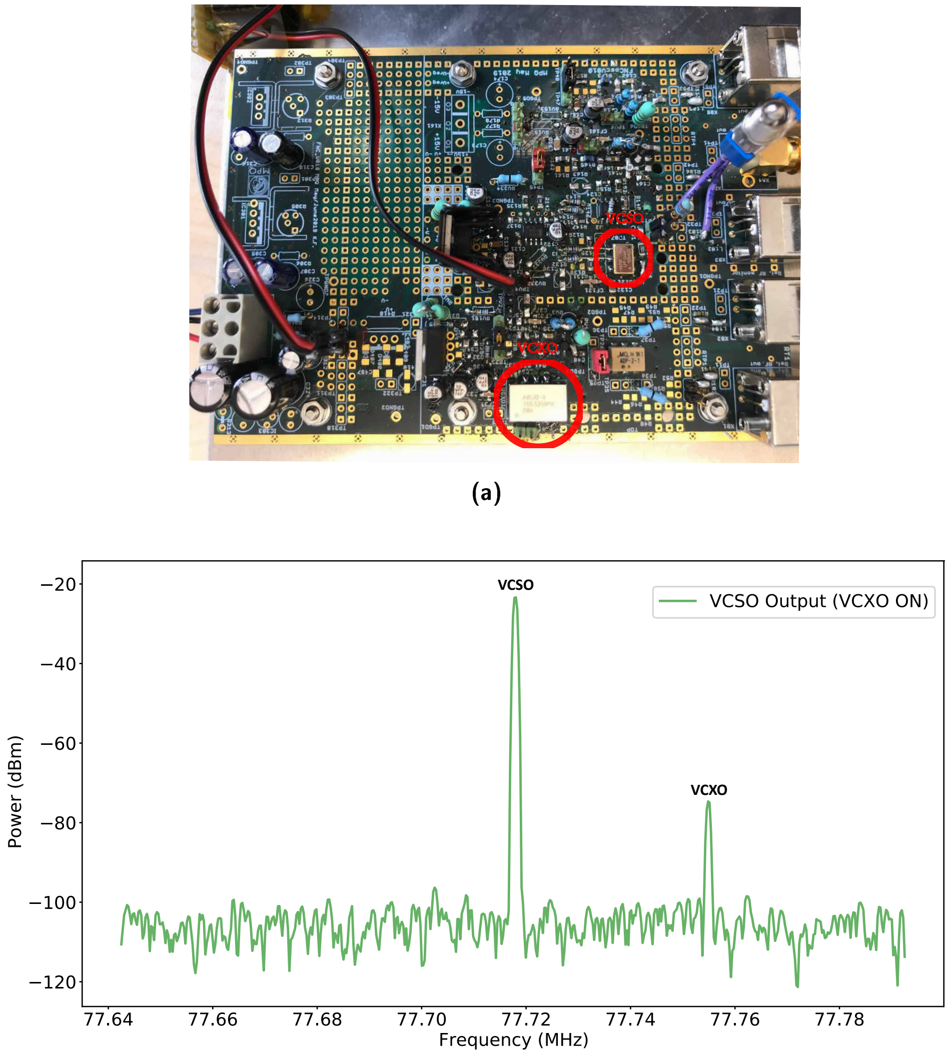

(a)

(b)

Figure 8.8 Cross-talking of the two oscillators. (a) The VCSO and the VCXO are located at the same PCB and are relatively close to each other. (b) The signal measured at the VCSO output port contains a component from the VCXO when the two oscillators are unlocked.

in Section 8.3.

Implementation of the Automatic Reset Functionality

As mentioned before, the system will fall out of the lock when the light path is disturbed or blocked which leads to overshooting of the VCSO control voltage. Once the system is unlocked, we need to reset the control voltage to its minimum by shorting the capacitor C201. In the first generation design, a reset button is implemented to allow for manual resetting of the system. However, it is unpractical to have people continuously check and reset the system during long-term operations. We thus decide to implement an automatic reset functionality for the system.

The automatic reset system is composed of two parts: a voltage comparator circuit as shown in Fig. 8.9 (a), and an alert system shown in Fig. 8.9 (b). When the system is stably locked, we measure the locking voltage for the VCSO to be 1.08 V. When the system falls out of lock and the loop filter overshoots, the VCSO control voltage will swing to the maximum value which is measured to be 2.4 V. The voltage comparator circuit measures the real-time VCSO control voltage and compares it with a set value slightly below the overshooting voltage. Once the the control voltage exceeds the set value, the output of the voltage comparator circuit will go to the ”low“ channel (-Vs), which would then turn on the active-low analog switch (DG417CJ) to short the integral element (C201) in the loop filter. This shorting resets the error signal to the minimum (see Fig. 8.7, blue curve), so that the system can lock again. The alert system is made of a buzzer and an red LED. The buzzer will start to beep once the system falls out of the lock, and stop beeping if it is locked again. The LED, on the other hand, is controlled by a Flip-Flop (SN74LVC1G74) that has a memory over the locking status. The LED will be triggered once the system is unlocked but will remain ON unless being manually reset to provide information to the operator whether the system has been unlocked from last check.

A picture of the complete setup of the FNC PCBS is shown in Fig. 8.10. The oscillator board (horizontal), the mixer board (vertical), and the automatic reset system (horizontal small) are tightly mounted on a piece of aluminum board for physical stability.

8.2.2 Characterization of the First Generation FNC System

To fully characterize the first generation FNC system, we have conducted two sets of performance tests: an electronic test and an optical test. In the electronic test, the FNC PCBs are locked to themselves to cancel out an electronic noise generated by a function generator. In the optical case, the PCBs and the optical components are integrated to compensate against the actual fiber noise generated by a speaker. The electronic test allows us to have a more precise control over the artificial noise and maintain the same input noise strength across different frequencies, while the optical test gives us the knowledge of the system performance in a real-world setting. In both cases, a systematic evaluation of the effects of different loop filter parameters are conducted.

Performance Test with Optics

Following the setup in Fig. 8.3, we test the system performance in canceling actual fiber noise. For testing purposes, instead of the 671 nm laser we couple the clock laser at

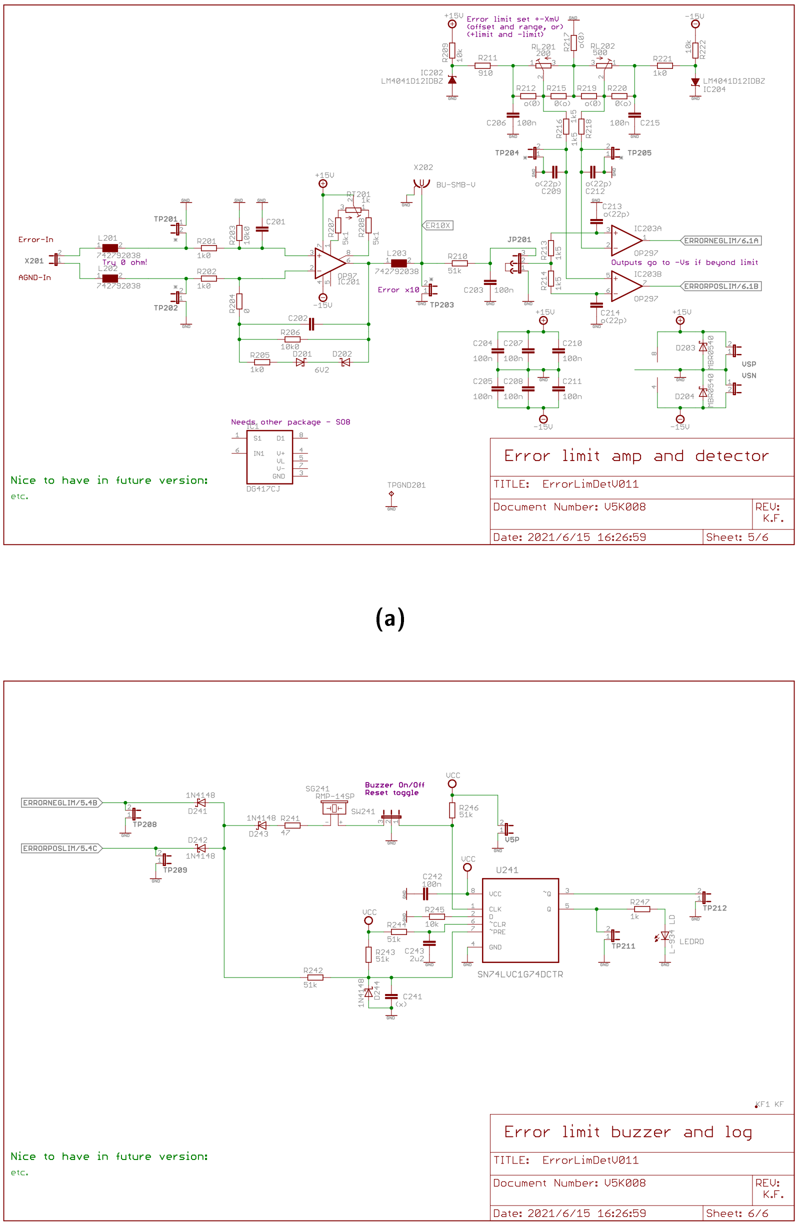

(a)

(b)

Figure 8.9 Electronic schematics of the automatic reset system. (a) The voltage comparator circuit and the active-low switch. (b) The alert system with a red LED controlled by a D-type flip-flop and a buzzer.

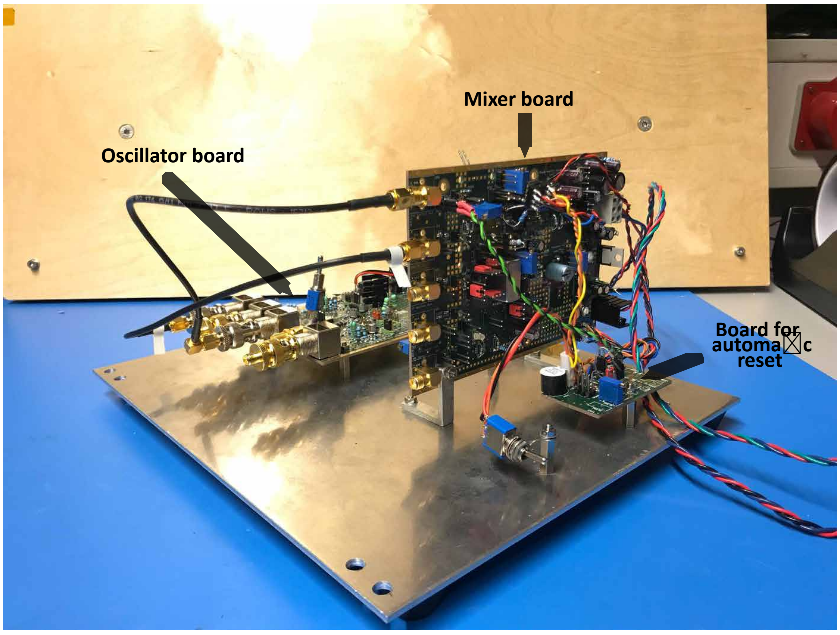

Figure 8.10 Picture of the first generation FNC PCBs together with the automatic reset system.

698 nm with a narrower linewidth to the desired PM-630-HP fiber. Acoustic waves are generated by the Visaton FRS 5 loudspeaker driven by a function generator. The acoustic waves are directed onto the fiber so that light traveling through picks up the fiber noise at the given frequency. An example noise spectrum measurement is shown in Fig. 8.11, where artificial noise at 300 Hz is generated and the photodiode signals are detected by a spectrum analyzer. The red curve represents the noise spectrum without the FNC. The first order noise side-peaks are exactly 300 Hz away from the carrier. The carrier to first order noise side-peak ratio is only 16.70 dB, indicating a very strong noise level. Once we turn on the FNC, we observe directly a suppression of the noise side-peaks, leading to a carrier to noise side-peak ratio of 71.42 dB, which means that the FNC system is able to reduce the noise level at 300 Hz by $71.42 - 16.70 = 54.72$ dB. Additionally, as we can see from the plot, there exists a lump around the carrier corresponding to low frequency noises from the environment. This behavior is predicted from the fiber noise simulation in Chapter 7, which shows that the fiber is more sensitive against low frequency noises. With the FNC turned on, we are able to significantly reduce the height and width of this lump. (Note that the data taken process involves producing loud acoustic noises, and we have to wear high-quality earplugs to minimize the effect of the disturbing acoustic noise on our physical and mental well-being.)

As we can see from Fig. 8.12, the performance of the system against various noise frequencies ranging from 10 Hz to 8 kHz is measured with three different integral gains (R202 equals 0.39 kΩ, 1.18 kΩ, and 3.9 0.39 kΩ). In order to have a more solid ground for comparison, all the data are taken with the fixed relative distance between the speaker and

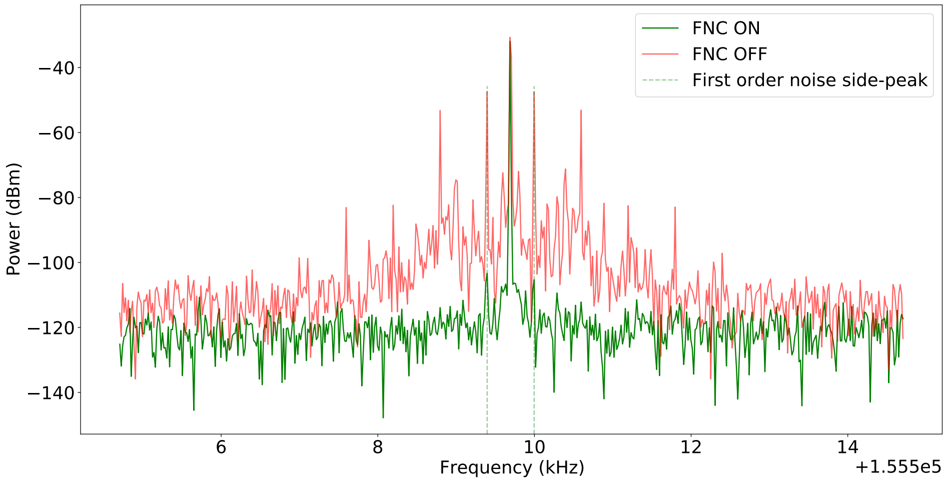

Figure 8.11 Example FNC spectrum. An artificial fiber noise is generated at 300 Hz and the photodetector signal with and without the FNC system is measured by a spectrum analyzer. The first order noise side-peaks are exactly 300 Hz away from the carrier. The carrier to first order noise side-peak ratio is 16.70 dB for the FNC OFF case, and is 71.42 dB once the FNC system is turned on, indicating a noise suppression level of 54.72 dB for fiber noise at this frequency. The loop filter parameters for this measurement are R202 = 0.39 kΩ, C201 = 560 pF, and R224 = 1.18 kΩ.

the fiber, and with a consistent driving voltage for the speaker. However, the speaker may have different performances at different frequencies even with the same driving power, and we can thus only guarantee a relatively consistent artificial noise input into the fiber. Note that do not confuse the noise input into the fiber with the actual fiber noise seen by the light: the former is what we are trying to control here and the latter is related to the properties of the fiber. For a more consistent framework, we have conducted electronic tests of the FNC performance where the input noise power is guaranteed to be absolutely the same. The results from the electronic tests are presented in the next Section.

As shown in Fig. 8.12, the lowest R202 value (blue curve) corresponds to the strongest noise cancellation performance, which is predicted by the transfer function calculation in the previous Section. The noise suppression levels can be deducted by taking the difference between the carrier to noise side-peak ratios for the FNC ON and FNC OFF cases. The system is able to achieve a noise suppression of about 20 dB for low frequencies below 80 Hz, and a suppression of roughly 40 dB for medium frequencies between 100 Hz and 1.2 kHz. The system performance drops at higher frequencies above 1.5 kHz. However, as we can see from the plot, the carrier to noise side-peak ratio increases to a high level at high frequencies for the FNC OFF case, indicating that the strength of the fiber noise at high frequencies becomes extremely weak. Such a behavior is exactly predicted by the fiber noise simulation in Chapter 7, which shows that the fiber is orders-

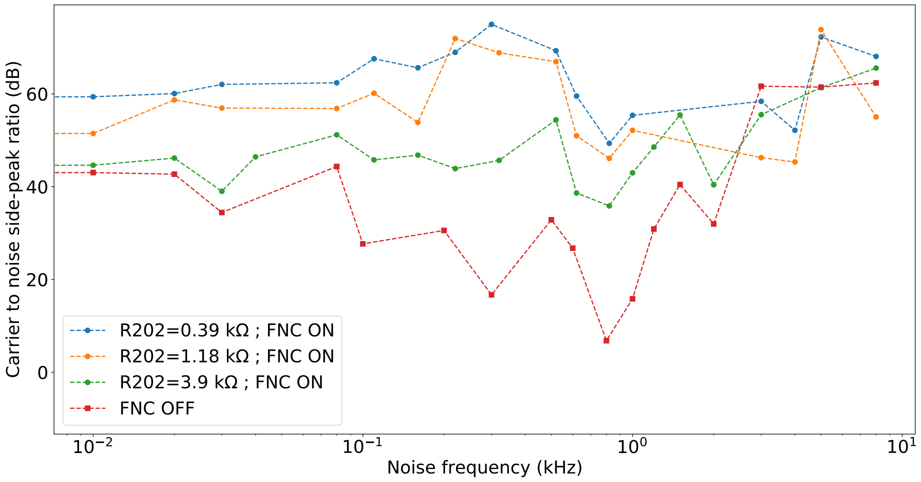

Figure 8.12 Fiber noise cancellation performance of the first generation FNC system. Artificial noise is generated by the Visaton FRS 5 loudspeaker driven by a function generator. The carrier to noise side-peak ratios are measured at different frequencies ranging from 10 Hz to 8 kHz with various R202 values. The other loop filter parameters are fixed at R224 = 1.18 kΩ and C201 = 560 pF during the test. A higher carrier to noise side-peak ratio indicates a lower noise level present in the light. The noise suppression level due to the system is represented by the difference between the FNC ON curves and the FNC OFF curve.

of-magnitudes less sensitive against high frequency noises. In this way, the system's low performance at frequencies above 1.5 kHz is acceptable.

Performance Test with Pure Electronics

The optical performance test provides a good qualitative description of how well the FNC system behaves in real-world settings. However, as mentioned before, we cannot guarantee that the speaker produces absolutely the same acoustic power at different frequencies even if it is under the same driving voltage. To obtain a more quantitative view of the system performance, we have also conducted a performance test with pure electronics.

In the real-world setting, the correction for the fiber noise manifests itself as an AC modulation on top of the DC signal driving and shifting the VCSO frequency to match that of the VCXO. Such a correction can also be triggered in a purely electronic way. Instead of actuating the AOM, the output of the VCSO is directed into the RF port of the mixer forming a closed loop. A function generator imposes an extra AC modulation directly onto the signal that goes into the RF port of the mixer to imitate the fiber noise. This AC modulation will end up in the error signal for the loop filter and be eventually compensated. The carrier frequency and the noise spectrum are revealed by a spectrum analyzer monitoring the VCSO output.

We calculate the carrier to noise side-peak ratio (in dB) to quantify the strength of the noise present in the system: the higher this ratio, the lower the actual noise level and the more noise suppression by the system. An example noise spectrum is shown in Fig. 8.13. In this measurement, artificial noise at 160 kHz is generated and fed into the system, which is revealed as the noise side-peaks marked by the dashed lines 160 kHz away from the carrier. The ratio between the carrier and the noise side-peak is calculated to be 60.94 dB.

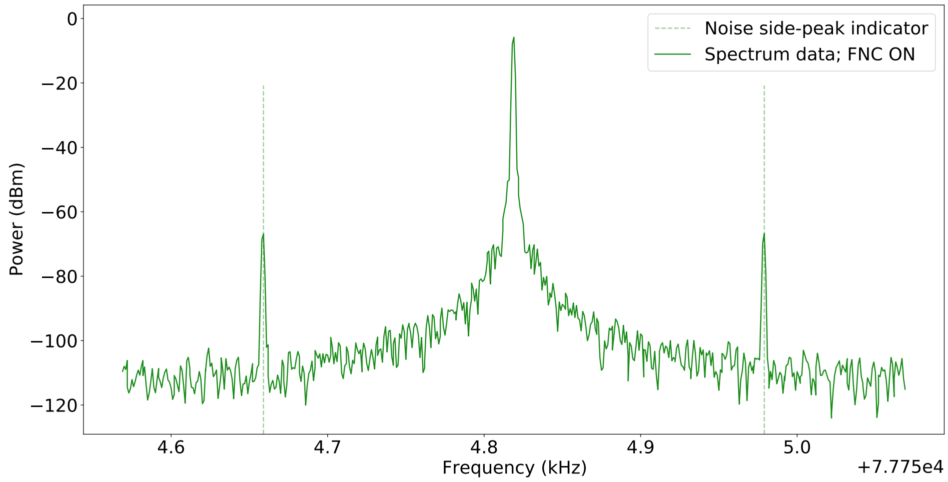

Figure 8.13 FNC spectrum from the electronic test. Artificial noise at 160 kHz is fed into the system. The noise side-peaks indicated by the dashed lines are exactly 160 kHz away from the carrier. The carrier to noise side-peak ratio is calculated to be 60.94 dB.

In the same manner, the carrier to noise side-peak ratios are measured at 21 frequency samples ranging from 10 Hz to 20 kHz for various loop-filter parameters. As discussed in the previous Section, there are three major parameters regulating the performance of the loop filter: the resistor R202 controls the overall amplification level of the integral gain, the capacitor C201 governs the corner frequency, and the resistor R224 is responsible for the overall proportional gain.

A systematic evaluation of the effects of R202 is presented in Fig. 8.14. The values of R202 range from 0.49 kHz to 7.5 kHz, while R224 and C201 are fixed at 1.2 kHz and 560 pF. We have observed that the noise suppression level is inversely proportional to the resistance of R202, which is as predicted by the transfer function calculation shown in Fig. 8.7 (a).

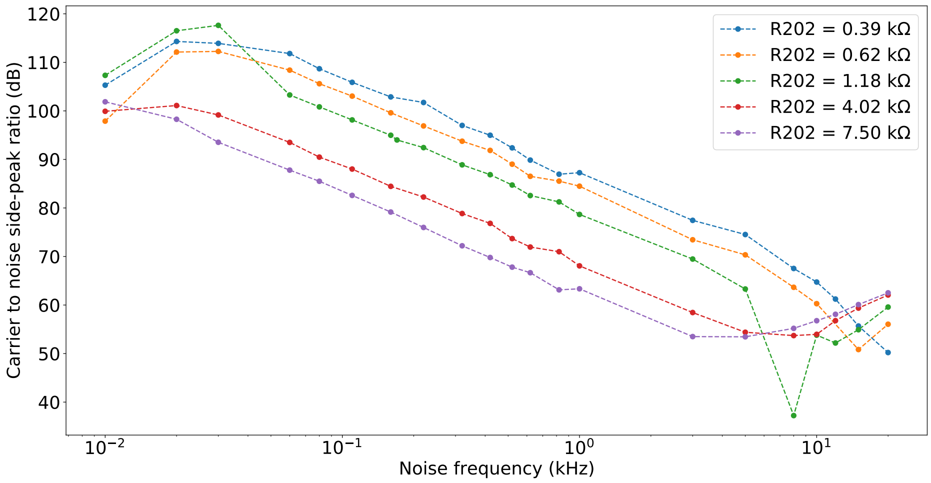

Figure 8.14 Effect of the overall amplification of the integral element (R202) on the FNC performance from the electronic performance test. R224 and C201 are held to be constant at 1.21 kΩ and 560 pF, respectively.

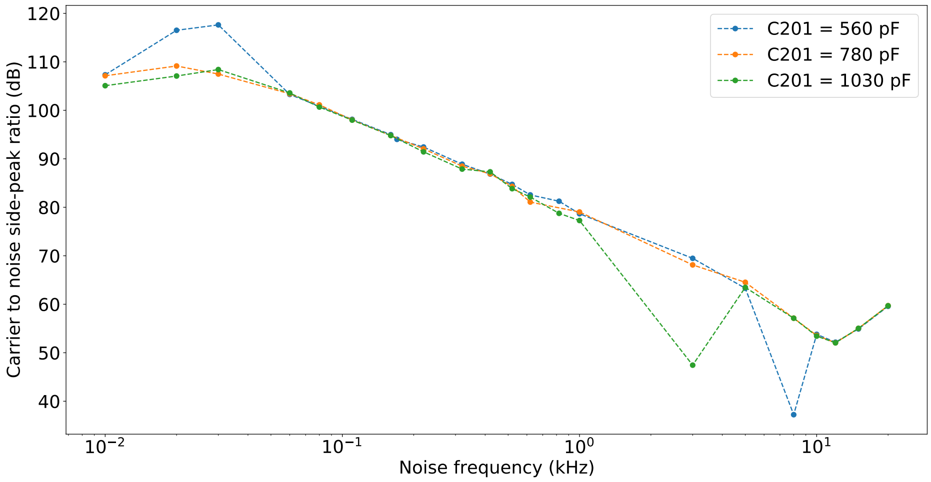

Figure 8.15 Effect of the corner frequency of the integral element (C201) on the FNC performance from the electronic performance test. R224 and C201 are held to be constant at 1.21 kΩ and 560 pF, respectively.

The effects of various C201 values ranging from 560 pF to 1030 pF on the system performance are shown in Fig. 8.15. It seems that the noise cancellation performance is not significantly affected by a change of the C201 value within this range. This behavior is predicted by the transfer function calculation in Fig. 8.7 (b), which leads to a corner frequency around 100 kHz for a C201 value within the aforementioned range This corner frequency is way higher than the highest noise frequency applied during the electronic test. Since all the generated noises are within the corner frequencies, it is expected that we do not observe a large difference among the above measurements.

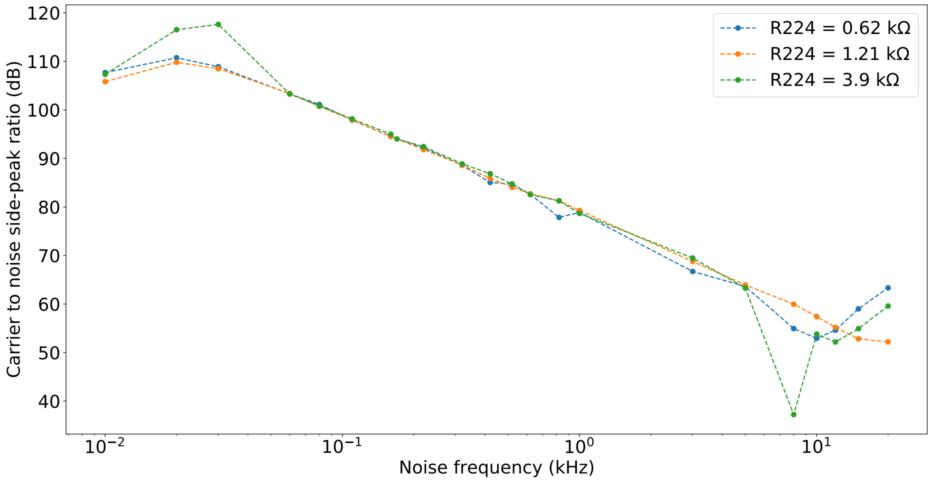

Figure 8.16 Effect of the proportional gain (R224) on the FNC performance from the electronic performance test.

Similar to the situation for C201, we also do not observe a significant effect of R224 on the system performance, as can be seen in Fig. 8.16. Such a behavior can also be explained by the transfer function calculation shown in Fig. 8.6. As we can see, the overall proportional gain is below 100 while the integral gain is orders-of-magnitude higher. Since the integral element takes the absolute domination, a change of the proportional gain has a negligible effect on the overall system performance.

It is worth mentioning that the downward trend of the curves in Fig. 8.14, Fig. 8.15, and Fig. 8.16 indicates that the FNC system has a weaker noise suppression capability for higher noise frequencies. This behavior is due to the finite time required for the signal to travel between different electronic components. Such a delay will induce a phase change that significantly degrades the validity of the correction signal for high frequency noises. However, it is not necessary to be panic over fiber noises at such high frequencies based on both the prediction from the simulation in Sec. 7.3.3 and the optical test, which all show that the actual fiber noise at frequencies above several kHz are orders-of-magnitude weaker than low frequency noises.

The evidence gathered from the electronic performance test brings us several insights for the next generation FNC system. First of all, the system behavior is solely dominated by the loop filter parameter controlling the overall amplification of the integral element

(R202), while the other parameters contribute negligibly to the final gain. However, in general we would like to achieve a balance between different loop parameters, and avoid the situation where one component is operating nearly at the saturation level while others are not really relied at all. Therefore, we would like to readjust the design for the proportional gain to allow for a much larger contribution from this component in the next generation FNC system. Moreover, the corner frequency is set to be too high, which not only amplifies the gain for low frequencies, but also leads to a high gain for high frequencies. We do not, however, desire too much gain for high frequencies, given that it could potentially lead to noises due to internal delay, not mentioning that the actual optical fiber is much more robust against high frequency noises above several kHz. Therefore, we could like to adjust the schematics to reduce the corner frequency from 100 kHz down to within 10 kHz for the next generation FNC system.

8.3 Designing Guidelines for the Next Generation FNC System

We have fully characterized the prototype FNC system through a thorough test of the individual electronic components, an optical performance test for actual fiber noise cancellation, and an electronic performance test focusing on a systematic analysis of the loop filter parameters. Here we will provide a brief summary of the problems identified, and present the possible solutions for the second generation FNC system.

The solution for the reset problem has already been developed and tested on the first generation board. We will keep this design for the next generation system. To solve the problem of excess heat for certain voltage regulators, we will add a second external power supply at ±5 V to power the 3.3 V elements. To prevent the VCSO and the VCXO from cross-talking, we will separate them into different PCBs and provide individual shielding for them. The first generation board is vulnerable to external EMI. This situation can be alleviated with proper shielding. On top of an overall shielding for the next generation FNC PCBs, we plan to design a special cap attached with short metal plates that once closed, can isolate and shield each individual functional region or component on the board. For the loop filter, we will keep the general structure but redesign the scales of the parameters to obtain a better balance between the proportional and integral gains. We will also lower the high frequency gains by adjusting the corner frequency for the integral element from 100 kHz down to around several kHz.

In general, the first generation FNC system serves as an excellent prototype. We believe that with the insights gained from this system, we are able to achieve a more mature and powerful FNC system for the next generation.

Chapter 9

Conclusion and Outlook

The main aim for this project was to construct a stable narrow-linewidth laser for the $^1S_0$-$^3P_2$ transition in strontium. In Chapter 3, we reported on the construction of a linear ECDL system for the generation of a single-mode laser light at 671 nm. To enhance the optical power while maintaining a high-quality optical mode, we set up a stable injection-lock system able to amplify the optical power after fiber coupling to 64.1 mW, which was three times larger than the power directly from the ECDL.

In Chapter 4, we described the dual sideband locking scheme developed based on regular PDH locks for frequency-stabilizing the $^1S_0$-$^3P_2$ laser to an reference cavity. To realize this scheme, we constructed a home-built EOM module for a fixed phase modulation at 38.24 MHz, and applied a commercial fiber EOM to modulate the light at an adjustable frequency.

In Chapter 6, we reported on an active temperature stabilization system for the reference cavity. We developed and tested two different approaches involving the use of commercial analog temperature servos and a home-built digital servo. The analog approach, though only employed the proportional element due to internal limitations of analog circuits, delivered a lower overlapping Allan deviation and provided more temperature stability. Nonetheless, both approaches were expected to be sufficient as a first-stage temperature stabilization device as they were able to maintain a temperature fluctuation within 0.15 K against the maximum ambient temperature fluctuation of 1 K. This level of stability provides good support to the second-stage temperature stabilization system inside the vacuum housing and serves as an extra warranty for achieving the ultralow 1 mK temperature instability inside the cavity.

In Chapter 5, we reported on the construction and characterization of the ultra-stable reference cavity for the implementation of the dual sideband locking scheme. The cavity was coupled with both the $^1S_0$-$^3P_2$ laser and the $^1S_0$-$^3P_0$ clock laser. We performed cavity ring down measurements and determined the finesses for the $^3P_2$ laser and the clock laser to be 20000 and 300000, corresponding to a cavity linewidth of 75 kHz and 5 kHz. Since the coating for the ULE resonator is more suitable for the clock laser wavelength, the measured cavity linewidth for the $^1S_0$-$^3P_2$ laser is one order of magnitude less than that of the clock laser. The 5 kHz cavity linewidth for the clock laser leads to a final laser linewidth on the Hz level from a previous beat measurement [15], which is three orders of magnitude narrower than the cavity linewidth. Comparatively, and from a conservative point of view, we estimated that the $^1S_0$-$^3P_2$ laser should be at least one order of magnitude narrower than the cavity linewidth, which was already narrow enough to resolve the energy splittings between two adjacent layers of Sr atoms calculated to be 25 kHz for ^{88}Sr and 33 kHz for ^{87}Sr. So far we have only indirectly estimated the linewidth of the $^1S_0$-$^3P_2$ laser. In the future, we plan to gain a more accurate knowledge of the linewidth from spectroscopy experiments in the vertical lattice where we can choose a proper polarization of the lattice beam to make the lattice magic [6]. Additionally, it would also be helpful if we perform further optimization of the transmission signal for the cavity which would also lead to more stability and a narrower laser linewidth.

Chapter 7 and Chapter 8 focused on reducing the phase noise that the laser beam picked up when travelling through an optical fiber. In Chapter 7, we simulated the power spectral density of the fiber phase noise using the fluctuation dissipation theorem. The simulation revealed that the biggest contribution for fiber noise arose from frequencies that are below 1 kHz and provided insights for optimizing an active fiber noise cancellation system. In Chapter 8, we reported on the thorough characterization of a prototype fiber noise cancellation system that was first assembled by a previous group member [46], and provided guidelines for designing the next generation system. We discovered that the fiber became much more insensitive to noises at frequencies higher than 1.5 kHz, which was predicted by the simulation. We optimized the loop filter to deliver a noise suppression of 20 dB for frequencies below 80 Hz, and a suppression of 40 dB for frequencies between 100 Hz and 1.2 kHz. We developed and tested the automatic reset functionality on the prototype system which would be added to the next generation system. For the next generation system, we suggested to make the upgrades including separation of the oscillators, better shielding, and extra power supply for low voltage components. And for better loop-filter performance, we recommended to reduce the corner frequency for the integral element and achieve a better balance between the proportional gain and the Integral gain. The next generation system is currently under design by the professional electrician in the group based on insights gained from this test. We believe that the new system, once finished, would be helpful for not only the $^1S_0$-$^3P_2$ laser but also for all the other narrow-linewidth laser systems in the laboratory.

In conclusion, we demonstrated the ability to generate, stabilize, and transport a high-quality laser light for the $^1S_0$-$^3P_2$ transition in strontium. We are confident that this laser system will play a positive role in the preparation for a single layer of strontium atoms in our optical lattice.

References

[1] I. Bloch, J. Dalibard, and S. Nascimbène. *Quantum simulations with ultracold quantum gases*, Nature Physics **8**, 267 (2012). DOI: 10.1038/nphys2259.

[2] D. Greif, M. F. Parsons, A. Mazurenko, C. S. Chiu, S. Blatt, F. Huber, G. Ji, and M. Greiner. *Site-resolved imaging of a fermionic Mott insulator*, Science **351**, 953–957 (2016). DOI: 10.1126/science.aad9041.

[3] W. S. Bakr, J. I. Gillen, A. Peng, S. Fölling, and M. Greiner. *A quantum gas microscope for detecting single atoms in a Hubbard-regime optical lattice*, Nature **462**, 74 (2009). DOI: 10.1038/nature08482.

[4] J. F. Sherson, C. Weitenberg, M. Endres, M. Cheneau, I. Bloch, and S. Kuhr. *Single-atom-resolved fluorescence imaging of an atomic Mott insulator*, Nature **467**, 68 (2010). DOI: 10.1038/nature09378.

[5] C. Weitenberg, M. Endres, J. F. Sherson, M. Cheneau, P. Schauß, T. Fukuhara, I. Bloch, and S. Kuhr. *Single-spin addressing in an atomic Mott insulator*, Nature **471**, 319–324 (2011). DOI: 10.1038/nature09827.

[6] A. Heinz. *Ultracold Strontium in State-Dependent Optical Lattices*, PhD Thesis Ludwig-Maximilian Universität München (2020). URL: https://ultracold.sr/publications/thesis_andre_heinz.pdf.

[7] T. Nicholson *et al. Systematic evaluation of an atomic clock at* 2×10^{-18} *total uncertainty*, Nature Communications **6**, 6896 (2015). DOI: 10.1038/ncomms7896.

[8] A. Cooper, J. P. Covey, I. S. Madjarov, S. G. Porsev, M. S. Safronova, and M. Endres. *Alkaline-Earth Atoms in Optical Tweezers*, Physical Review X **8**, 041055 (2018). DOI: 10.1103/PhysRevX.8.041055.

[9] X. Xu, T. H. Loftus, J. L. Hall, A. Gallagher, and J. Ye. *Cooling and trapping of atomic strontium*, Journal of the Optical Society of America B **20**, 968 (2003). DOI: 10.1364/JOSAB.20.000968.

[10] J. A. Muniz, D. J. Young, J. R. K. Cline, and J. K. Thompson. *Cavity-QED measurements of the* $^{87}\mathrm{Sr}$ *millihertz optical clock transition and determination of its natural linewidth*, Phys. Rev. Research **3**, 023152 (2021). DOI: 10.1103/PhysRevResearch.3.023152.

[11] J. E. Sansonettia and G. Nave. *Wavelengths, Transition Probabilities, and Energy Levels for the Spectrum of Neutral Strontium (Sr I)*, Journal of Physical and Chemical Reference Data **39**, 033103 (2010). DOI: 10.1063/1.3449176.

[12] M. Yasuda and H. Katori. *Lifetime Measurement of the* $^3P_2$ *Metastable State of Strontium Atoms*, Physical Review Letters **92**, 153004 (2004). DOI: 10.1103/PhysRevLett.92.153004.

[13] O. Onishchenko, P. Sergey, A. Urech, C. Chen, S. Bennetts, G. A. Siviloglou, and F. Schreck. *Frequency of the ultranarrow* $^1S_0{-}^3P_2$ *transition in* $^{87}\mathrm{Sr}$, Phys. Rev. A **99**, 052503 (2019). DOI: 10.1103/PhysRevA.99.052503.

[14] S. Falke *et al. A strontium lattice clock with* $3{\times}10^{-17}$ *inaccuracy and its frequency*, New Journal of Physics **16**, 073023 (2014). DOI: 10.1088/1367-2630/16/7/073023.

[15] F. Wallner. *New Tools for Controlling Strontium Atoms with High Spectral and Spatial Resolution*, Master Thesis Technische Universität München (2020). URL: https://ultracold.sr/publications/thesis_florian_wallner.pdf.

[16] K. Shibata, R. Yamamoto, Y. Seki, and Y. Takahashi. *Optical spectral imaging of a single layer of a quantum gas with an ultranarrow optical transition*, Physical Review A **89**, 031601 (2014). DOI: 10.1103/PhysRevA.89.031601.

[17] R. Yamamoto, J. Kobayashi, T. Kuno, K. Kato, and Y. Takahashi. *An ytterbium quantum gas microscope with narrow-line laser cooling*, New J. Phys. **18**, 023016 (2016). DOI: 10.1088/1367-2630/18/2/023016.

[18] F. Träger. *Springer Handbook of Lasers and Optics*. Springer, 2012. ISBN: 978-3-642-19409-2.

[19] J. Liu. *Laser Oscillation*. Cambridge University Press, 2016, pp. 274–296. ISBN: 9781316687109.

[20] P. Dirac. *The Quantum Theory of the Emission and Absorption of Radiation*, Proc. Royal Soc. Lond. A **114**, 243–265 (1927). DOI: 10.1098/rspa.1927.0039.

[21] R. Fernow. *Introduction to Experimental Particle Physics*. Cambridge University Press, 1989. ISBN: 978-0-521-379-403.

[22] O. Svelto. *Principles of Lasers*. Springer, 1998. ISBN: 978-1-4757-6266-2.

[23] W. Demtröder. *Laser Spectroscopy*. Springer, 2008. ISBN: 978-3-540-73418-5.

[24] R. Pantell and H. Puthoff. *Fundamentals of Quantum Electronics*. Wiley, 1964. ISBN: 978-0471657903.

[25] D. Griffiths. *Introduction to Electrodynamics*. Cambridge University Press, 1989. ISBN: 978-1108420419.

[26] W. Koechner. *Solid-State Laser Engineering*. Springer, 1996. ISBN: 978-0-387-29338-7.

[27] A. Siegman. *Lasers*. Univ. Sci. Books, Mill Valley, 1986. ISBN: 978-0-935702-11-8.

[28] Thorlabs. *Bandpass Filter Tutorial*, (visited on 11/09/2021). URL: https://www.thorlabs.com/newgrouppage9.cfm?objectgroup_id=10772.

[29] Laser Focus World. *Laser-diode Electronics: How to protect your laser diode from electrically caused damage*, (visited on 19/11/2020). URL: https://www.laserfocusworld.com/lasers-sources/article/16548195/laserdiode-electronics-how-to-protect-your-laser-diode-from-electrically-caused-damage.

[30] Edmund Optics. *Laser Beam Shaping Overview*, (visited on 08/02/2021). URL: https://www.edmundoptics.com/knowledge-center/application-notes/optics/laser-beam-shaping-overview/.

[31] Laser Glow Technologies. *Laser Beam Profiles*, (visited on 08/02/2021). URL: https://www.laserglow.com/content/Laser-Beam-Profiles.

[32] B. Saleh and M. Teich. *Fundamentals of Photonics.* Wiley, 2007. ISBN: 978-0-471-35832-9.

[33] E. Staub. *Developing a High-Flux Atomic Beam Source for Experiments with Ultracold Strontium Quantum Gases*, Master Thesis Ludwig-Maximilian Universität München (2019). URL: https://ultracold.sr/publications/thesis_etienne_staub.pdf.

[34] H. Huber *et al. Picsecond Laser Structuring for the Monolithic Serial Intercombination of CIS Solar Cells*, EUPVSEC conference **3BV.5.78**, 3066–3071 (2009). DOI: 10.4229/24thEUPVSEC2009-3BV.5.78.

[35] M. Peiris. *Coupling a LASER into a single mode fiber (video)*, (2012). URL: https://www.youtube.com/watch?v=kQvhbJbDG0M.

[36] N. Jansa. *A frequency-stable diode laser system for spectroscopy and trapping of Sr atoms*, Master Thesis Ludwig-Maximilian Universität München (2016). URL: https://ultracold.sr/publications/thesis_nejc_jansa.pdf.

[37] E. Black. *An introduction to Pound–Drever–Hall laser frequency stabilization.*, American Journal of Physics **69**, 79 (2001). DOI: https://doi.org/10.1119/1.1286663.

[38] S. Karna and A. Yeates. *Nonlinear Optical Materials: Theory and Modeling.* American Chemical Society, Inc., 1996. ISBN: 0-8412-3401-9.

[39] SiTime. *Time Machine II User Manual*, (2019). URL: https://media.digikey.com/pdf/Data%20Sheets/SiTime%20PDFs/Time-Machine_II_UM_7-24-19.pdf.

[40] J. Thorpe, K. Numata, and J. Livas. *Laser frequency stabilization and control through offset sideband locking to optical cavities*, Opt Express (2008). DOI: 10.1364/oe.16.015980.

[41] A. Fox and T. Li. *Resonant Modes in a Maser Interferometer*, Bell Labs Technical Journal **40**, 453–488 (1961). DOI: 10.1002/j.1538-7305.1961.tb01625.x.

[42] R. Paschotta. *Finesse*, (visited on 09/20/2021). URL: https://www.rp-photonics.com/finesse.html.

[43] T. Li. *Zero-crossing temperature of ultra-stable optical reference cavity measured by optical transition spectrum*, Acta Phys. Sin. **70(7)**, 073701 (2021). DOI: 10.7498/aps.70.20201721.

[44] D. Jastrzebski. *Nature and Properties of Engineering Materials*. Vol. 4. John Wiley & Sons, Inc., 1959, pp. 372–373. DOI: 10.1002/app.1960.070041224.

[45] S. Webster, M. Oxborrow, and P. Gill. *Vibration insensitive optical cavity*, Phys. Rev. A **75**, 011801(R) (2007). DOI: 10.1103/PhysRevA.75.011801.

[46] R. Haindl. *A Clock Laser System for Quantum Simulations with Ultracold Strontium Atoms*, Master Thesis Ludwig-Maximilian Universität München (2019). URL: https://ultracold.sr/publications/thesis_rudolf_haindl.pdf.

[47] J. Alnis, A. Matveev, N. Kolachevsky, T. Udem, and T. Hänsch. *Subhertz linewidth diode lasers by stabilization to vibrationally and thermally compensated ultralow-expansion glass Fabry-Pérot cavities.*, Phys. Rev. A **77**, 053809 (2009). DOI: 10.1103/PhysRevA.77.053809.

[48] K. Jousten. *Handbook of Vacuum Technology*. Wiley - VCH, 2016. ISBN: 978-3-527-41338-6.

[49] M. Martin. *Quantum Metrology and Many-Body Physics: Pushing the Frontier of the Optical Lattice Clock*, PhD thesis University of Colorado (2013). URL: https://jila.colorado.edu/bibcite/reference/3282.

[50] Wavelength Electronics. *Optimizing Thermoelectric Temperature Control Systems*, Technical Note TN-TC01 Rev. D (2020). URL: https://www.teamwavelength.com/download/applicationtechnotes/tn-tc01.pdf.

[51] D. Tilbury and B. Messner. *Control tutorials for Matlab and Simulink*, (2011). URL: https://ctms.engin.umich.edu/CTMS/index.php?example=Introduction&section=ControlPID#1.

[52] S. Skogestadt. *Probably the best simple PID tuning rules in the world*, Journal of Process Control **04-09**, 276 (2001). URL: https://folk.ntnu.no/skoge/publications/2001/tuningpaper_reno/tuningpaper_06nov01.pdf.

[53] J. Ziegler and N. Nichols. *Optimum Settings for Automatic Controllers*, J. Dyn. Sys., Meas., Control **115(2B)**, 220–222 (1993). DOI: 10.1115/1.2899060.

[54] Engineers-excel. *PID Loop Simulator*, (visited on 21/11/2021). URL: http://www.engineers-excel.com/Apps/PID_Simulator/Description.htm.

[55] DOTX Control Solutions. *PID Tuning Guide*, (visited on 15/03/2021). URL: https://www.pid-tuner.com/pid-control/.

[56] W. Riley. *Handbook of Frequency Stability Analysis*, NIST Special Publication 1065 (2008). URL: https://tf.nist.gov/general/pdf/2220.pdf.

[57] D. Howe, D. Allan, and J. Barnes. *Properties of signal sources and measurement methods*, Proceedings of the 35th Annual Symposium on Frequency Control (1981). URL: https://tf.nist.gov/general/pdf/554.pdf.

[58] WavelengthElectronics. *Operating Guide: HTC Series & HTCEVAL PCB*, (2020). URL: https://www.teamwavelength.com/download/Datasheets/htcseries.pdf.

[59] L. Ma, P. Jungner, J. Ye, and J. Hall. *Delivering the same optical frequency at two places: accurate cancellation of phase noise introduced by an optical fiber or other time-varying path*, Optics Letters **19**, 1777–1779 (1994). DOI: 10.1364/ol.19.001777.

[60] L. Duan. *General treatment of the thermal noises in optical fibers*, Phys. Rev. A **86**, 023817 (2012). DOI: 10.1103/PhysRevA.86.023817.

[61] H. Callen and R. Greene. *On a Theorem of Irreversible Thermodynamics*, Phys. Rev. 86 **86**, 702 (1952). DOI: 10.1103/PhysRev.86.702.

[62] Y. Levin. *Internal thermal noise in the LIGO test masses: A direct approach*, Phys. Rev. D **57**, 659 (1998). DOI: 10.1103/PhysRevD.57.659.

[63] Y. Levin. *Fluctuation–dissipation theorem for thermo-refractive noise*, Physics Letters A **372**, 1941–1944 (2008). DOI: 10.1016/j.physleta.2007.11.007.

[64] L. Landau and E. Lifshitz. *Theory of Elasticity*. Butterworth-Heinemann, 1970. ISBN: 9780750626330.

[65] J. Beck, K. Cole, A. Haji-Sheikh, and B. Litkouhi. *Heat Conduction Using Green's Functions*. CRC Press, 2010. ISBN: 9781439813546.

[66] L. Landau and E. Lifshitz. *Fluid Mechanics*. Pergamon, 1987. ISBN: 9781483161044.

[67] I. Gradshteyn and I. Ryzhik. *Table of Integrals, Series, and Products*. Academic Press, 1994. ISBN: 9780123849335.

[68] K. Yamamoto, M. Ando, K. Kawabe, and K. Tsubono. *Theoretical approach to thermal noise caused by an inhomogeneously distributed loss: Physical insight by the advanced modal expansion*, Phys. Rev. D **75**, 082002 (2007). DOI: 10.1103/PhysRevD.75.082002.

[69] C. Zener. *Elasticity and Anelasticity of Metals*. University of Chicago Press, 1948. ISBN: 9780608127637.

[70] L. Duan. *Intrinsic thermal noise of optical fibres due to mechanical dissipation*, Electron. Lett. **46**, 1515–1516 (2010). DOI: 10.1049/el.2010.1653.

[71] P. Saulson. *Thermal noise in mechanical experiments*, Phys. Rev. D **42**, 2437 (1990). DOI: 10.1103/PhysRevD.42.2437.

[72] Thorlabs. *Spec sheet for PM630-HP fiber*, (visited on 6/05/2021). URL: https://www.thorlabs.de/drawings/cd97c2ec8f238ec5-4B8D6181-D0D7-48E7-71239B8988A66F76/PM630-HP-SpecSheet.pdf.

[73] R. Bartolo, A. Tveten, and A. Dandridge. *Thermal Phase Noise Measurements in Optical Fiber Interferometers*, IEEE J. Quantum Electron **48**, 720–727 (2012). DOI: 10.1109/JQE.2012.2190717.

[74] B. Beadle and J. Jarzynski. *Measurement of speed and attenuation of longitudinal elastic waves in optical fibers*, Opt. Eng. **40**, 10 (2001). DOI: 10.1117/1.1403449.

[75] P. Antunes, H. Lima, J. Monteiro, and P. Andre. *Elastic constant measurement for standard and photosensitive single mode optical fibres*, Opt. Technol. Lett. **50**, 2467–2469 (2008). DOI: 10.1002/mop.23660.

[76] W. Schwenger and J. Higbie. *High-speed acousto-optic shutter with no optical frequency shift*, Review of Scientific Instruments **83**, 083110 (2012). DOI: 10.1063/1.4746292.

[77] Microchip-Technology. *VS-705 Single Frequency VCSO Datasheet*, (2014). URL: https://www.vectron.com/products/vcso/vs705.pdf.

[78] P. Scherz and S. Monk. *Practical Electronics for Inventors*. McGraw-Hill Education Ltd., 2000. ISBN: 978-1259587542.

Acknowledgements

First and foremost, I would like to thank **Prof. Immanuel Bloch** for granting me the great opportunity to be part of this group, and providing us with this outstanding research environment at the Max Planck Institute of Quantum Optics.

Secondly, I would like to express my gratitude to my principal investigator **Dr. Sebastian Blatt**. You consistently allowed this thesis to be my own work, but steered me in the right direction whenever you thought I needed it.

I would like to especially thank **Valentin Klüsener**. You are like my big brother, always being there when I needed help, and giving me encouragement when I made mistakes.

Another big thank you goes to **Karsten Förster**. As the group electrician you were always swamped by a million different tasks everyday. But yet you managed to take a great portion of your time to look over my project and gave me patient guidance. When I joined I was absolutely a rookie in circuitry, and now I am confident to work with really complicated circuits. All of these cannot happen without you.

Throughout my project, I have also received a great deal of support and assistance from my other colleagues in the team: **Annie Jihyun Park**, **Dr. André Heinz**, **Dr. Dimitry Yankelev**, **Jan Trautmann**, **Florian Wallner**, and **Eva Casotti**. Thank you all for your insightful comments and suggestions.

Moreover, I would like to express my sincere gratitude to **Anton Mayer** and **Olivia Mödl** for your reliable assistance in solving technical issues, and to **Kristina Schuld** and **Doreen Seidl**, for your prompt support in organizational tasks.

I would also like to thank my co-master student **Dimitrios Tzevas** for being a great company. It would be a very different journey without your friendship. Also, I would like to thank my office mate **Romain Granier** for all the relaxing chats during lunch breaks, and for trusting me by asking my advice during your internship.

Finally, many thanks to my **family** and to **Aimee**, for your love and support.

Appendix A

Arduino Code for the Home-built Digital Temperature Servo

```
#include <Adafruit_MCP4728.h>
#include <Wire.h>

//PID constants
//double kp = 400000;  //Critical gain, with period about 6 mins
//double ki = 0;
//double kd = 0;

//Only PI
double kp = 180000;
double ki = 0.6;
double kd = 0;

//With PID
//double kp = 240000;
//double ki = 1.33;
//double kd = 10800000000;


unsigned long currentTime, previousTime;
double elapsedTime;
double error;
double lastError;
double input, output, setPoint;
double cumError, rateError;

Adafruit_MCP4728 mcp;

// the setup routine runs once when you press reset:
void setup() {
        setPoint = 0.85; //divide by 1000

        // initialize serial communication at 9600 bits per second:
        Serial.begin(115200);
        while (!Serial)
        delay(10); // will pause Zero, Leonardo, etc until serial console
             opens

        if (!mcp.begin()) {
```

```
                Serial.println("Failed to find MCP4728 chip");
                while (1) {
                        delay(10);
                }
        }

        mcp.setChannelValue(MCP4728_CHANNEL_B, 0);
        mcp.setChannelValue(MCP4728_CHANNEL_D, 512);

}

// the loop routine runs over and over again forever:
void loop() {

        // read the input on analog pin 0:
        int sensorValue = analogRead(A0);
        // Convert the analog reading (which goes from 0 - 1023) to a
            voltage (0 - 5V):
        float voltage = sensorValue * (5.0 / 1023.0);
        output = computePID(voltage);
        //delay(100);

        if (output > 4048)
        {
                output = 4048;
                Serial.println("Max power output");
        }
        // print out the value you read:
        //Serial.println(voltage);
        Serial.println(output);
        mcp.setChannelValue(MCP4728_CHANNEL_A, output);
        mcp.setChannelValue(MCP4728_CHANNEL_C, 4048);

        //delay(200);
}

double computePID(double inp){
        currentTime = millis();
        //get current time
        elapsedTime = (double)(currentTime - previousTime);
        //compute time elapsed from previous computation

        error = inp - setPoint;
        // determine error
        Serial.println(error);

        cumError += error * elapsedTime;
        // compute integral
        rateError = (error - lastError)/elapsedTime;
        // compute derivative

        double out = kp*error + ki*cumError + kd*rateError;
        //PID output
```

```
        lastError = error;
        //remember current error
        previousTime = currentTime;
        //remember current time

        return out;
        //have function return the PID output
}
```

Appendix B

Key Components and Testing Notes for the First Generation FNC PCBs

Name	Index	Part No.	Testing method	Observation	Result
Positive voltage regulator	IC31	78M33	TPV3	3.3 V	Pass
Voltage Controlled SAW Oscillator (VCSO)	VCSO121	VS-705 LFF -GAAN 155M520	BNC port: "VCO F out" or SMA Port: "VCO F/2(AOM) out"	Single peak at 155.520 MHz	Pass
Voltage controlled crystal oscillator (VCXO)	VCXO1	ABLJ0V	Pre-amp: TP23 Post-amp: Ports "Ref. RF out" and "Ref. RF monitor"	Single peak at 155.520 MHz	Pass
Cross-talking of the VCXO and VCSO	NA	NA	Deviate the frequencies of the two oscillators. See if one can observe on the output port of one oscillator the signal from the other oscillator.	Observe clear VCXO signal from the VCSO output. Found signs of cross-talking	Fail

Table B.1 continued from previous page

Name	Index	Part No.	Testing method	Observation	Result
Power Splitter	U31	MC-ADP -2-1	Ports "Ref. RF out" and "Ref. RF monitor" (TP 36; TP 37)	See signal from both ports	Pass
Positive voltage regulator	IC121	78M33	TPV4	Resistor RW2 is initially left open and no current goes into IC121. However, even when RW2 is connected, IC121 still doesn't work (TPV4 has voltage smaller than 1V) and RW2 immediately become extremely hot. (IC121 is replaced by an external voltage regulator, see below)	Fail
Positive voltage regulator (Externally Connected)	NA	78M33	TPV4	3.27 V at TPV4; However, converting 15 V to 3.27 V leads to great heat dissipation. Part gets extremely hot given time.	Fail
Emitter Coupled Logic (ECL) 1:2 Differential Fanout Buffer	U1	MC100 -EP11DG	BNC port: "VCO F out" (or TP47)	Freq. at 155.520 MHz	Pass

Table B.1 continued from previous page

Name	Index	Part No.	Testing method	Observation	Result
ECL D Flip-Flop with Reset and Differential Clock	U2	MC100 -EP51DG	SMA Port: "VCO F/2(AOM) out" (or TP45)	Single peak at 77.76 MHz	Pass
Photodiode signal (Externally input)	SMA Port: "PD input"	NA	SMA port: "PD monitor out"	Observe clear signal from PD	Pass
RF power detector	U42	AD8361 -ARTZ -RL7	Change the output power of the function generator which serves as the PD input. Measure the voltage across TP1 to see if it changes accordingly.	Output voltage (TP1) only changes proportionally when PD input is larger than 12.5 dBm. Below 12.5 dBm the power detector has constant output regardless of the PD input power. (LED remains red all the time)	Pass
Limiter	LM21	MCL-PLS-2	Amplitude modulate the PD signal, and detect the signals before and after the limiter. The limiter should greatly suppress the amplitude fluctuation. Before limiter: port "PD monitor" After limiter: TP14	The AM mod directly affects the "PD monitor" signal, by has little effect on the signal after the limiter (TP14)	Pass

Table B.1 continued from previous page

Name	Index	Part No.	Testing method	Observation	Result
Positive voltage regulator	IC21	78L09	TPV9	8.12 V	Pass
High Reliability Mixer	U21	MC-ADE -R1L+	Feed function generator signal at around 155.520 MHz into PD input. Observe from a spectrum analyzer the (F-f) and (F+f) IF signals (with higher harmonics).	Observed the expected IF signals	Pass
Butterworth low-pass filter for IF signal	L32, C28, C29, etc.	NA	Measure TP13 to see if the harmonics are filtered	Higher order harmonics attenuated by 50 dB.	Pass
Adjustable Positive Voltage Regulator	IC301	LM317	TP301	Can reach 5V after tuning	Pass
Adjustable Negative Voltage Regulator	IC302	LM337	TP302	Can reach -5V after tuning	Pass

Table B.1 Key components and testing notes for the first generation FNC PCBs

Erklärung

Hiermit erkläre ich, die vorliegende Arbeit selbständig verfasst zu haben und keine anderen als die in der Arbeit angegebenen Quellen und Hilfsmittel benutzt zu haben.

München, Datum der Abgabe

Unterschrift